

VERITAS OBSERVATIONS OF PULSAR WIND NEBULAE  
IN THE VHE BAND

A Dissertation

Submitted to the Faculty

of

Purdue University

by

Benjamin J. Zitzer

In Partial Fulfillment of the

Requirements for the Degree

of

Doctor of Philosophy

December 2010

Purdue University

West Lafayette, Indiana

This work is dedicated to the memory of my late uncle, Richard Stewart, who was taken from us too soon. I know that a part of him was with me through the writing process, and certainly will be with me during the celebrations when I'm finished.

## ACKNOWLEDGMENTS

There are so many people to thank! First, my loving family, who I think never quite understood why I've chosen this path, but never doubted for a second that I could accomplish it. Thanks to the friends who have been along me on the way: Brandon Hogan, Josh Konzer, Suzanne and John Lorenz, Mark and Bethany Theiling, Kari Frank, Angelo Varlotto, Kris Carlson, Daniel Gall, John Millis, Ben Philabaum, Andy Irrgang, Sarma, Qi Feng, Paul and Heather Mistretta, Mary Kertzman, and the gang in Franklin just to name a few of them. Thanks Heather and Emjay in the high-energy office and Sandy Formica downstairs for dealing with all that bureaucracy that I didn't want to put up with. I owe a great deal to my VERITAS collaborators, especially the ones that helped me out during the year I spent on the site: Ken Gibbs, Trevor Weekes, Jeremy and Donna Perkins, John Kildea, John E. Ward, John Toner, Andy Smith, Peter Cogan, Mark Theiling (yes, I know I mentioned him once already, he deserves it) among others. I think that the VERITAS collaboration built and now operates a wonderful experiment (although I might be a bit biased) and I am proud that I was able to contribute in some small way. Extra thanks goes to those people I mentioned who had to put up with me as a roommate. Special thanks goes to Glenn Sembroski for his moral support, advice, and for being my C++ guru.

Finally, I'd like to thank John Finley. He has been a friend and mentor to me all for the low price of indentured servitude for several years. I doubt that I would have gotten through graduate school with anyone else as a Ph.D. advisor. Any future endeavors of mine will only occur because of him.

## TABLE OF CONTENTS

	Page
ACKNOWLEDGMENTS .....	iii
TABLE OF CONTENTS.....	iv
LIST OF TABLES .....	vii
LIST OF FIGURES .....	viii
LIST OF ABBREVIATIONS.....	xi
ABSTRACT.....	xii
CHAPTER 1. INTRODUCTION TO HIGH ENERGY ASTROPHYSICS .....	1
1.1. History of VHE astronomy .....	1
1.2. Status of VHE Astronomy as of Summer 2010.....	3
1.2.1. VERITAS.....	3
1.2.2. HESS.....	4
1.2.3. MAGIC .....	4
1.2.4. Fermi.....	5
1.3. Types of VHE Sources.....	6
1.3.1. Extra-Galactic sources .....	6
1.3.2. Galactic Sources.....	7
1.4. Important Astrophysical processes for VHE astronomy .....	9
1.4.1. Synchrotron Radiation .....	10
1.4.2. Inverse Compton Scattering.....	10
1.4.3. Curvature Radiation.....	11
1.4.4. Bremsstrahlung Radiation.....	12
1.4.5. Pion Production and decay.....	12
1.5. Outline of the remainder of work.....	13
CHAPTER 2. PULSAR WIND NEBULAE .....	15
2.1 Stellar Evolution .....	15
2.1.1. The Lifetime of a Main Sequence Star .....	15
2.1.2. The Physics of Degenerate Matter .....	18
2.1.3. Life After Death for a Star .....	20
2.2. Characteristics of Pulsars:.....	21
2.2.1. Spin-down Luminosity.....	22
2.2.2. Pulsar Age.....	22
2.2.3. Magnetic Field .....	23
2.2.4. Light Cylinder Surface.....	24
2.2.5. Charge Density and the Null Charge Line .....	25

	Page
2.3. Pulsar Particle Acceleration Models .....	27
2.3.1. Polar Cap Model .....	27
2.3.2. Outer Gap Model .....	29
2.3.3. Co-rotation model .....	31
2.3.4. Slot-Gap Models .....	32
2.3.5. Hadronic Models.....	33
2.4. Definition of a Pulsar Wind Nebula: .....	34
2.5. Evolution of a PWN.....	35
CHAPTER 3. ATMOSPHERIC CHERENKOV TECHNIQUE.....	37
3.1. Cherenkov Radiation .....	37
3.2. Cosmic Ray Showers .....	39
3.3. VERITAS Telescope Array .....	41
3.4. Data Analysis .....	48
3.4.1. Calibration Calculation and Application .....	48
3.4.2. Shower Reconstruction .....	49
3.4.3. Gamma-Ray Signal Extraction .....	52
3.4.4. Other Data Products .....	55
CHAPTER 4. PWN SELECTION CRITERIA .....	58
4.1. VHE PWN Population Study.....	58
4.2. Results of the Population study: .....	59
4.3. Candidates for VHE Observation .....	63
4.3.1. Crab Nebula .....	64
4.3.2. PSR J1928+1746/PSR J1930+1852.....	64
4.3.3. PSR J2229+6114/Boomerang.....	65
4.3.4. PSR J1856+0245/HESS J1857+026.....	65
4.3.5. PSR J2021+3651/Cisne PWN .....	66
4.3.6. 3C58.....	66
4.4. Conclusions of the Population Study.....	66
CHAPTER 5. PWN OBSERVATIONS .....	67
5.1. Crab Nebula and Pulsar .....	67
5.1.1. Cuts and Data Set Used for Analysis .....	67
5.1.2. Results of Observations of the PWN .....	69
5.1.3. Pulsar Analysis.....	71
5.2. G54.1+0.3/PSR J1930+1852 & PSR J1928+1746 .....	76
5.2.1. Cuts and Data Set Used for Analysis .....	76
5.2.2. Results of Observations of Nebulae.....	77
5.2.3. Pulsar Analysis for PSR J1930+1852.....	81
5.3. The Boomerang PWN and PSR J2229+6114 .....	82
5.3.1. Cuts used and data set.....	82
5.3.2. Results of observations of the PWN G106.3+2.7 .....	83
5.3.3. Pulsar analysis of PSR J2229+6114 .....	86
5.4. HESS J1857+026/PSR J1856+0245 .....	87
5.4.1. Cuts used and data set.....	87
5.4.2. Observation results of HESS J1857+026.....	88

	Page
5.4.3. Pulsar Analysis of PSR J1856+0245 .....	91
5.5. 3C58 & PSR J0205+6449 .....	92
5.5.1. Cuts used and data set .....	92
5.5.2. Observation results for 3C58 .....	92
5.5.3. PSR J0205+6449 .....	94
5.6. Cisne PWN & PSR J2021+3651 .....	95
5.6.1. Data set and cuts used .....	95
5.6.2. Observation results of G75.2+0.1 .....	96
5.6.3. PSR J2021+3651 .....	99
CHAPTER 6. Conclusions .....	101
6.1. PWNe Observation Summary .....	101
6.2. PWNe Discussion .....	104
6.3. Pulsar Observation Summary .....	106
6.4. Pulsar Discussion .....	107
BIBLIOGRAPHY .....	109
VITA .....	118

## LIST OF TABLES

Table	Page
Table 4.1. PWN which are VHE emitters as of Spring 2010. ....	59
Table 5.1. Cuts used for Crab Nebula analysis.....	69
Table 5.2. Cuts used for the Crab Pulsar during three seasons of observation.....	72
Table 5.3. Cuts used for G54.1+0.3 and PSR J1930+1852 .....	77
Table 5.4. Cuts used for G106.3+2.7 and PSR J2229+6114 .....	83
Table 5.5. Cuts used for G75.2+0.1 .....	96
Table 6.1. Analysis summary of PWN .....	102
Table 6.2. Post-trials Significance of detected sources.....	102
Table 6.3. Summary of Spectral Data.....	103
Table 6.4. Pulsar Statistical Test Results .....	107

## LIST OF FIGURES

Figure	Page
Figure 1-1. The VHE sky as of summer 2010. Type of source is shown by color. Red indicates AGN, violet for PWN, green for shell SNR, orange for starburst galaxies, Gray for unidentified VHE sources, and binary systems in blue. [2] .....	1
Figure 1-2. The first VHE telescope in the US, built using WWII surplus searchlights, operated in the winter of 1967-8. The site of this experiment south of Tucson, AZ is the same current location as the VERITAS observatory. [3] .....	2
Figure 2-1. Typical H-R diagram. Credit: NASA/CXC/SAO .....	16
Figure 2-2 Image of the Crab SNR shown in three wavelengths. The Chandra X-ray image is shown light blue, while Spritzer IR is red, and the Hubble Space Telescope image is dark blue and green. Credit: X-ray: NASA/CXC/ASU/J. Hester & A. Loll; Optical: NASA/ESU/ASU/J. Hester & A. Loll; Infraed: NASA/JPL-Caltech/Univ. Minn./R. Gehrz. ....	18
Figure 2-3. Illustration of the pair production cascade present in polar cap models. The electron closest to the NS surface emits curvature radiation ( $\gamma cr$ ) which pair produces on the magnetic field, creating leptons which repeats this process [37].	29
Figure 2-4 Outer gap magnetosphere with gap regions shaded in gray. The gaps have the last closed magnetic field line, the null surface, and the light cylinder as boundaries. [39] .....	31
Figure 2-5 Depiction of the slot gap model. [42].....	33
Figure 3-1. Illustration of Hygens construction for Chrenkov radiation .....	38
Figure 3-2 VERITAS array at the Fred Lawrence Whipple Observatory base camp .....	42
Figure 3-3 The T1 camera box with 499 pixel camera [1]. ....	44
Figure 3-4 Efficiency for an average Photonis PMT plotted as a function of wavelength.	44
Figure 3-5. Illustration of the VERITAS data acquisition system [51]. ....	47
Figure 3-6 Image of a gamma ray shower and its projection onto an ACT camera (left), and the same for a hadronic shower (center) and a hardronic shower with a muon “ring” (right). Image courtesy of G. Sembroski. ....	50
Figure 3-7 Images of a Cherenkov shower in the four telescopes (four left images) and its reconstructed position on the ground (right).....	52
Figure 3-8. A significance sky map of the Crab Nebula, the standard candle of TeV astronomy. The white circles indicate regions excluded for use as background. ...	54
Figure 3-9. Effective area plots for two different simulations packages. KASCADE simulations are in red, CORSIKA are in black. ....	55



Figure	Page
Figure 4-1. Period vs. Period derivative plot. Blue contour lines are characteristic ages for the pulsar, and black contour lines are spin-down luminosity. Red asterisks indicate already established VHE PWN from table 4-1, green circles are potential sources discussed in this section, and other pulsars are blue crosses. ....	60
Figure 4-2. Plot of TeV Luminosity as a function of spin-down power. Contour lines of TeV efficiency are also drawn. ....	61
Figure 4-3. TeV Luminosity as a function of the square root of spin-down luminosity. The best fit value of equation 4.2 is shown as the blue line. ....	63
Figure 5-1. $\theta^2$ distribution of the Crab Nebula in red, the Crab OFF regions in blue, and the Crab scaled down to 25% of the total excess in Green. ....	68
Figure 5-2. Excess (left) and Significance (right) maps of the Crab PWN. White circles indicate background exclusion regions in the analysis. ....	70
Figure 5-3. Spectrum of the Crab Nebula before (left) and after (right) the T1 move .....	70
Figure 5-4. Phase histogram for Crab Pulsar data over two periods. The red dashed line represents the best fit to a constant value. ....	73
Figure 5-5. Optical data of the Crab Pulsar taken from the Multiple Mirror telescope (MMT), located on Mt. Hopkins, AZ. ....	73
Figure 5-6. ON and OFF distributions of pulsed photons, where the ON region is defined as the P2 region. ON region photons are shown in red, while OFF region distribution is blue. ....	75
Figure 5-7. Distribution of energy of the excess pulsed photons for the Crab pulsar at the P2 position. ....	75
Figure 5-8. Excess map for the G54.1+0.3 region. ....	78
Figure 5-9. Significance map for the G54.1+0.3 region. ....	78
Figure 5-10. Significance distribution of the G54.1+0.3 sky region. The best fit Gaussian function is shown as the black curve. ....	79
Figure 5-11. Significance distribution of the G54.1+0.3 sky region, excluding a region of $0.3^\circ$ around G54.1+0.3. ....	79
Figure 5-12. Spectrum for G54.1+0.3, fit to a powerlaw of the form in equation 5.1. ....	80
Figure 5-13. Phase histogram for PSR J1930+1852. The dashed red line is the best fit to a constant value. ....	82
Figure 5-14. Excess map of the G106.3+2.6 region. The pulsar position is shown by the light blue point. A PMT is drawn for scale. ....	84
Figure 5-15. Significance map of the G106.3+2.6 region. The pulsar position is shown by the light blue point. A PMT is drawn for scale. ....	84
Figure 5-16. Significance distribution of the G106.3+2.6 region. A Gaussian best fit is shown as a blue curve on the figure. ....	85
Figure 5-17. VERITAS spectrum of G106.3+2.7. The black line shown is the best fit to the powerlaw function. ....	86
Figure 5-18. Phase histogram for PSR J2229+6114. The dashed red line is the best fit to a constant value. ....	87
Figure 5-19. Excess counts map in the HESS J1857+026 FOV. The blue cross represents the pulsar position, and the black points are the two HESS UNID sources. ....	89

Figure	Page
Figure 5-20. Significance map in the HESS J1857+026 FOV. The blue cross represents the pulsar position, and the black points are the two HESS UNID sources. ....	89
Figure 5-21. Significance distribution in the HESS J1857+026 FOV. The blue curve is the best fit to a Gaussian function. ....	90
Figure 5-22. Spectrum of HESS J1857+026. The black line represents the best fit of the spectrum to a powerlaw of the form of equation 5.1. ....	91
Figure 5-23. Phase histogram of PSR J1856+0245. The red dashed line represents the best fit of the phase histogram to a constant value. ....	92
Figure 5-24. Excess Map of the 3C58 FOV .....	93
Figure 5-25. Significance Map of the 3C58 FOV.....	93
Figure 5-26. Significance distributions of 3C58 with the $0.3^\circ$ source exclusion around 3C58 (right) and without the source exclusion (left). Both distributions are fit by a Gaussian function shown in blue. ....	94
Figure 5-27. Phase histogram of PSR J0205+6449 .....	95
Figure 5-28. Excess counts map for G75.2+0.1. The light blue points indicate the positions of the PWNe and the INTEGRAL source IGR J20188+3647. ....	97
Figure 5-29. Significance map for G75.2+0.1. The light blue points indicate the positions of the PWNe and the INTEGRAL source IGR J20188+3647.....	97
Figure 5-30. Significance Distribution of G75.2+0.1. The blue curve is the fit of the significance distribution to a Gaussian. ....	98
Figure 5-31. Spectrum of G75.2+0.1 .....	99
Figure 5-32. Phase histogram of PSR J2021+3651. The red dashed line is the fit of the phase histogram to a constant value.....	100

## LIST OF ABBREVIATIONS

VERITAS: Very Energetic Radiation Imaging Telescope Array System

VHE: Very High Energy

PWN(e): Pulsar Wind Nebula(e)

IC: Inverse Compton

ACT: Atmospheric Cherenkov Telescope

HESS: High Energy Stereoscopic System

MAGIC: Major Atmospheric Gamma Imaging Cherenkov Telescope

HEGRA: High Energy Gamma Ray Array

FOV: Field of View

PMT: Photomultiplier Tube

AGN: Active Galactic Nuclei

SN: Supernovae

SNR: Supernovae Remnant

NS: Neutron Star

PSR: Pulsating Source of Radio

UNID: Unidentified

GRB: Gamma Ray Burst

MSL: Mean Scaled Length

MSW: Mean Scaled Width

HSM: Height of Shower Maximum

OVA: Old VERITAS Array

NVA: New VERITAS Array

## ABSTRACT

Zitzer, Benjamin J. Ph.D., Purdue University, December, 2010. VERITAS Observations of Pulsar Wind Nebulae in the VHE Band. Major Professor: John Finley.

Pulsars have been known to exist for over forty years now, but the nature of their emission throughout the EM spectrum is still not well understood. Pulsar Wind Nebulae (PWNe) are most likely fueled by spin-down energy of the pulsar, but multiple theories exist on how particles are accelerated to create very high energy (VHE) gamma-rays. This work discusses results and implications of VHE observations for PWNe and the pulsars associated with them, focusing on observations with VERITAS.

## CHAPTER 1. INTRODUCTION TO HIGH ENERGY ASTROPHYSICS

Compared to other branches of astronomy, Very High Energy (VHE) astronomy is relatively young in the sense of most of the detections in this area have only been found in the last 10 years of this writing (Summer 2010) and 20 years since the definitive detection of the Crab Nebula in 1989 by the Whipple 10m telescope [1]. The current VHE sky contains ~100 sources with energies above 100 GeV as shown in figure 1-1 [2].

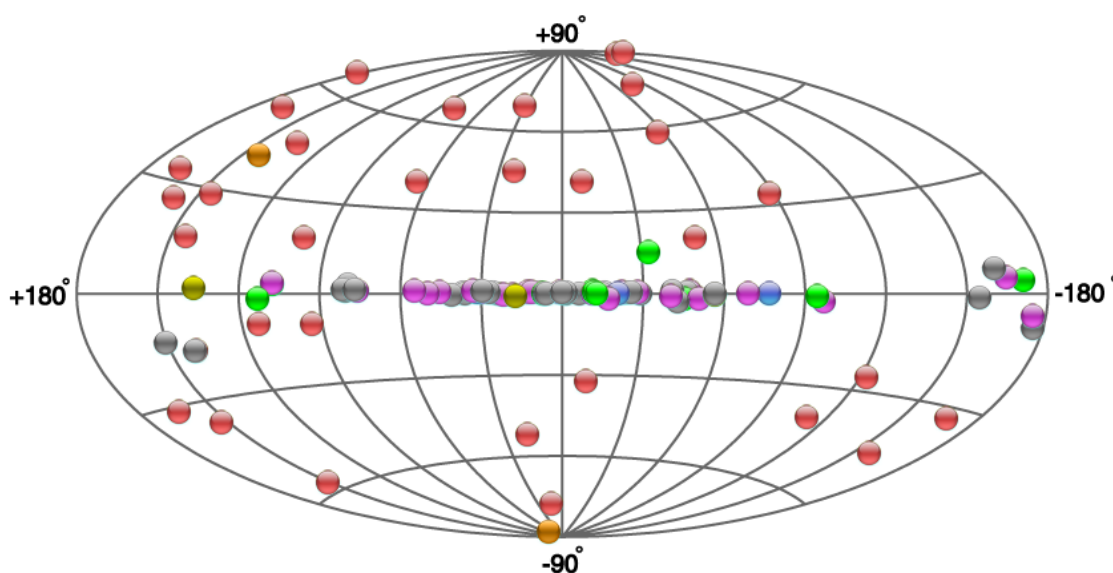


Figure 1-1. The VHE sky as of summer 2010. Type of source is shown by color. Red indicates AGN, violet for PWN, green for shell SNR, orange for starburst galaxies, Gray for unidentified VHE sources, and binary systems in blue. [2]

### 1.1. History of VHE astronomy

VHE astronomy is over fifty years old at this point, however, as previously mentioned, the first detections occurred only twenty years ago. The pioneers of this field were Chudakov and Zatsepin in the USSR while Jelly and Porter were working in the UK. At that time, there were no known X-ray or Gamma-Ray sources [3]. Cosmic rays were

known since Victor Hess's balloon experiments back in 1911-1912, but their origin is still a debated subject. The existence of cosmic rays implied that particles were accelerated to high energies in places beyond the earth's atmosphere, but that didn't necessarily imply gamma ray fluxes at levels that could be measured. Early experiments were somewhat crude (see figure 1-2), until the construction of the 10m telescope on the ridge of Mt. Hopkins south of Tucson AZ in 1968. Originally, the 10m telescope had a single photomultiplier tube (PMT). With a single PMT it is very difficult to discriminate the gamma ray showers from the much larger cosmic ray background [3]. Collectively, these are now referred to as the 'first generation' of VHE experiments.



Figure 1-2. The first VHE telescope in the US, built using WWII surplus searchlights, operated in the winter of 1967-8. The site of this experiment south of Tucson, AZ is the same current location as the VERITAS observatory. [3]

The ‘second generation’ of VHE experiments was envisioned as early as 1980 [3]. The next generation consisted of upgrades to the Whipple 10m camera (37 PMTs at that time), the HEGRA array and a couple other experiments. The biggest improvement of this generation of instruments was due to cameras of PMTs that were being used to image the Cherenkov air shower which in turn allowed imaging at TeV energies. Monte Carlo techniques simulating air showers were necessary for discriminating between gamma ray showers and hadronic cosmic ray showers. While this technique was successful in detecting the Crab Nebula [1] and a handful of other sources, arrays of Cherenkov telescopes were necessary to reduce the large muon background at low energies and increase sensitivity. An explanation of how arrays accomplish this is in chapter 3. Small arrays were already beginning to be built in the 1980’s, but they lacked the sensitivity of the next generation of these experiments.

### 1.2. Status of VHE Astronomy as of Summer 2010

Currently, this is the ‘Third Generation’ of VHE experiments. Most scientific results are dominated by the ‘big three’: HESS, MAGIC, and VERITAS. However, there are other experiments such as the Whipple 10-meter telescope and the CANGEROO III experiment which are important for AGN monitoring. Milagro, a water Cherenkov telescope, detected photons from sources at energies above 20 TeV, which is above the energy range of many atmospheric Cherenkov experiments. These experiments are all well-complimented by the Fermi space telescope, which operates below the energy threshold of the ACT experiments, at energies from 100 MeV up to tens of GeV [3].

#### 1.2.1. VERITAS

VERITAS (Very Energetic Radiation Imaging Telescope Array System) is an array of four 12m telescopes located in southern Arizona at the base camp of the Fred Lawrence Whipple Observatory (FLWO) only a few miles away from the pioneering Whipple 10m telescope. Each telescope consists of a camera of 499 PMTs, 350 mirrors and a 3.5 deg field of view (FOV). The design of the optical support structure (OSS) is the same as the

Whipple 10m telescope, the Davies-Cotton design [4]. The sensitivity of VERITAS is such that a source that is 1% of the Crab Nebula flux can be detected in less than 50 hours. The energy resolution of VERITAS is about 15% to 20% [5] at 1 TeV. Energy resolution is defined as  $\Delta E/E$ , where  $E$  is the energy of the gamma ray. The technical details of VERITAS will be discussed in depth in section 3-3.

### 1.2.2. HESS

HESS (High Energy Stereoscopic System), like VERITAS, consists of four telescopes based on the Davies–Cotton design. It has a wider FOV (5 degrees) than VERITAS. HESS is located in Namibia in Africa at 1.8km altitude, and has been in operation since 2003. Each telescope has a camera composed of 960 PMTs and a 107m<sup>2</sup> area reflector [6]. The angular resolution of HESS is 0.03° [7]. The spectral range for HESS is similar to VERITAS, from 100 GeV to 10 TeV. Currently a fifth HESS telescope is under construction which is larger than the current four in operation in hopes of lowering the energy threshold [8].

### 1.2.3. MAGIC

MAGIC (Major Atmospheric Gamma Imaging Cherenkov telescope) is located at LaPalma, in the Canary Islands, on the site that formerly had the HEGRA array. MAGIC operated as a single telescope since its commissioning in the summer of 2004, until a second telescope (MAGIC II) was constructed 85m away and started taking data in the summer of 2009 [9]. Both MAGIC telescopes have 17m diameter reflectors and high QE PMTs which allow for more light collection, leading to a lower energy threshold than HESS or VERITAS, 25 GeV [10]. MAGIC also has a faster slewing speed than VERITAS or HESS, allowing for faster observations of objects than might be at a higher flux, such as active galactic nuclei (AGN) in a flaring state, or gamma ray bursts (GRBs). The total time for MAGIC to slew to any position in the sky is 30 to 60 seconds [10]. The FOV of MAGIC is 3.5 to 3.8 degrees [10].



#### 1.2.4. Fermi

Fermi (formerly GLAST or Gamma-ray Large Area Space Telescope) is a space-based gamma-ray telescope observing gamma rays from the range of tens of MeV to a few hundreds of GeV. Fermi carries two instruments on board: the Large Area Telescope (LAT) and the GLAST Burst Monitor (GBM). Fermi was launched in the summer of 2008 [11].

The LAT is considered the main instrument on Fermi, which is sensitive to gamma rays in the spectral range between 20 MeV and 300 GeV. This spectral range has not been explored since the ending of the EGRET mission on the Compton Gamma Ray Observatory (CGRO) in 2000. The LAT works by conversion of Gamma rays into electron-positron pairs. The detector consists of 16 trackers of 14 tungsten foil layers to facilitate pair conversion, and 18 layers of X-Y pairs of single-sided silicon detectors to measure the path the pair takes after conversion. The shower initiated by the pair is absorbed and has energy measured by a calorimeter composed of 1536 CsI crystals located at the bottom of the LAT. Plastic scintillators surround the instrument and detect charged particles to work as a veto shield for background rejection. The LAT has a wide FOV of 2.4sr, allowing imaging of large sections of the sky at a time, and scans the sky once every 2 to 3 orbits. The angular resolution of the LAT changes as a function of energy, going from  $0.09^\circ$  for a 10 GeV photon to  $3.4^\circ$  for a 100 MeV photon. The energy resolution varies from 9% at lower energies to 15% at higher ones [11].

The GBM monitors the sky for gamma-ray bursts in the hard X-ray/soft gamma ray regime, 8 keV to 30 MeV. The detector consists of twelve NaI crystal detectors for the lower energy range and two BGO crystal detectors for photons with energies above 150 keV. It has a FOV of 9.5sr which covers the entire sky except for portions that are blocked by the earth. The instrument has 12% energy resolution at 511 keV [11].

### 1.3. Types of VHE Sources

VHE sources can be categorized into two main groups: Galactic and extra-Galactic. Galactic sources are typically the evolved remnants of large stars, and the majority of extra-Galactic sources are AGN.

#### 1.3.1. Extra-Galactic sources

AGN (Active Galactic Nuclei) are galaxies that have their emission dominated by their bright central region that is believed to be powered by a super massive black hole ( $M > 10^8 M_{\odot}$ ). A jet, or collimated particle outflow, is typically observed coming from the central region believed to be the black hole. The majority of AGN that are seen at VHE energies are known as blazars, which are a subclass of radio-loud AGN with a small jet viewing angle with regards to the observer [12]. The first extra-galactic object detected at VHE energies was the blazar Markarian 421 (Mrk 421) [13]. A large subset of blazars detected at TeV energies are BL Lac objects (named for the prototypical object in this class, BL Lacertae) that lack any strong emission or absorption features [12]. They are notable for having rapid variability in flux on timescales shorter than days [14]. Most of the BL Lacs detected are high-frequency peaked BL Lacs (HBLs) that have a spectral peak in the X-ray band, believed to be caused by Synchrotron radiation from energetic electrons [5].

FSRQ (Flat Spectrum Radio Quasars) are another type of AGN that are seen at higher redshifts than Blazars. The FSRQ 3C279 first discovered by MAGIC is the highest redshift object detected in VHE. By measuring the amount of VHE photon attenuation from these objects, the amount of Extra-galactic Background Light (EBL) can be constrained. EBL photons create electron-positron pairs with TeV photons, so the attenuation in VHE is proportional to the EBL density [15]. Other AGN detected in VHE include the FR I galaxy M87. Observations of M87 during a flaring period were observed by VERITAS, MAGIC, HESS and the Very Long Baseline Array (VLBA). Chandra

observations revealed that the core of M87 was also active in the X-ray band, implying that TeV photons are observed from the core of M87 [5].

Starburst Galaxies are a recently discovered type of extra-galactic source. There are only two detected in VHE currently, M82 by VERITAS [16] and NGC 253 by HESS [17]. They are noted for having large star forming regions due to the interaction of a group of galaxies. High cosmic ray (CR) rates have been inferred from sources such as starburst galaxies have a high supernovae (SN) rate. M82 also has a large mean gas density  $\sim 150$  particles/cm<sup>2</sup>. Gamma Rays are believed to originate from interactions of cosmic rays with either the gas or local photon fields. These sources represent the only type of extra-galactic source which is not associated with an AGN [5].

The galactic center of the milky way, SgrA\*, has also been detected as a VHE source by HESS [18] after nearly being detected by the Whipple 10m telescope [33]. Although it is technically a galactic source, it is included with the extra-galactic sources because of the presence of a super massive black hole.

### 1.3.2. Galactic Sources

There are four types of VHE galactic sources: Supernovae Remnants (SNR), Pulsar Wind Nebulae (PWNe), Binary systems and unidentified sources.

Supernova Remnants are the end product of the explosion of a high mass star which lead to the formation of compact objects, i.e. neutron stars or black holes. The outer layers of the progenitor star are ejected into the interstellar medium (ISM). It is the interaction of the ISM and the stellar material which leads to emission throughout the electromagnetic spectrum. The morphology of the VHE source SNR IC443 overlaps a dense CO molecular cloud [19] as seen in figure 1-3. Supernova Remnants will be covered more in depth in section 2.1.

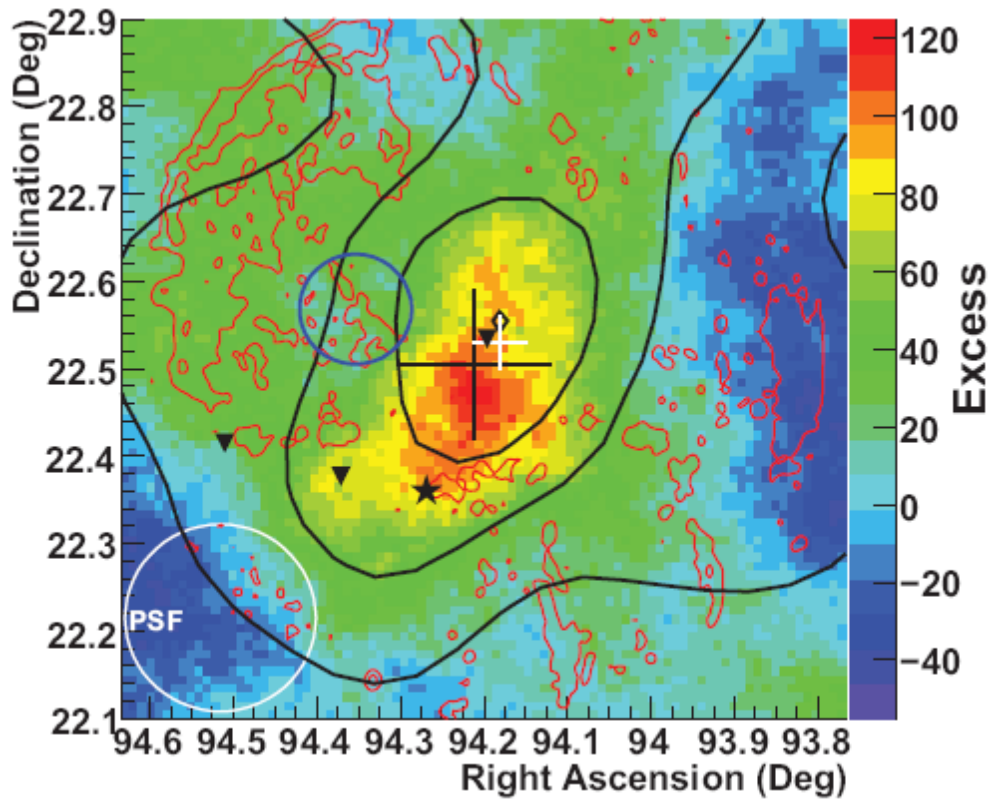


Figure 1-3. VHE excess map of the supernovae remnant IC443. Black contours are regions of CO [19].

There are a handful of microquasars that have been detected in VHE. These are compact objects in binary systems with bright companion stars that have common characteristics with quasars: strong radio emission coming from jets, and an accretion disk surrounding the central compact object. The accretion disk originates from the companion star and the relativistic jets result from the accretion onto the compact object. The VHE emission is noted for variability in flux with the orbital period and a hard spectrum [20]. As an example of the flux variability, the microquasar LSI+61303 has peak emission in TeV near apastron [21].

PWNe, as the name suggests, are nebulae that are powered by the wind (ejecta of particles) from an associated pulsar. Pulsars are a type of highly-magnetized, rapidly spinning neutron stars with periods ranging from a few milliseconds to a few seconds. The interaction of the pulsar wind with the nebula material causes emission throughout the EM spectrum [14]. Pulsars and PWN will be discussed more thoroughly in chapter 2.

Many of the unidentified sources are referred to as dark accelerators because they emit radiation at VHE but have no identified source at other wavelengths. The first of these sources, TeV 2023+4130, was discovered by HEGRA [22], leading to much speculation about what type of object it actually is. Later, the HESS sky survey discovered more of these sources [6]. This has led to searches for counterparts in other wavelengths by other instruments. One of these sources, HESS J1857+026, is now believed to be a PWN after a pulsar was discovered in the vicinity by the Arecibo PALFA radio survey [23] and will be discussed in detail in chapters 4 and 5.

#### 1.4. Important Astrophysical processes for VHE astronomy

Knowledge of radiation processes is required for most branches of astronomy, including VHE. Since most of everything we know about astronomical sources comes from photons from them, then understanding the physics behind the emission of the objects gives us insight into the processes occurring both within these objects and along the path to the observer. In VHE astronomy, there are two main emission processes to consider: Inverse Compton (IC) scattering, and neutral pion decay. They are referred to as leptonic and hadronic emission, respectively, due to the types of particles that are the source of the emission. Knowledge of other types of high-energy emission, such as synchrotron radiation, is also important to get a fuller understanding of astronomical objects over multiple wavelengths.

### 1.4.1. Synchrotron Radiation

A charged particle in a magnetic field under classical mechanics will radiate at only one frequency,  $\omega_{gyr} = qB/mc$ , known as the gyration frequency. A relativistic particle, however, will radiate over a range of frequencies above the gyration frequency. Synchrotron radiation is emitted by a charged particle at relativistic speeds in a magnetic field transverse to the particle's velocity. The radiation is beamed in a cone of angle  $1/\gamma$  with respect to the magnetic field, where  $\gamma$  is the Lorentz factor of the particle. The mean power loss by the particle averaged over pitch angles, and therefore the average power of the emitted radiation is:

$$P_{Synch} = \frac{4}{3} \sigma_T c \gamma^2 \beta^2 U_B \quad \text{Eq. 1.1}$$

where  $\sigma_T$  is the Thomson cross section and  $U_B = B^2/8\pi$  is the magnetic field energy density.  $\beta$  is defined as  $v/c$ , where  $v$  is the speed of the particle. The radiation peaks at a particular frequency:

$$\nu_c = \frac{3}{4\pi} \gamma^2 \omega_{gyr} \sin \alpha \quad \text{Eq. 1.2}$$

Where  $\alpha$  is the pitch angle between the particle's velocity and the magnetic field. Synchrotron radiation is an important process for astrophysics as it can explain processes ranging from radio to hard X-ray wavelengths [24].

### 1.4.2. Inverse Compton Scattering

Inverse Compton scattering occurs when an electron with high energy interacts with photons of lower energy (known as 'seed' photons), transferring energy to the photons, bumping the photons up to higher energies. Compton scattering, by contrast, is the process where higher energy photons transfers energy to electrons and lose energy. Suppose that a photon with energy  $h\nu$  is scattered by an electron with energy  $\gamma mc^2$ ,

where  $\gamma = \sqrt{1 - (v/c)^2}$ , the Lorentz factor of the incoming electron. The mean energy of the scattered photon is:

$$h\langle\nu'\rangle = \frac{4}{3}\gamma^2 h\nu \quad \text{Eq. 1.3}$$

So the photon gains an energy of  $\sim\gamma^2$  [25]. For ultra-relativistic electrons with Lorentz factors up to the millions, this can be quite a jump in the photon energy. This also means that the electrons lose quite a bit of energy in the scattering. The rate of energy lost by a single electron (and therefore gained by photons) undergoing this type of scattering is:

$$P_{IC} = \frac{4}{3}\sigma_T c\gamma^2\beta^2 U_{ph} \quad \text{Eq. 1.4}$$

Where  $\sigma_T$  is the Thomson cross section,  $\beta = v/c$ , and  $U_{ph}$  is the energy density of the seed photon field [24]. The cross section for IC scattering can be approximated as the Thomson cross section for lower energy photons in the rest frame of the electrons ( $h\nu \ll mc^2$ ) and as the Klein-Nishina cross section for photons at energies comparable to the electrons rest mass or higher. The latter case is known as the Klein-Nishina regime [25].

Synchrotron Self-Compton (SSC) is the process where photons produced by the Synchrotron process are scattered to higher energies by the same population of charged particles that produced them [24].

### 1.4.3. Curvature Radiation

Synchrotron radiation, as mentioned previously, occurs for a particle accelerating perpendicular to the magnetic field. Curvature radiation, on the other hand, occurs with a charged particle changing energy along a path parallel to the magnetic field. This is an important process for understanding high energy emission in pulsars, as charged particles

tend to travel along the dipole field lines. Like Synchrotron radiation, there is a peak frequency in a curvature spectrum [14]:

$$\nu_c = \frac{3}{2} \frac{c\gamma^3}{R_c} \quad \text{Eq. 1.5}$$

where  $R_c$  is the radius of curvature. Equation 1.5 evaluated for typical pulsar values with electrons in the TeV energy range give photons in the GeV range. However, those photons can be attenuated by the magnetic field and create  $e^+/e^-$  pairs. The power of curvature radiation integrated over all frequencies is [26]:

$$P_{cur} = \frac{2}{3} \frac{q^4}{R_c^2 m c^2} \beta^3 \gamma^4. \quad \text{Eq. 1.6}$$

#### 1.4.4. Bremsstrahlung Radiation

Bremsstrahlung (a word meaning “breaking” in German, also known as free-free emission) radiation is associated with the de-acceleration of electrons in the electrostatic fields of ions and atomic nuclei [24]. This is an important physical process for atmospheric air showers (see section 4.2), but not a major process in VHE astrophysics. Relativistic Bremsstrahlung is an energy loss mechanism important for TeV energy electrons that are capable of generating soft gamma rays.

#### 1.4.5. Pion Production and decay

Pions are a by-product of violent interactions between protons at high energies and other protons or nuclei. From this interaction, neutral pions ( $\pi^0$ ) and an equal number of positive and negative charged pions ( $\pi^+, \pi^-$ ) are produced. The neutral pions will decay into a pair of gamma rays after a mean lifetime of  $8.4 \times 10^{-17}$  seconds, while the charged pions will decay into charged muons, which will decay into electron/positron pairs.



Pion decay plays an important role in VHE astrophysics and in the study of cosmic ray physics. Models of astrophysical objects that include neutral pion decay as the source of gamma rays are referred to as Hadronic, since protons and pions are Hadrons. The presence of neutrinos, a product of the charged pion decay could be used to distinguish hadronic models from leptonic ones [27].

#### 1.5. Outline of the remainder of work

PWN have broadband emission throughout the EM spectrum, but not all of them can be seen with the sensitivity of the current generation of VHE experiments and in some cases, the PWN may not be energetic enough to be seen in VHE at all. If we have a better understanding of the emission from PWN at their highest energies, then it will give some constraints to the emission models of these objects. Further constraints are possible if the pulsar itself within these objects can be detected. For example, Fermi and MAGIC observations of the Crab Pulsar show a cutoff of the pulsar in the range of 10 to 20 GeV as shown in figure 1-4. This cutoff can constrain how far from the NS emission takes place, since curvature photons can be attenuated by the higher magnetic field close to the NS surface. If pulsations are found in TeV PWN, that would imply that photons are being created by curvature processes further away from the NS surface [28].

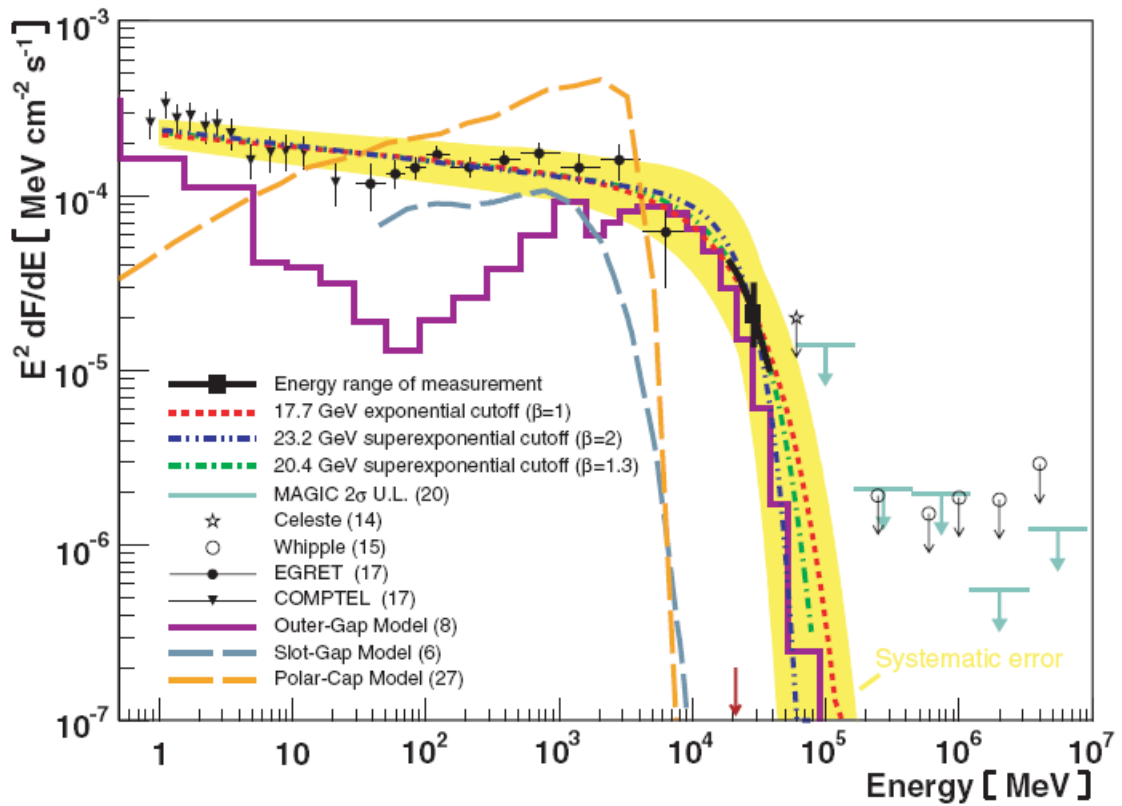


Figure 1-4. A Broadband spectrum of the Crab pulsar [28].

The remainder of this work will attempt to answer the question: ‘which PWN and the pulsars within them will be able to be seen at VHE energies and which cannot?’ Chapter 2 will cover background information on pulsars and PWN. Chapter 3 will cover ACTs and the principles behind how they work. This will focus mostly on VERITAS and the data analysis package VEGAS, since they will be utilized in the chapters that follow it. Chapter 4 discusses the current trends in VHE PWN and selection criteria for observations in this work. Chapter 5 discusses the observations of young energetic PWN and their associated pulsars with VERITAS and the results of those observations. Finally, conclusions from this work are discussed in Chapter 6.

## CHAPTER 2. PULSAR WIND NEBULAE

### 2.1 Stellar Evolution

#### 2.1.1. The Lifetime of a Main Sequence Star

Stars are born from the interstellar gas and dust that exists between stars, which is mostly hydrogen but contains trace amounts of helium and heavier elements. A molecular cloud exceeding a density limit will collapse due its own internal gravitational potential, and a protostar is born. From this time onward, the internal pressure will balance the gravitational pull of the center of the star to prevent collapse of the star, a state known as hydrostatic equilibrium. The temperature in the core of the star increases due to pressure, and reaches the point where nuclear reactions begin to occur. Hydrogen is converted into helium in the first proton-proton chain (or PP I) and the Carbon-Nitrogen-Oxygen (CNO) chain, which uses  $^{12}_6\text{C}$ ,  $^{14}_7\text{N}$  and  $^{15}_8\text{O}$  in the CNO chain [29].

At this point, the star's luminosity is maintained by nuclear energies. The evolution of most stars can be predicted with the assistance of a Hertzsprung-Russell diagram (also referred to as a H-R diagram, seen in figure 2.1). The H-R diagram plots the temperature of the star (determined by color or spectral type) vs. the apparent magnitude of the star. The long line going from top left of the H-R diagram to the lower right is called the main sequence, where most stars spend the majority of their lifetimes. Eventually, the hydrogen in the core will be completely burned up in PP and CNO processes until the core is dominated by Helium. This will occur at an age of 9.3 billion years for a star with mass equal to our sun. Since the mean molecular weight has increased the density at the core has increased, resulting in a release of gravitational potential energy. According to the virial theorem, half of that energy will be converted to kinetic energy and hence an

increase in temperature. However, not all energy reaches the star's surface and goes towards slow expansion of the envelope causing a decrease in surface temperature and the star will start moving to the right in the H-R diagram, a region known as the sub-giant branch [29].

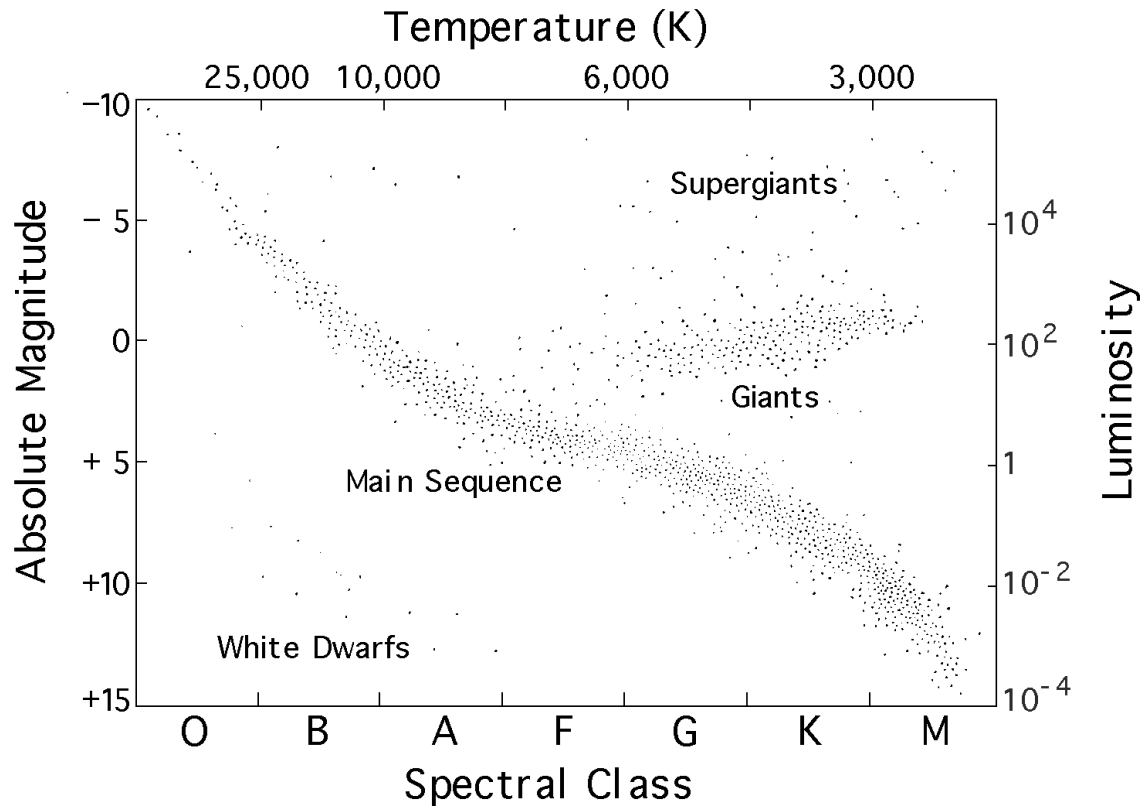


Figure 2-1. Typical H-R diagram. Credit: NASA/CXC/SAO

At this point, the star will move off of the main sequence and the rest of the star's lifetime proceeds relatively quickly. Eventually the electrons at the core will become degenerate (see next section) and the core is held up by degeneracy pressure of free electrons. The temperature in the core will rise to the point where the triple alpha process occurs, where Helium is fused into Carbon. The release of energy due to Helium burning will transfer energy to the surface where it will cause further expansion of the envelope and cooling of the star's surface. This will eventually lead to the burning of Carbon into

Oxygen and heavier elements, and the heavier elements will burn, eventually leading to a core of Iron. The star is now in the red giant branch of the H-R diagram [29].

A profile of a star at this point will look something like an onion: an Iron core, with layers outwards of lighter metals and with a layer of Hydrogen at the upper envelope. Each successive element being burned results in less and less energy being produced per unit mass with the timescale of the burning becoming shorter. The core of the star is now under extreme temperature and pressure, causing the free electrons that held the core through degeneracy pressure to be ‘captured’ by protons and form neutrons:



This process, known as inverse beta decay, occurs when the electron’s energy exceeds the difference in energy between the proton and neutron. Neutrinos created in equation 2.1 carry away a large amount of energy from the core of the star. Additional neutrons are created through photodisintegration, where a high energy photon can split heavy nuclei. At this point, the core collapses rapidly, due to the loss of the Iron core and degeneracy pressure. A shock wave forms at the core due to the strong nuclear force at the core becoming repulsive, a result of the Pauli Exclusion Principle applied to neutrons. This shock will pass through the outer core into the envelope. This collapse, followed by the shock exploding out of the star’s surface is known as a supernova. Specifically, what was described here is a Type II supernova, due to the presence of hydrogen lines and heavier elements in the emission spectra. Type II supernovae are divided into Type II-L or Type II-P for a linear or plateau shaped light curve, respectively. Type I supernovae, on the other hand, do not contain prominent hydrogen lines. Type I are further divided into Type Ia which show a strong Si II line, and those without it are divided into Type Ib or Type Ic depending on the presence or absence of strong Helium lines, respectively [29].

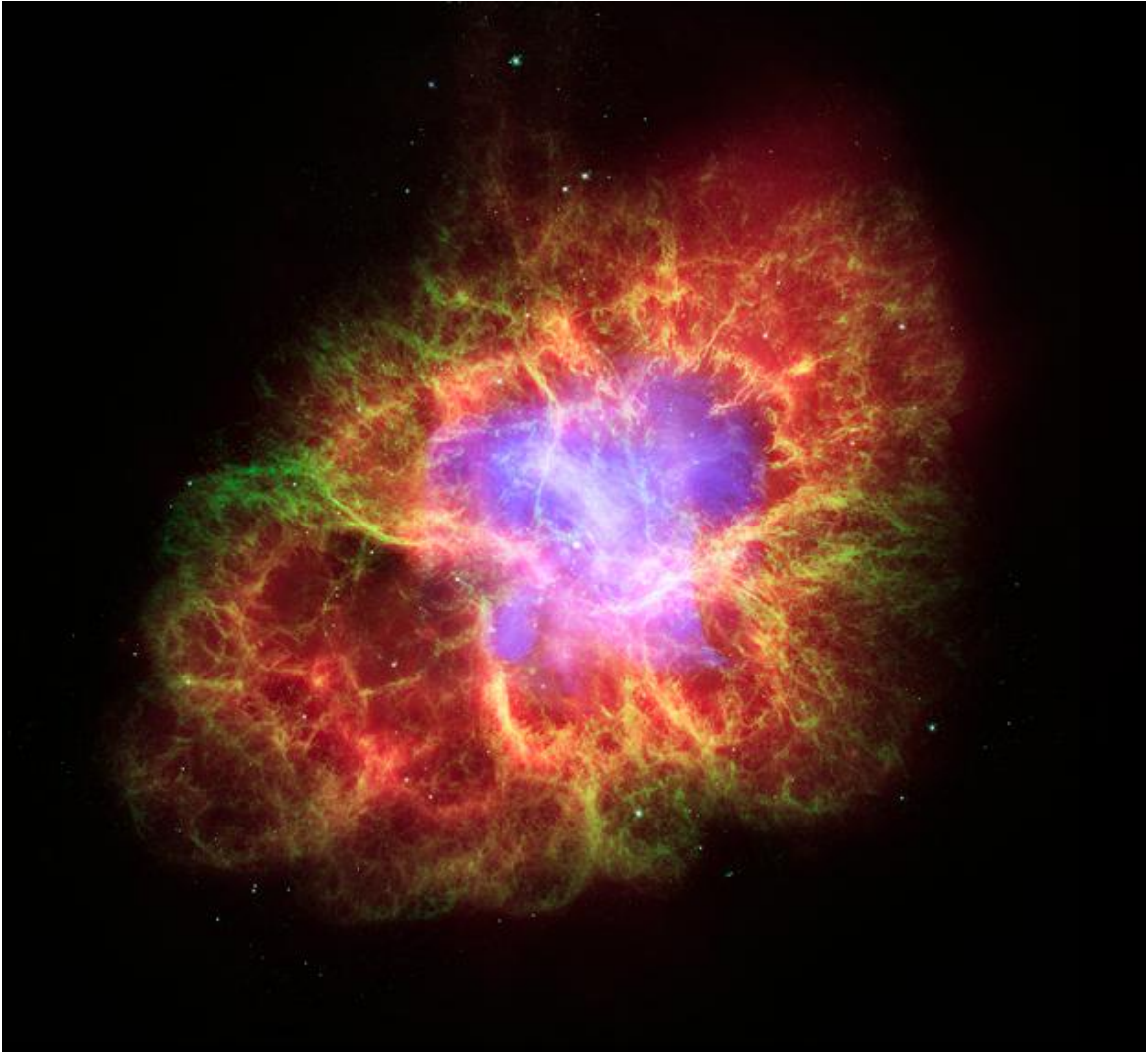


Figure 2-2 Image of the Crab SNR shown in three wavelengths. The Chandra X-ray image is shown light blue, while Spitzer IR is red, and the Hubble Space Telescope image is dark blue and green. Credit: X-ray: NASA/CXC/ASU/J. Hester & A. Loll; Optical: NASA/ESU/ASU/J. Hester & A. Loll; Infraed: NASA/JPL-Caltech/Univ. Minn./R. Gehrz.

### 2.1.2. The Physics of Degenerate Matter

An understanding of degeneracy pressure is required to understand neutron stars or white dwarfs, so an aside will be taken here to explain it. According to the Pauli Exclusion Principle from quantum mechanics, no two fermions can occupy the exact same quantum state. Electrons and neutrons are both fermions, defined as particles with odd half integer

spins. Now suppose you had a box of a fermion gas, the energies of the particles in the box would effectively be those of a 3-dimensional square well:

$$E = \frac{\hbar^2 \pi^2}{2mL^2} (n_x^2 + n_y^2 + n_z^2). \quad \text{Eq. 2.2}$$

A particle in this box could have states  $n_x = 1, n_y = 0, n_z = 0$ , and have the same energy as another particle in states  $n_x = 0, n_y = 1, n_z = 0$ . These two states would be considered degenerate, meaning that the two different states have the same energy. If the particles in the box were at low enough temperatures, the particles will fill up the lowest energy states and only occupy the higher states if all the lower states were already occupied. Therefore, the highest possible occupied state would be the fermi energy:

$$\varepsilon_f = \frac{\hbar^2}{2m} (3\pi^2 N)^{2/3}. \quad \text{Eq. 2.3}$$

Where  $N$  is the number of fermions per unit volume [30].

When this information is combined with the Heisenberg uncertainty principle, we find that a degenerate gas exerts a pressure on its surroundings. The 3-dimensional box will be continued to be used as an example. The momentum of particles in the box is quantized as  $\vec{p} = \hbar \vec{n}/L$ . ( $\vec{n}$  is a vector with components  $\{n_x, n_y, n_z\}$ .) Electrons in the box are packed as tightly as possible, giving a separation of  $N^{-1/3}$ . With the Heisenberg relationship

$$\Delta x \Delta p \approx \hbar, \quad \text{Eq. 2.4}$$

the average momentum for a particle can be approximated as  $\hbar N^{1/3}$ . If we assume that all particles have the same momentum, then pressure can be approximated as:

$$P \approx \frac{1}{3} N p v \quad \text{Eq. 2.5}$$

Combining the pressure equation, and estimate for momentum for a classical gas, we get an equation of state for a degenerate gas:

$$P = \frac{\hbar^2}{3m} \left(\frac{\rho}{m}\right)^{5/3} \quad \text{Eq. 2.6}$$

In the extreme relativistic limit,  $v \sim c$  and the equation of state is then [14]:

$$P = \frac{\hbar^2 c}{3m} \left(\frac{\rho}{m}\right)^{4/3} \quad \text{Eq. 2.7}$$

### 2.1.3. Life After Death for a Star

There are a few different paths that a star can take as it gets older: white dwarfs, neutron stars, or black holes. A trend does exist on which one of the three it might become, depending on its mass. Less massive stars typically become white dwarfs, which are stable due to the balance of electron degeneracy pressure with gravitational pressure of its own mass. They occupy the lower left corner of the H-R diagram. There is an upper limit for the mass of a white dwarf, known as the Chandrasekhar limit, above which a white dwarf cannot form. The Chandrasekhar limit can be approximated by equating equation 2.7 for electrons with the hydrostatic pressure of a sphere of uniform density ( $P = \frac{2}{3}\pi G\rho^2 R^2$ ) and solving for mass, or about 1.44 solar masses [14].

The more massive stars ( $M > 10M_{\odot}$ ) tend to become black holes that form when the gravitational pressure overtakes electron and neutron degeneracy pressure, and the star collapses into a single point, known as a singularity. General Relativity explains that gravity is simply the curvature of space-time, and mass (and energy) determines the amount of curvature. When a massive object collapses into a singularity, anything that falls into the black hole cannot escape. The barrier which objects cannot escape is defined by the Schwarzschild radius, which only depends on the mass of the black hole:



$$r_s = \frac{3GM}{c^2} \quad \text{Eq. 2.8}$$

Stars that are between the Chandrasekhar limit and less than 10 solar masses typically become neutron stars. As mentioned previously, neutrons can form by the capture of electrons by protons in stellar cores. Since neutrons are also fermions, neutron degeneracy pressure can also exist in stellar cores. This pressure is much less than electron degeneracy pressure, due to the greater mass of the neutron. The lesser neutron degeneracy pressure implies that a neutron star can exist with a higher mass than a white dwarf without collapsing into a black hole [29].

## 2.2. Characteristics of Pulsars:

A Pulsar is a type of neutron star that rotates rapidly, and characterized by a large magnetic field. The high frequency is a result of conservation of angular momentum during the collapse of the stellar core, where the size of the iron core is suddenly decreased, requiring the angular frequency to increase. As a pulsar ages, it spins more slowly and loses rotational kinetic energy. This rotational kinetic energy is transferred to the particles in the surrounding medium, which is believed to fuel the radiation seen throughout the EM spectrum. Additionally, a pulsar is essentially a magnetic dipole, so making the dipole approximation we can infer knowledge about the electrodynamics of pulsars.

With some reasonable assumptions and the period and period derivative information, some important physical quantities can be derived for pulsars. It is assumed that all pulsars have mass of one solar mass, and a perfect sphere of radius of 10km, making the moment of inertia ( $I = \frac{2}{5}MR^2$ )  $\sim 10^{45}$ g. These approximations come from an order of magnitude estimate from the Chandrasekhar limit, and the radius that results when the equation of state for degenerate neutrons (Eq. 2.6) is equated with hydrostatic pressure [14].

### 2.2.1. Spin-down Luminosity

Spin-down luminosity, the rotational energy loss rate for the pulsar, is simply the time derivative of the rotational kinetic energy:

$$L_{rot} = \frac{d}{dt} \left( \frac{1}{2} I \omega^2 \right) = I \omega \dot{\omega} = -I \frac{4\pi^2}{P^3} \dot{P} \quad \text{Eq. 2.9}$$

where  $I$  is the moment of inertia,  $P$  is the period of rotation for the pulsar,  $\dot{P}$  is the time derivative of the period, and  $\omega$  and  $\dot{\omega}$  is the angular frequency and angular frequency time derivative, respectively. The result of equation 2.9 is significant because it is roughly the entire ‘power budget’ for the pulsar. It is this energy that is transferred into the pulsar wind and magnetic field that fuels a PWN.

### 2.2.2. Pulsar Age

The age of the pulsar can also be estimated from  $P$  and  $\dot{P}$  information. The angular frequency of the pulsar,  $\omega$ , varies with time as:

$$\dot{\omega} = -k\omega^n \quad \text{Eq. 2.10}$$

where  $k$  is a positive constant, and  $n$  is also a positive constant, known as the braking index. Using separation of variables, we can solve this equation for time:

$$-k\tau = \frac{1}{1-n} (\omega^{1-n} - \omega_0^{1-n}) \quad \text{Eq. 2.11}$$

Solving equation 2.10 for  $k$  and doing some algebra gives us:

$$\tau = \frac{1}{n-1} \left( \frac{\omega}{\dot{\omega}} \right) \left( 1 - \left( \frac{\omega}{\omega_0} \right)^{n-1} \right) \quad \text{Eq. 2.12}$$

At this point, some assumptions need to be made. First, the braking index will be exactly three, which is the correct value if a pulsar is a perfect magnetic dipole. Although the braking index has only been measured precisely for very few pulsars, (a measurement of  $\ddot{\omega}$  is needed, requiring a very long observation), the braking index measured has been roughly that value. The second approximation is that  $\omega \ll \omega_0$ , which holds true for older pulsars. This approximation in equation 2.12 gives us the characteristic age of the pulsar:

$$\tau_c = \frac{P}{2\dot{P}} \quad \text{Eq. 2.13}$$

### 2.2.3. Magnetic Field

By using the dipole approximation for the pulsar and equating the spin-down luminosity to the dipole radiation rate, found by the Larmor formula:

$$L_{B,dip} = \frac{2|\ddot{\mu}|^2}{3c^3} = \frac{2\omega^4\mu_{\perp}^2}{3c^3} = \frac{2\omega^4\mu^2\sin^2\alpha}{3c^3} \quad \text{Eq. 2.14}$$

The dipole component perpendicular to the rotational axis rotates with the pulsar, so it varies sinusoidal with period equal to the period of the pulsar. The perpendicular component is  $\mu_{\perp} = \mu \sin \alpha$ , where  $\alpha$  is defined as the angle between the rotation axis and the magnetic dipole axis. Note that if the rotational axis and magnetic axis were aligned ( $\alpha = 0$ ), that the dipole radiation shuts off.

The magnetic field from a dipole is:

$$\vec{B}(r, \theta, \mu) = \frac{2\mu}{r^3} (2 \cos(\theta) \hat{r} + \sin(\theta) \hat{\theta}) \quad \text{Eq. 2.15}$$

Where  $\theta, r$  are spherical coordinates in the frame where the magnetic moment,  $\mu$ , points in the  $\hat{z}$  direction. Dipole radiation on the surface can be expressed in terms of the surface magnetic field, exploiting that the mean surface field averaged over polar angle is

$B_0 = 2\mu/R^3$ . By setting the equations for dipole radiation and spin down power equal, the surface magnetic field can be found:

$$L = I\omega\dot{\omega} = \frac{\omega^3 B_0^2 R^6 \sin^2 \alpha}{6c^3} \quad \text{Eq. 2.16}$$

By solving this expression for  $B_0$  and using the assumed mass and radius of a pulsar:

$$B_0 = \left[ \frac{3}{5\pi^2} c^3 R^{-4} M P \dot{P} \right]^{\frac{1}{2}} / \sin \alpha \quad \text{Eq. 2.17}$$

$$B_0 \approx 1.8 \times 10^{18} (P_{[s]} \dot{P})^{\frac{1}{2}} / \sin \alpha \text{ Gauss}$$

where  $P_{[s]}$  is period in units of seconds. By taking advantage of the  $B \sim r^{-3}$  relationship, we can find the polar averaged magnetic field at any radius  $r$  away from the pulsar center [31]:

$$\langle B_r \rangle = \frac{B_0 R^3}{r^3} \quad \text{Eq. 2.18}$$

#### 2.2.4. Light Cylinder Surface

The light cylinder is defined as a surface that limits where a particle is allowed to co-rotate with the pulsar. A particle is forbidden from rotating with the pulsar beyond the light cylinder surface because it would exceed the speed of light. The light cylinder surface is defined by the boundary  $r = \pm c/\omega$  or:

$$r_l = \frac{cP}{2\pi \sin(\theta)} \quad \text{Eq. 2.19}$$

The light cylinder serves an important purpose; it defines zones of particle populations and fields around the pulsar. The near zone, for example, is defined as everything within the light cylinder, also called the magnetosphere.

### 2.2.5. Charge Density and the Null Charge Line

In the co-rotating reference frame of the pulsar, the electric field is:

$$\vec{E} = -\frac{(\vec{\omega} \times \vec{r})}{c} \times \vec{B}. \quad \text{Eq. 2.20}$$

For a magnetic dipole spinning in the  $\vec{z}$  direction and utilizing equation 2.14 would give an electric field of:

$$\vec{E} = \frac{4\pi\mu}{Pr^2} (\sin^2\theta \hat{r} + \sin 2\theta \hat{\theta}). \quad \text{Eq. 2.21}$$

The scalar potential is given by Laplace's equation:

$$\nabla^2 \Phi(r, \theta, \varphi) = 0. \quad \text{Eq. 2.22}$$

In spherical coordinates, the solutions have the form:

$$\Phi(r, \theta) = \sum_{l=1}^{\infty} \left( \frac{A_l}{r^{l+1}} + B^l r^l \right) P_l(\cos \theta). \quad \text{Eq. 2.23}$$

All of  $B_l$  would have to be zero, to maintain the boundary condition that  $\Phi \rightarrow 0$  as  $r \rightarrow \infty$ . In equation 2.23,  $P_l(\cos \theta)$  is the Legendre polynomial of order  $l$  (not to be confused with period of the pulsar). Equating equation 2.21 and then taking the gradient of equation 2.23, Exploiting the boundary conditions that the fields need to be continuous at  $r = R$ , we can solve for  $A_l$ :

$$E_\theta = \frac{4\pi\mu}{PR^2} \sin 2\theta = \frac{1}{r} \frac{\partial \Phi}{\partial r} = -\frac{A_1}{R^3} \sin \theta + \frac{3A_2}{R^4} \cos \theta \sin \theta + \dots \quad \text{Eq. 2.24}$$

By matching both sides of the equation,  $A_2 = 8\pi\mu R^2/3P$ , with all other  $A_l = 0$ , with the exception of  $A_0$ , which dropped out because of the derivative in equation 2.14.  $A_0$  is found with the  $\hat{r}$  direction of the electric field, giving the potential as:

$$E_{r=R} = \frac{\partial \Phi}{\partial r} = \frac{4\pi\mu}{PR^2} \sin^2 \theta = -\frac{A_0}{R^2} - \frac{3A_2}{R^4} P_2(\cos \theta).$$

Finally, the potential for a magnetic dipole is found:

$$\Phi(r, \theta) = \frac{8\pi\mu}{3P} \left( \frac{1}{r} - \frac{R^2}{r^3} P_2(\cos \theta) \right). \quad \text{Eq. 2.25}$$

This can be expressed in terms of the surface magnetic field, exploiting the mean surface field averaged over polar angles (which is  $B_0 = 2\mu/R^3$ ):

$$\Phi(r, \theta) = \frac{4\pi B_0 R^3}{3P} \left( \frac{1}{r} - \frac{R^2}{r^3} P_2(\cos \theta) \right). \quad \text{Eq. 2.26}$$

The charge density can be found through Gauss's law:

$$\rho = \frac{1}{4\pi} \vec{\nabla} \cdot \vec{E} = -\frac{1}{4\pi} \vec{\nabla} \cdot \left( \frac{\vec{\omega} \times \vec{r}}{c} \times \vec{B} \right). \quad \text{Eq. 2.27}$$

The electric field in the co-rotating frame (Equation 2.20) was used. Using vector calculus identities:

$$\rho = \frac{1}{4\pi c} \vec{B} \cdot \left( \vec{\nabla} \times (\omega r \sin(\theta) \vec{\phi}) \right) - \frac{1}{4\pi c} \omega r \sin(\theta) \vec{\phi} \cdot \left( \vec{\nabla} \times \vec{B} \right) \quad \text{Eq. 2.28}$$

The cross product in the first term in equation 2.28 simplifies to  $2\vec{\omega}$ , and the cross product in the second term is  $4\pi\vec{j}$ , through Ampere's law.  $\vec{j} = \frac{\rho\vec{v}}{c} = \frac{\rho\vec{\omega} \times \vec{r}}{c}$ , leading to our final result:

$$\rho_0 = \frac{1}{2\pi c} \frac{\vec{B} \cdot \vec{\omega}}{[1 - (r/r_l)^2]} \quad \text{Eq. 2.29}$$

The result in equation 2.29 is commonly referred to as the Goldreich-Julian density [32].

The Goldreich-Julian density shows that there is a surface defined by  $\vec{B} \cdot \vec{\omega} = 0$ , where the charge density is zero, known as the null-charge surface. The null charge surface separates the magnetosphere into regions of positive and negative charge densities.

### 2.3. Pulsar Particle Acceleration Models

Pulsars have been seen throughout the electromagnetic spectrum for the past 40 years (as of this work). However, explanations behind their emission are still not completely understood. While most experts agree that spin-down powers pulsar wind nebulae (PWN), how that energy is transferred to the individual particles (and which kind) that cause the emission is still debated. At  $\gamma$ -ray energies, most do agree on lepton emission through either the Polar Cap or Outer Gap models that will be discussed in the following sections. A few selected other models will also be discussed briefly.

#### 2.3.1. Polar Cap Model

The polar cap model assumes that particles are accelerated along magnetic field lines from polar caps. Polar caps are regions on the NS surface from which open magnetic field lines emanate, near the rotation axis. Open field lines extend beyond the light cylinder surface to a near infinite distance from the neutron star. Particles that travel along those magnetic field lines will not return to the pulsar. The angular size of the polar cap region can be approximated by:

$$\theta_p \approx (R/r_l)^{1/2}. \quad \text{Eq. 2.30}$$

The radius of the polar cap is:

$$R_p \approx \theta_p R \approx R^{3/2} r_l^{-1/2}. \quad \text{Eq. 2.31}$$

There are two polar caps for a pulsar, a positively charged one and negatively charged one. This is determined by the Goldreich-Julian density.

Charged particles flow from the polar cap surface to beyond the light cylinder surface along magnetic field lines, accelerated by electric fields that run parallel to the magnetic fields. Curvature radiation is the primary emission process for leptons [34], [35]. Many models consider the transverse electric field to be negligible, so synchrotron emission is mostly ignored. Many of the energetic curvature photons produced close the neutron star pair produce with the strong magnetic field. Pairs produced in this manner (known as secondary pairs) are traveling nearly parallel with the magnetic field along with the primary leptons. The secondary leptons produce more curvature photons, some of which attenuate on the magnetic field and the process can repeat several times, forming a pair producing cascade [36].

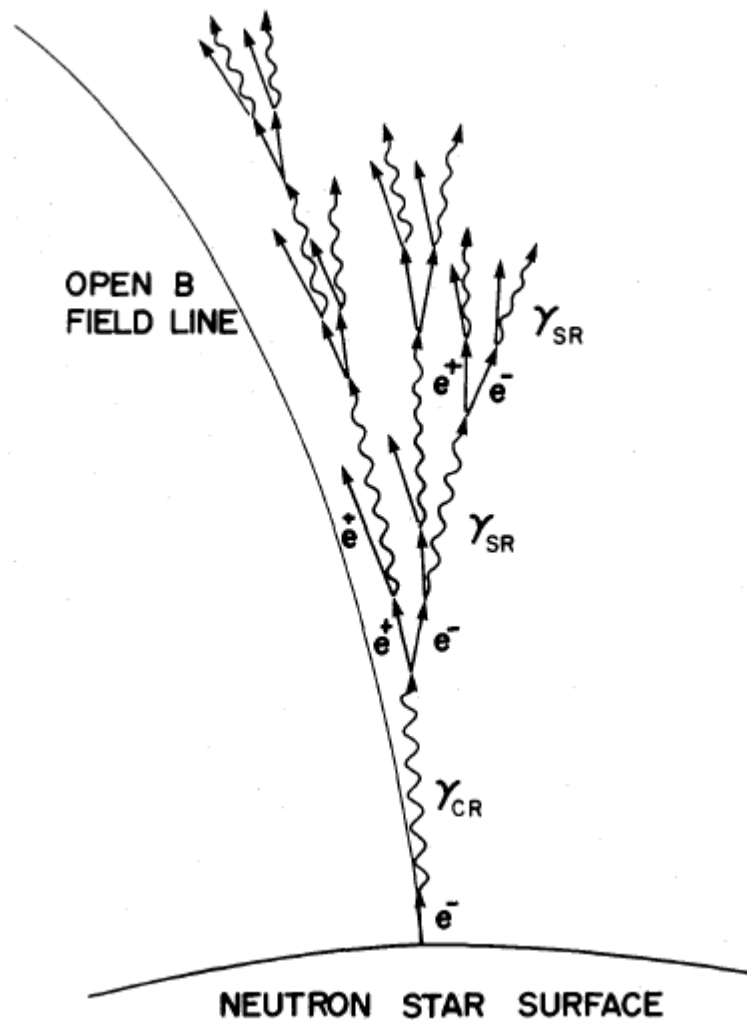




Figure 2-3. Illustration of the pair production cascade present in polar cap models. The electron closest to the NS surface emits curvature radiation ( $\gamma_{cr}$ ) which pair produces on the magnetic field, creating leptons which repeats this process [37].

### 2.3.2. Outer Gap Model

The basis for the outer gap model is if the charge density would differ from the Goldreich-Julian density in any region in the magnetosphere, it would cause a large potential drop along the magnetic field lines that would move charge into the deficient (or excess) region. This would create electrostatic ‘gaps’ far from the neutron star, where the co-rotating magnetosphere would be a significant fraction of  $c$ . In a region of positive charge density, the gap region would be an effective region of negative charge density. If this occurs near the null surface, then charges on the other side of the null surface will be repulsed and a vacuum gap forms. Positive charge will be pulled through the light cylinder surface to fill in the gap. The gap has boundaries formed by the null-charge line, the last closed magnetic field line and the light cylinder as seen in figure 2-3. If the gap were to terminate in a region with  $\rho_c \neq 0$ , charges would flow in and destroy the gap. The maximum voltage that supplies this current flow is:

$$\Delta\Phi \approx \frac{\omega^2 R^3 B_0}{c^2}. \quad \text{Eq. 2.32}$$

Vacuum gap growth is limited by  $e^\pm$  plasma production. Inside the gap, the Lorentz invariant  $\vec{E} \cdot \vec{B} \neq 0$ , implying a region of acceleration for charged particles within the gap moving along the field lines. Equation 2.32 also implies that electrons are accelerated to energies where they can emit  $\gamma$ -rays.  $\gamma$ -rays are produced either through curvature radiation, IC scattering or synchrotron emission from extremely relativistic electrons. These  $\gamma$ -rays pair produce by collisions with ambient X-rays for photons at GeV energies, IR or optical photons for TeV energy  $\gamma$ -rays. A third way of pair production is interactions of  $\gamma$ -rays with the magnetic field. This form of attenuation is more likely to occur closer to the NS, however. In the outer magnetosphere, where magnetic fields are

in the range of  $10^4$ - $10^5$ G, a  $\gamma$ -ray would have to be above 100 TeV in order to pair produce [38].

Since electrons and positrons are accelerated due to electric fields along magnetic field lines, they lose energy due to curvature radiation. The curvature radiation pair produces (gap secondary pairs) with X-rays, beyond the outer gap but within the light cylinder. Synchrotron radiation of the secondary pairs is the source of the X-rays. Inverse Compton scattering of X-rays with the secondary pairs is the source of  $\gamma$ -rays. The resulting radiation should be beamed tangentially from the edge of the gap through the light cylinder surface. This model explains pulsed behavior as beamed from the edge of the gap as opposed to the polar cap region in the polar cap model.

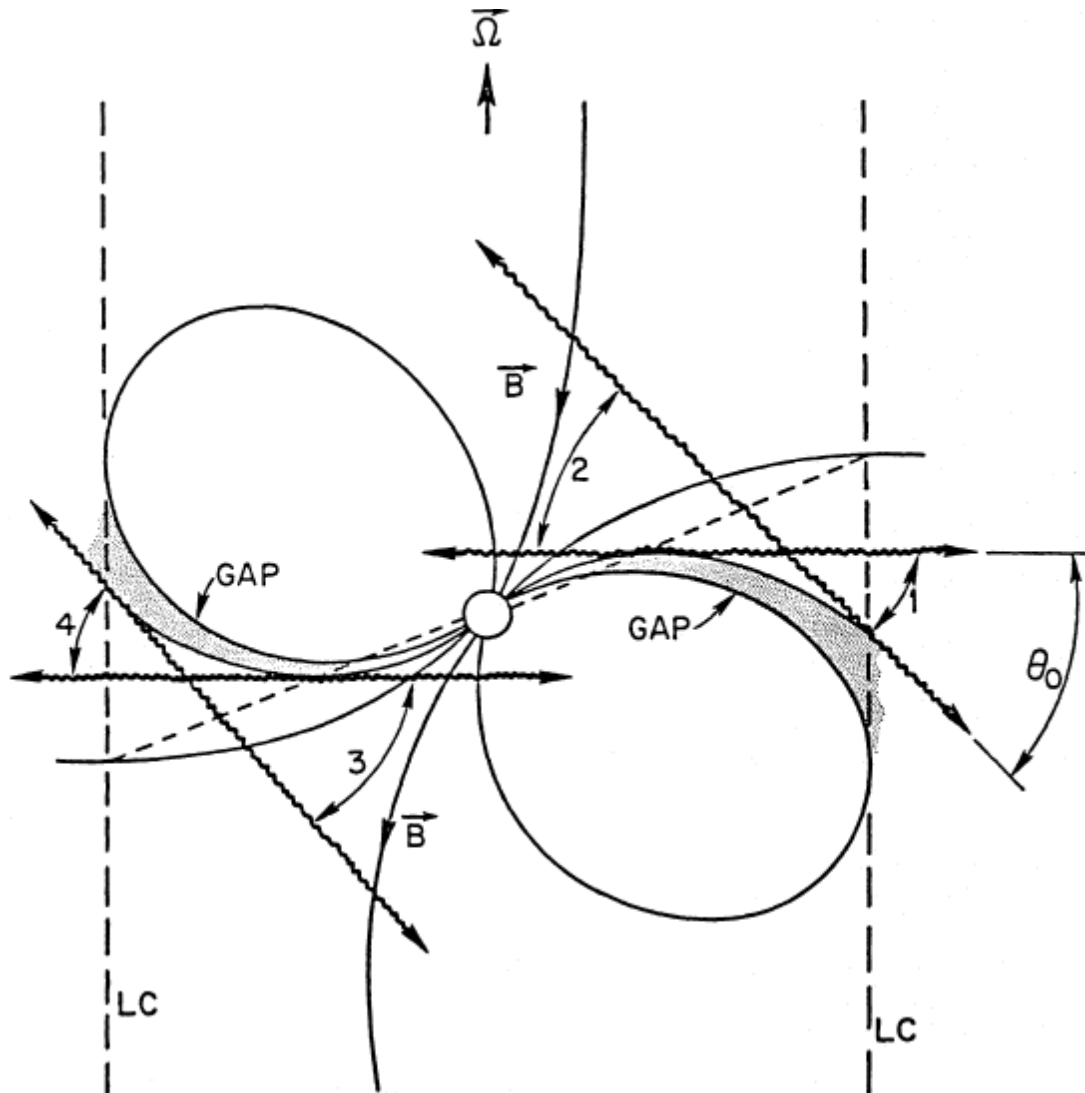


Figure 2-4 Outer gap magnetosphere with gap regions shaded in gray. The gaps have the last closed magnetic field line, the null surface, and the light cylinder as boundaries. [39]

### 2.3.3. Co-rotation model

The co-rotation model [40] assumes that acceleration of leptons is due to co-rotating close to (but still within) the light cylinder. The model uses an idealized monopole-like magnetic field near the LC surface where the parallel electric component is nearly screened out. Inertial effects become important in describing the plasma dynamics. Co-rotation is only possible if the kinetic energy density does not exceed the magnetic field

density, known as the Alfvén co-rotation condition. This condition puts a limit on the maximum Lorentz factor of the electrons:

$$\frac{B_{LC}^2}{8\pi} > \gamma M \rho_0 m_e c^2 \quad \text{Eq. 2.33}$$

where  $M$  represents the multiplicity (ratio of secondaries to primaries),  $\gamma$  the Lorentz factor, and  $B_{LC}$  magnitude of the magnetic field evaluated at the light cylinder surface. Solving for  $\gamma$  gives:

$$\gamma_{max,e} = 4 \times 10^5 \frac{B_{LC,[G]} P_{[s]}}{M \cos \alpha}. \quad \text{Eq. 2.34}$$

The subscript  $G$  indicates magnetic field in Gauss and  $s$  is for the period in seconds. Curvature radiation losses also limit acceleration close to the light cylinder surface.

Curvature and synchrotron output would then be consistent with Fermi/Egret observations, while IC scattering in the Klein-Nishina regime of soft thermal photons would be consistent with the power output at TeV energies [40].

#### 2.3.4. Slot-Gap Models

Slot gap models were first introduced in 1979 [41] but have only recently gained attention as an extension to the polar cap model to explain the wider pulse profiles seen that cannot be easily explained by emission near the polar cap. The geometry of the slot gap (SG) is a region bounded by the last open field line and the field lines holding in the pair formation front (PFF), produced by attenuated curvature photons above the polar cap. The accelerating voltage for primary particles in the slot gap is weakly dependent on the period and magnetic field, dependant more on the moment of inertia of the NS and the angle between the magnetic moment and angular momentum,  $\alpha$ . The electric field

parallel to the magnetic field decreases with altitude from the NS surface and mostly gets screened out by the proximity to the two conducting surfaces surrounding the SG [41].

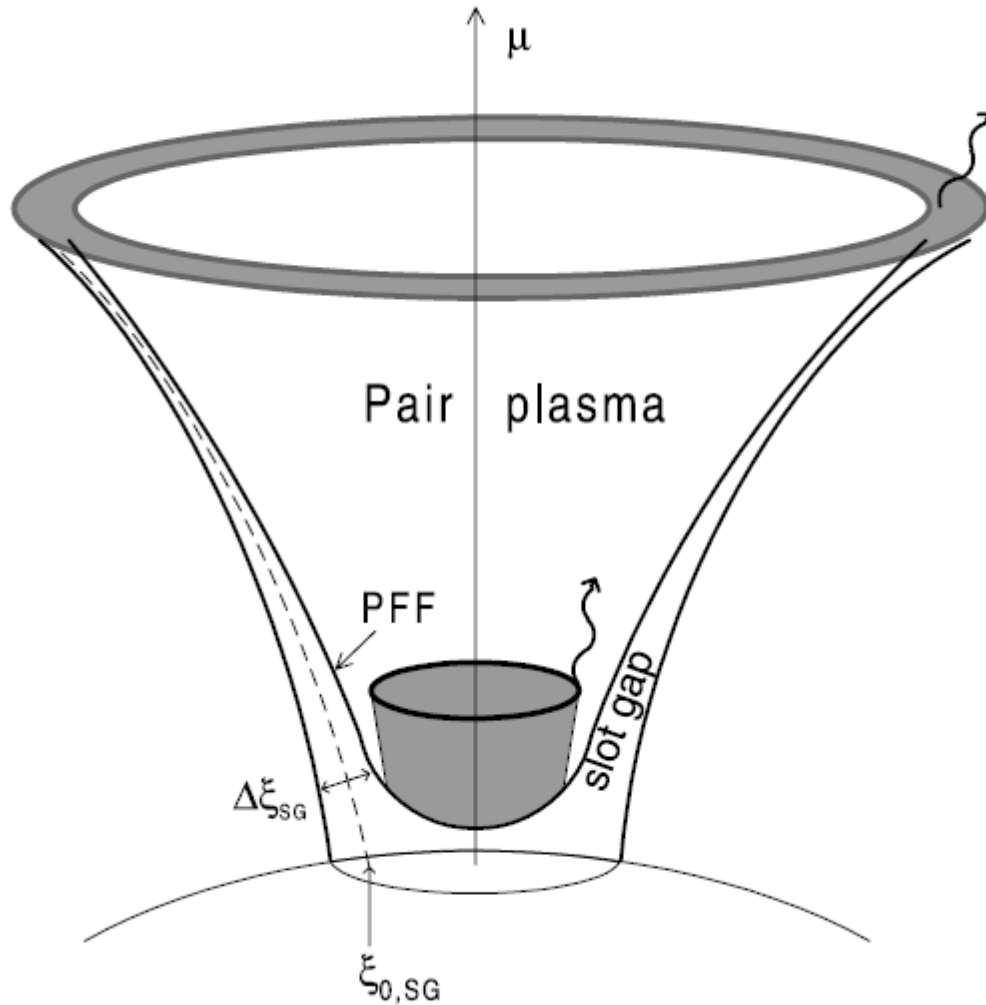


Figure 2-5 Depiction of the slot gap model. [42]

### 2.3.5. Hadronic Models

Hadronic models suggest that the source of  $\gamma$ -ray emission is neutral pion decay. The earliest versions of this model have protons, along with leptons, accelerated through gaps

such as the ones described in section 2.3.1. Protons are extracted from the stellar surface by inward moving electrons produced in the outer gap. The protons are accelerated by the electric field existing in the outer gap along magnetic field lines. The protons are beamed out of the magnetosphere where they collide with other protons in the nebula, creating pions. The power of VHE  $\gamma$ -rays is:

$$P_\gamma = \frac{1}{3} E_{total} R(\langle E_p \rangle). \quad \text{Eq. 2.35}$$

The factor of 1/3 comes from the multiplicity of neutral pions which is about 1/3 of the total pion multiplicity.  $E_{total}$  is the total integrated energy in the gap since the birth of the neutron star.  $R$  represents the rate of p-p collisions at a mean proton energy  $\langle E_p \rangle$ . The total energy in the gap is:

$$E_{total} = \int_0^{\tau_c} 1.2 \times 10^{38} P(t) dt \quad \text{Eq. 2.36}$$

Assuming a magnetic dipole, then  $P(t) = P(t/\tau_c)^{\frac{1}{2}}$ , then  $E_{total} \sim P^2 / \dot{P}$  or about  $8 \times 10^{46}$  ergs for Crab. The rate of p-p collisions is low, about  $4.5 \times 10^{-13} \text{s}^{-1}$ , assuming a particle density of  $\sim 500 \text{cm}^{-3}$  [43].

#### 2.4. Definition of a Pulsar Wind Nebula:

A Pulsar Wind Nebula is a nebula powered by the wind generated by a pulsar located within the supernovae remnant (SNR). The SNRs are typically shell-like because of a strong shock wave propagating (known as the forward shock) into the stellar medium or interstellar medium (ISM). They are also known as PWN or plerions (ancient Greek “pleres” meaning “filled” [44]). A PWN was originally defined by the following characteristics:

- Filled center or blob-like form (Reasoning behind name Plerion for PWN, [44])

- A flat radio spectrum where the radio energy flux is proportional to  $\nu^\alpha$ , with  $\alpha \sim 0$  to  $\sim -0.3$  (as opposed to  $\sim -0.45$  for other SNRs)
- A well-organized internal magnetic field
- High integrated linear polarization at high radio frequencies.

The growth of X-ray astronomy has added extra parameters to this definition [45]:

- A torus and jet near the pulsar, with the direction of the jet reflecting the direction of the pulsar spin axis and the torus showing an under luminous region inside a characteristic scale radius  $R_s \sim 10^{17}$  cm to  $\sim 10^{18}$  cm, believed to be the pulsar wind shock radius
- Evidence for synchrotron cooling (spectral steepening) with  $R > R_s$ , with the size of the PWN decreasing towards increasing energies, as seen from the Crab and several other PWN. The photon indices of the cooled spectra range between 2.0 and 2.5.
- Evidence for re-acceleration of particles somewhere between the pulsar light cylinder and  $R_s$ , leading to a hard X-ray spectrum with a photon index  $\sim 1.5$  to  $\sim 2$  near  $R_s$ .

### 2.5. Evolution of a PWN

After a SN explosion, the pulsar and the initial PWN around it is surrounded by an expanding SNR. Asymmetry in the supernovae gives the pulsar a velocity of  $\sim 400$  to  $500$  km/s. The direction that the pulsar travels in is due to asymmetry in the ISM at the time of the SN. The pulsar is embedded in slowly moving un-shocked ejecta. The wind from the pulsar is highly over-pressurized, causing the PWN to expand rapidly, moving supersonically and eventually driving a shock (known as the PWN shock) into the ejecta. This shock forms the outer boundary of the PWN. Assuming the PWN is roughly spherical in shape, the radius of the shock evolves with time as [46]:

$$R_{pwn} = 1.5 \dot{E}_0^{1/5} E_{SN}^{3/10} M_{ej}^{-1/2} t^{6/5} \quad \text{Eq. 2.37}$$

where  $\dot{E}_0$  is the initial spin-down energy of the pulsar,  $E_{SN}$  is the kinetic energy of the supernovae explosion and  $M_{ej}$  is the mass of the ejecta released in the SN. During this time, the PWN remains centered on the pulsar's position.

After the expanding SNR sweeps up a significant mass from the interstellar medium (ISM), it evolves to the ‘‘Sedov-Taylor’’ phase, in which energy is equally partitioned between thermal and kinetic contributions [47]. Now there is a forward shock where ambient gas is compressed and heated; and a reverse shock where ejecta is decelerated. The SNR interior is entirely filled with shock-heated ejecta. The reverse shock expands at first outward behind the forward shock, but eventually falls inward to the initial position of the PWN. If the remnant has no PWN, the reverse shock enters the SNR center after a time  $t_{sedov}$ , after the SN, which is on the order of a few thousand years. If the remnant contains a PWN, the reverse shock will collide with the PWN before that time. The reverse shock will compress the PWN which will respond with an increase of pressure and sudden expansion.

Once the reverberations between the PWN and SNR have faded, the pulsar once again powers the steadily expanding bubble. The PWN will expand into the hot shocked ejecta of the SNR at subsonic speeds. After this point, the pulsar may leave the SNR completely, leaving behind a ‘relic’ PWN and starting a new one around it. If this happens, the pulsar's space motion becomes supersonic and drives a bow shock through the SNR that may re-energize the SNR shell during the pulsar's passage. After leaving the SNR, the pulsar is surrounded by a mach cone and takes on a comet-like appearance at X-ray and radio wavelengths [47].

This chapter discussed pulsars and PWN in very general terms, without going into specifics about characteristics of any particular object. The rest of this work will discuss the observational results of a handful of these objects. The equations and ideas discussed here will still apply however, to attempt to bring together the VHE emitting PWN and the PWN that have not been detected in VHE into a larger framework.



## CHAPTER 3. ATMOSPHERIC CHERENKOV TECHNIQUE

### 3.1. Cherenkov Radiation

Cherenkov radiation is analogous to a ‘sonic boom’ but for light waves as opposed to sound. It is emitted whenever a particle has enough energy to travel faster than the speed of light in the medium that it is traveling in. It can only be viewed from a particular angle with respect to the particle’s velocity seen in the lower part of figure 3-1. This angle, known as the Cherenkov angle,  $\theta$ , is:

$$\cos\theta = c/nv_s \qquad \text{Eq. 3.1}$$

where  $n$  is the refractive index of the medium, and  $v_s$  is the speed of the particle. Equation 3.1 is known as the Cherenkov relation. When a charged particle travels through a dielectric medium at constant velocity it polarizes nearby molecules momentarily, afterwards the polarized molecules return to their initial positions, emitting brief pulses of EM radiation. When  $v_s > \frac{c}{n}$ , the pulses are emitted coherently, generating a Cherenkov wave front [14].

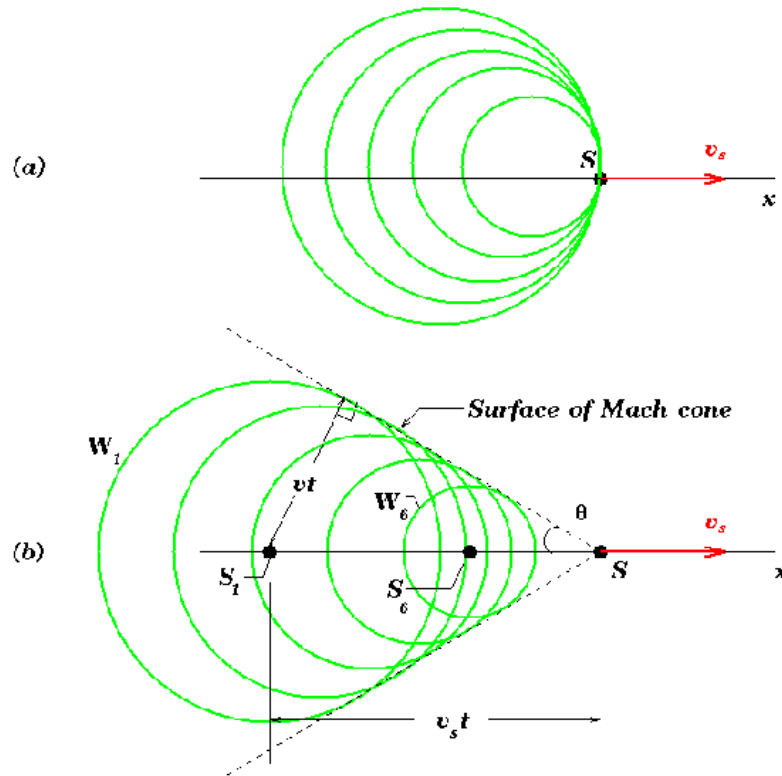


Figure 3-1. Illustration of Huygens construction for Cherenkov radiation

This concept is illustrated in figure 3-1. In that figure, the particle travels from  $S_1$  to  $S$  in a time  $t$ . At the same time, the wave front is emitted in all directions at speed  $c/n$  from the atoms at the location of the particle. Some simple trigonometry tells us that at a time  $t$  later after the particle passed:

$$\cos \theta = \frac{(c/n)t}{v_s t} = \frac{c}{n v_s}. \quad \text{Eq. 3.2}$$

Constructive interference from wave fronts created along every point in the path of the charged particle leads to the Cherenkov wave front. If  $v_s < c/n$ , the individual wave fronts never align to create constructive interference, as illustrated in the upper portion of figure 3-1 [14].

The Cherenkov relation tells us that there is a minimal energy for Cherenkov radiation to be emitted. The minimal velocity occurs when  $v_s = c/n$  and  $\theta = 0$ . Putting this into the equation for relativistic energy:

$$E_{min} = \frac{m_0 c^2}{\sqrt{1 - 1/n^2}} \quad \text{Eq. 3.3}$$

For an electron or positron (rest mass of 0.511MeV) moving in air (refractive index of 1.00028), this corresponds to a threshold energy of ~21 MeV. The other extreme is a particle traveling at ultra relativistic velocities,  $v_s \rightarrow c$ . That leads to a maximum angle of Cherenkov emission:

$$\theta_{max} = \cos^{-1} 1/n \quad \text{Eq. 3.4}$$

In air, this leads to a maximum Cherenkov angle of  $1.36^\circ$ .

### 3.2. Cosmic Ray Showers

In the upper atmosphere, gamma rays will interact with nuclei of atmospheric atoms and pair produce, creating an electron positron pair, as long as  $h\nu > 2m_e c^2$ . Pair production is typically not a spontaneous process, the atmospheric nuclei are necessary to conserve momentum. Because of the large momentum of the initial photon, the electron-positron pair travels in nearly the same path as the original photon at super-luminal speed, emitting Cherenkov radiation in the process. The charged particles will likely interact with atmospheric nuclei, generating Bremsstrahlung radiation, producing more gamma rays. Those gamma rays will pair produce and the process repeats itself. The cross sections for pair production and Bremsstrahlung are constant at higher energies, meaning a constant radiation length, about  $37.7 \text{ g cm}^{-2}$  for pair production [49].

The cascade grows exponentially, until it reaches a maximum point on the order of  $10^3$  charged particles for an initial 1 TeV gamma ray [49]. The location of shower maximum

is still far above the earth's surface. The number of particles in the cascade after  $N$  interaction lengths is  $2^N$  with mean energy of  $E_p/2^N$ , where  $E_p$  is the energy of the primary particle. The mean energy for a particle in the cascade will eventually reach a critical energy,  $E_c$ . Below  $E_c$  the interaction cross-section is zero [49]. At this point, the shower maximum has occurred.

After shower maximum has occurred, Compton scattering becomes the dominate process for photon dissipation, while the charged particles lose energy due to Coulomb scattering rather than Bremsstrahlung. The shower has lost the energy to self-propagate [49]. However, Cherenkov radiation is still emitted from the charged particles until they drop below the threshold of 21 MeV, calculated from equation 3.3.

Cosmic Hadrons, mostly protons and helium nuclei but sometimes nuclei of heavier elements, initiate air showers as well. The primary particle will interact with an atmospheric particle, creating a charged or neutral pion. The primary hadron will continue along approximately its original path, although it has lost energy, and may still go through several more nuclear interactions. It might detach several nucleons that will start nuclear interactions of its own, similar to the original hadron. A neutral pion will decay quickly into a pair of gamma rays after a mean lifetime of  $0.83 \times 10^{-16}$  seconds, starting an electromagnetic shower as described previously. Charged pions will decay into muons after a mean lifetime of  $2.6 \times 10^{-8}$  seconds according to the following [14]:



Muons are weakly interacting and emit Cherenkov radiation much lower in the atmosphere and closer to the ground, adding to the background that needs to be accounted for in any subsequent analysis. Muon events are characterized as rings or partial rings, since they only emit at the Cherenkov angle, but closer to the ground. They particularly cause problems for single telescopes; the emission is low enough to only be

seen in the FOV of a single telescope. Therefore, muons are less of a problem for stereoscopic arrays, such as VERITAS, that can discriminate against them by requiring a multi-telescope trigger. Eventually, muons decay into electrons after a mean lifetime of  $\sim 2.2 \times 10^{-6}$  seconds by the following decay processes:

$$\mu^+ \rightarrow e^+ + \bar{\nu}_\mu + \nu_e \quad \text{Eq. 3.6}$$

$$\mu^- \rightarrow e^- + \nu_\mu + \bar{\nu}_e$$

### 3.3. VERITAS Telescope Array

VERITAS is an array of four atmospheric Cherenkov telescopes (ACT) designed to observe Very High-Energy (VHE) gamma rays. The first telescope (T1), which was originally the prototype, saw first light in February of 2005. The stereo system was later introduced by adding a second telescope (T2) in the spring of 2006, later that fall the third telescope (T3) was brought online. The complete array saw first light when T4 was completed in spring 2007. In the summer of 2009 T1 was moved to improve the baseline between the four telescopes, making the array a more optimal diamond shape. A photograph of the array (after the T1 move) is shown in figure 3-2.



Figure 3-2 VERITAS array at the Fred Lawrence Whipple Observatory base camp

The design of each of the VERITAS telescopes is essentially the same as the Whipple 10m telescope that pioneered this technique. Each telescope has a Davies-Cotton design with a 12m diameter segmented reflector sitting on an optical support structure (OSS). Four arms extending from the OSS support the camera at the primary focus of the system. The OSS is a steel space frame, custom designed by M3 engineering (Tucson AZ) and fabricated by Amber steel (Chandler AZ). The OSS sits on a commercial positioner manufactured by RPM-PSI (Northridge CA) [4].

The reflector consists of ~350 mirrors facets with each mirror having an area of  $0.322 \text{ m}^2$ , giving the entire mirror area of  $\sim 110 \text{ m}^2$ . The mirror facets each have a  $24.0 \pm 0.1 \text{ m}$  radius of curvature. The reflectivity of the mirrors is greater than 90% at 320 nm when first placed on the telescope. The mirrors are washed monthly and recoated roughly every four years to keep the light collection efficiency high in the harsh Arizona desert conditions.

The OSS has a tendency to bend slightly due to its own weight and the weight of the camera when pointed at the sky during observing. The mirrors are aligned to correct for this in a procedure known as bias alignment. Bias measurements are taken by attaching lasers pointed onto a screen attached to the camera box. By taking CCD images at 2 degrees and 65 degrees elevation, it can be determined how much each facet moves due to OSS bending. During the actual alignment, a laser illuminates each mirror from 24m away taking advantage of the fact that from twice the focal length the laser light will reflect back onto itself. Then the mirror facets are adjusted so the return beam is offset from the source beam by an amount determined by the CCD measurements. This ensures a better focus and smaller optical point spread function (PSF) at higher elevations (typically  $> 55^\circ$ ) where most observations occur.

Each telescope camera is contained in a square box, 1.8 meters on a side (see figure 3-3). The camera contains 499 photomultiplier tubes (PMTs) each 2.86 cm in diameter with an angular spacing of 0.15 degrees, making a telescope field of view (FOV) of 3.5 degrees [4]. The PMTs are manufactured by Photonis, model #XP2970/02. That model has 10 stages, UV-sensitive, with the high gain and fast timing that is required for ACT experiments [50]. These PMTs have a quantum efficiency (QE) of about 20% at 420nm. A typical curve for QE against wavelength is shown in figure 3-4. Each phototube is connected to a high voltage power supply kept in the electronics trailer for each telescope that can control the high voltage that every PMT receives. Gain varies with high voltage according to a powerlaw, so during operating the voltage of each tube is set so that each one has a gain of  $2 \times 10^5$ . The procedure where this is done is called flat-fielding. This is done to help ensure that each PMT has the same weight in the camera when it comes to triggering on incoming events.



Figure 3-3 The T1 camera box with 499 pixel camera [1].

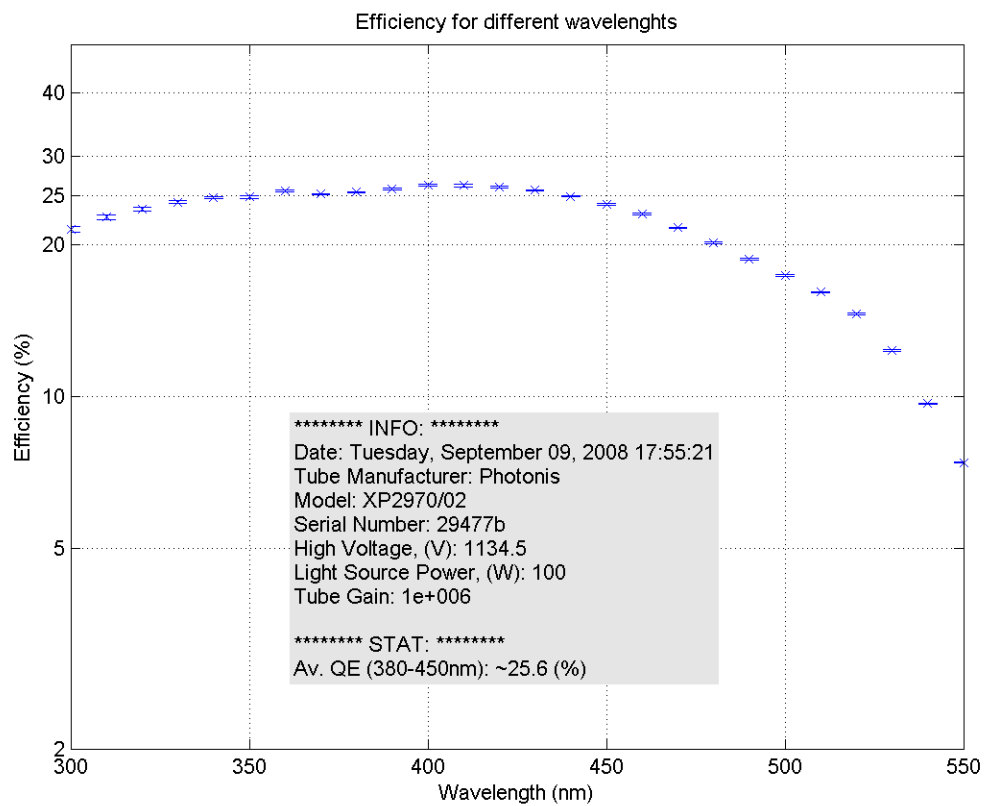


Figure 3-4 Efficiency for an average Photonis PMT plotted as a function of wavelength.



To determine the fluctuations of the night sky background (NSB) and distinguish single muon events from air showers, a three level trigger system is implemented. The trigger helps to reduce the coincidence resolving time and therefore lower the energy threshold [4]. The first level, known as L1, is performed by custom-made constant fraction discriminators (CFDs), one for each PMT pixel. Each PMT signal passes from the camera box to one of four FADC (Flash Analog to Digital Converter) modules in the electronics trailer attached to each telescope which houses the CFDs [51]. The CFDs operate by integrating the voltages of the PMT and produces an output signal if the voltage and a time-delayed copy are over a certain threshold. VERITAS CFDs also include a rate feed-back loop (RFB) that increases the effective threshold when the noise rate rises [51]. The CFD threshold is set to 50mV for normal operations, and 70mV during moonlight operations to cut down on increased NSB levels, while the RFB is set at 60mV/Mhz.

The second trigger is commonly known as the pattern trigger or L2, which determines if a group of adjacent pixels in the camera have satisfied a L1 trigger condition nearly simultaneously. This greatly increases the chance of the incoming event being due to an air shower by decreasing coincidence due to a random noise fluctuation. The L2 modules are also kept in the electronics trailers. The L2 system has two components: an ECL signal splitter, which copies and redirects the signal coming from the CFDs, and a pattern selection trigger (PST). There are 19 PST modules on each telescope that cover overlapping parts of the telescope camera. They are programmed to read CFD trigger information and recognize if the L1 triggers are coming from adjacent pixels in the camera. If the PSTs see that 3 adjacent pixels (or more) pass the L1 trigger within an overlap time of 6ns, then that event passes the L2 trigger [52].

The third trigger is the telescope array trigger, otherwise known as the level three trigger or L3. The L3 trigger determines if incoming L2 signals are consistent with an air shower that is seen by multiple telescopes, which effectively eliminates muon triggers. The L3 electronics are kept in the central VERITAS trailer on site at the base camp. The L3

trigger has a Pulse Delay Module (PDM) that accounts for delays in the arrival times of L2 pulses due to Cherenkov light fronts reaching the telescopes at different times due to geometry of the array and delays due to different lengths of fiber optics between the telescopes and control trailer. The SubArray Trigger board (SAT) takes signals from all telescopes and determines if an incoming event passes the trigger. An event passes if at least a preset number of L2 signals from different telescopes (typically 2) arrive within a user selected coincidence window between 1 and 125 ns (typically 100ns in normal operations) [52].

The signal is split when it arrives from the camera box; one copy is sent to the CFDs and the other is digitized in a set of custom-built 500 MHz FADC units. The FADCs sample the light pulse from the PMT every 2 nanoseconds [53] with a maximum memory depth of 32  $\mu$ s. If an incoming event passes the L3 trigger, a logic signal is sent to the FADC crates and 24 samples corresponding to the event is readout by the VME Data Acquisition as shown in figure 3-5 [51]. Information about the timing and number of the event is also readout by an auxiliary crate. While the FADCs are in readout, the L3 trigger is inhibited by a BUSY signal, resulting in a dead time that scales with the L3 trigger rate. During a typical data run, this dead time is ~10-11% at a typical L3 rate of 225 Hz [52].

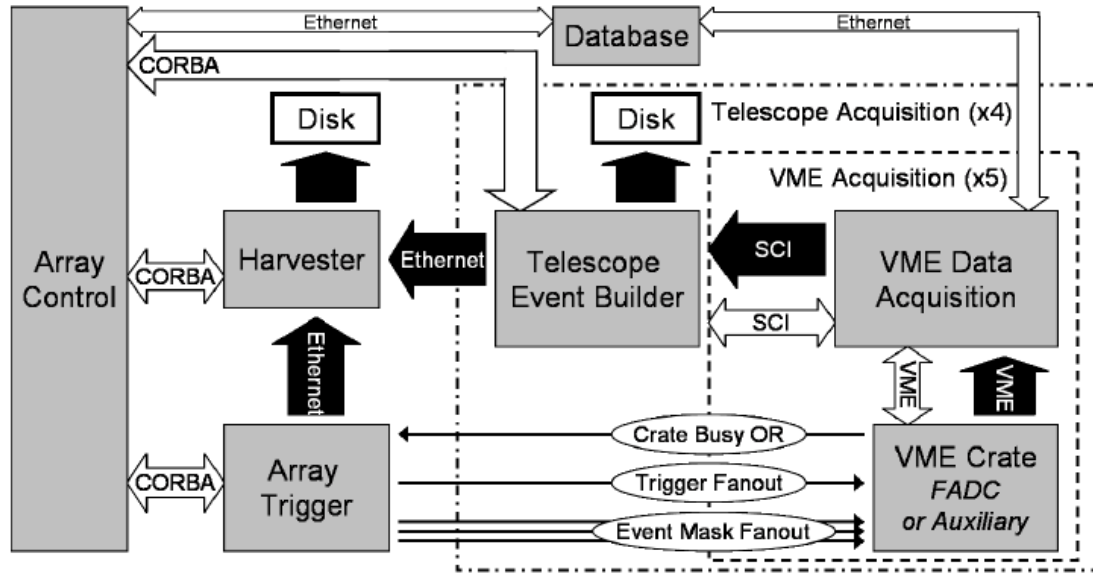


Figure 3-5. Illustration of the VERITAS data acquisition system [51].

Events are then sent to the central VERITAS trailer and go through a few more steps before going to an archive where they can be downloaded and analyzed. A schematic of this data acquisition system is shown in figure 3-5. Buffered events are first sent to an event building computer via a Scaling Coherent Interface (SCI) where they are integrated, tested and passed to the harvester computer [4]. The event building software is written in C++ and controlled by the use of CORBA. The harvester has four main functions: storing data before it gets passed to the archive, combining real time data from each telescope to see what the entire array is doing, diagnostics that serve as a real-time analysis package called Quicklook, and combining data streams when a run is completed into a single file using the VERITAS Bank File (VBF) data format [51]. At the end of the night, the observers run a `send_to_archive` command to transfer data to the main archive at UCLA.

### 3.4. Data Analysis

To get a useful gamma-ray signal from an ACT such as VERITAS, pixel data must be properly calibrated to get accurate charges from each PMT. The charge information is then parameterized to reconstruct geometrical information about the Cherenkov shower, and that information in turn is used to estimate a background and determine if there are sources in the FOV. For the VERITAS Gamma-Ray Analysis Suite (VEGAS) analysis package, the standard analysis package for VERITAS data, this is accomplished with a minimum of four stages and an optional fifth stage.

#### 3.4.1. Calibration Calculation and Application

During every night of observations, a five minute laser run is taken to get relative gain information from each PMT and get timing offsets between pixels. The 10-hz 337 nm laser fires with a 300  $\mu$ J pulse energy and 4ns pulse length. An opal diffuser is used to spread light evenly across the face of the camera [54]. Pedestal events are injected during observations to estimate the expected voltage offset of each FADC trace. Estimates of the electronic noise and NSB are estimated from the pedestal variance [55].

The total charge of a trace is obtained by summing the samples in a particular window size (typically 7 ns) and then subtracting out a pedestal value that represents the total noise current in the phototube. The charge is adjusted for gain by multiplying by the individually determined gain and then dividing by the average of gains of all PMTs. This is done to account for slight differences that might still exist between PMTs.

A cleaning procedure is implemented next. If the integrated charge in a pixel is above 5 times the channel's pedestal variance, then the pixel (now called a picture pixel) is kept in the camera image. Additionally, any pixel adjacent to a picture pixel with an integrated charge greater than 2.5 times the pedestal variance is called a boundary pixel and is also kept in the image. All other pixels and isolated picture pixels with no adjacent picture or boundary pixels have their charges set to zero [55].

### 3.4.2. Shower Reconstruction

The next step is shower reconstruction. Each good image will resemble an ellipse that is the 2-D projection of the Cherenkov air shower onto the camera plane. The 1st, 2nd, and 3rd moments are calculated and are used to parameterize the image, using parameters such as distance (The angular distance between the camera's center to the ellipse's center), size (The sum of the digital counts in the image), length (length of the major ellipse axis) and width (length of the minor axis). By superimposing all the telescope images onto one plane and then finding an intersection point along the major axes of the images the location of the shower in the sky can be found (see figure 3-7). Quality cuts on the distance, size and minimum number of tubes in the image are made to ensure accurate reconstruction. Images with large distance are often truncated by the edge of the camera, causing error in the sky position. Smaller sized images typically have a smaller length/width ratio (and therefore rounder), again causing error in the sky position. If there are only two images in the reconstruction, a cut is also made in the angle of intersection between two major axes. If the intersection angle is too small, then the accuracy of the reconstructed position increases with only one point of intersecting lines.

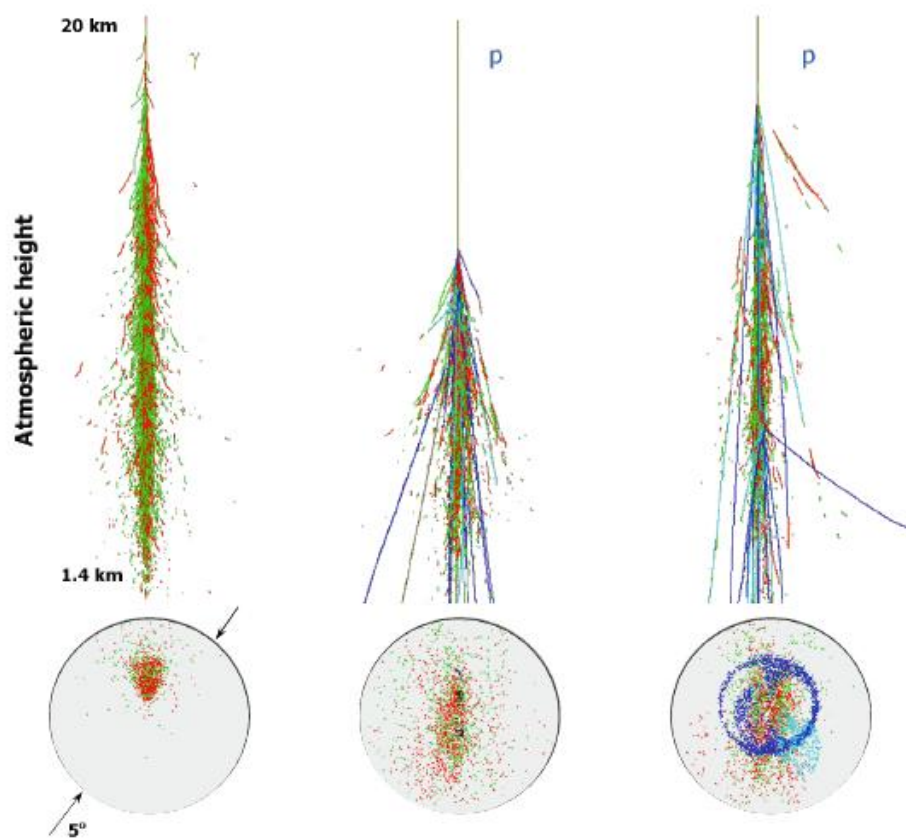


Figure 3-6 Image of a gamma ray shower and its projection onto an ACT camera (left), and the same for a hadronic shower (center) and a hadronic shower with a muon “ring” (right). Image courtesy of G. Sembroski.

As previously mentioned, T1 was moved in the summer of 2009 to increase sensitivity, since it was less than an optimal distance away from T4. Events that triggered L3 on both T1 and T4 (referred to as T1T4 pairs) but no other telescopes were being reconstructed with less accuracy, leading to extra background in the analysis and reducing sensitivity. Removing T1T4 pairs before the T1 move is done as an extra quality cut. This cut is not performed on data taken after the T1 move.

At this point in the analysis, Cherenkov showers have been separated from the NSB and electronics noise, but gamma ray showers still have to be separated from showers

initiated by protons and other types of cosmic rays. To accomplish this, cuts are performed on two parameters called Mean Scaled Length (MSL) and Mean Scaled Width (MSW). Both take advantage of the fact that proton and other cosmic ray showers are on average larger than gamma ray showers. See figure 3-6 for an example of the contrast between gamma ray initiated showers and showers initiated by protons. These parameters are calculated as follows:

$$MSL = \frac{1}{N_{tel}} \sum_i^{N_{tel}} \frac{l_i}{l_{sim}(z, size, r)} \quad \text{Eq. 3.7}$$

where  $N_{tel}$  is the number of telescopes in the image,  $l_i$  is the length of the image,  $l_{sim}$  is the average of simulated gamma ray showers at a given zenith angle,  $z$ , size and impact distance,  $r$ , taken from a table of simulated events. Impact distance is the projected location of the shower center on the ground [55]. The example in equation 3.7 is for MSL, but MSW is calculated in a similar way. By cutting out events with large MSL or MSW, the gamma ray sensitivity can be improved greatly. A cut on the lower height of shower maximum (HSM) reduces hadronic events, since gamma events tend to interact higher in the atmosphere (see figure 3-6).

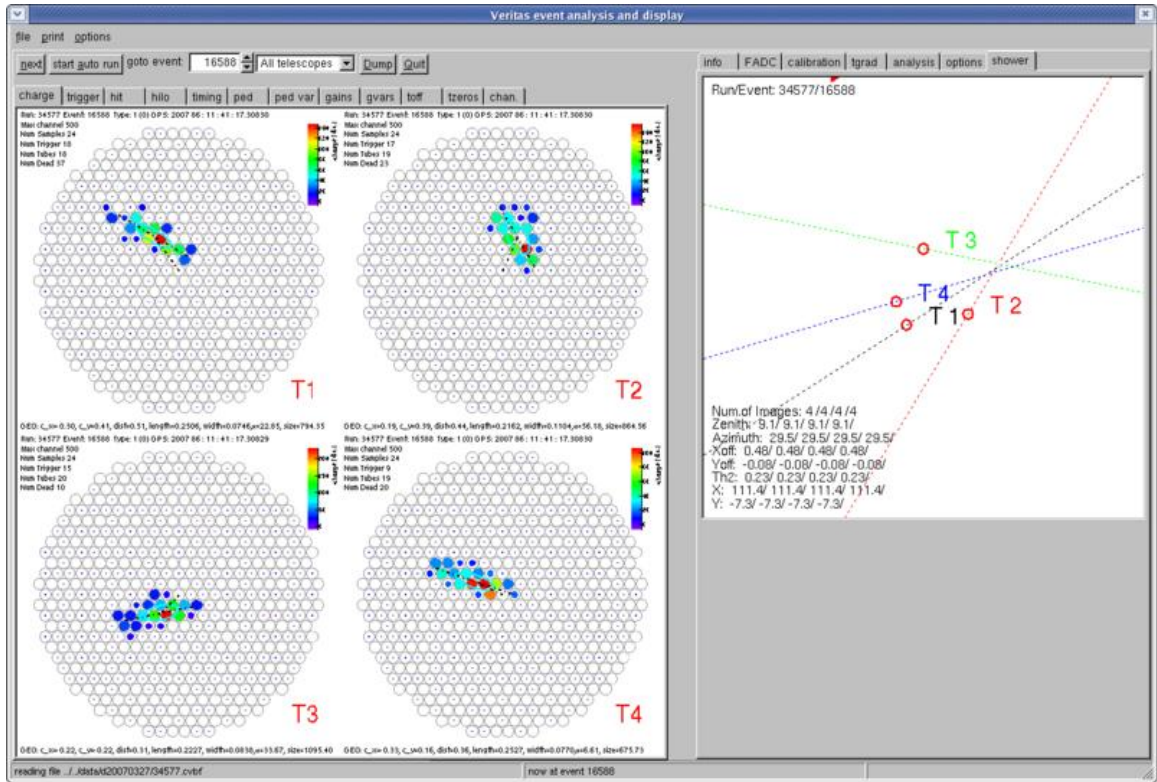


Figure 3-7 Images of a Cherenkov shower in the four telescopes (four left images) and its reconstructed position on the ground (right).

### 3.4.3. Gamma-Ray Signal Extraction

Finally, a gamma-ray signal can be extracted after these cuts are made. A 2D histogram called a sky map is produced using the reconstructed sky events. Right Ascension and Declination coordinates are found using the timing and telescope pointing information in a process called de-rotation. Excess gamma ray events above the background are found by applying the following test:

$$N_{ex} = N_{on} - \alpha N_{off} \quad \text{Eq. 3.8}$$

Where  $N_{ex}$  represents the excess of gamma rays that could indicate a signal,  $N_{on}$  is defined as the number of counts in an ON region and  $N_{off}$  is the number of counts in the OFF



region(s) [56]. The ON region is defined as a circular area of the sky map that is the region of interest. For any given run, it is typically 0.5 degrees offset from the camera center. The direction of the offset is often referred to as the wobble direction. The size of the ON region, called the theta-squared cut (theta is defined as the angular distance from the center of the array pointing). Theta-squared is often enlarged for extended sources. There are two major ways of defining the OFF regions; each with a different way of defining the alpha in equation 3.8. The first is the reflected ring model, where a series of OFF regions, each the same size as an ON region is located at a reflected position from the camera center [55].  $\alpha$  in this case is the inverse of the number of OFF regions, so that the background can be weighted properly to represent the background gamma rays in the ON region. The other way to define the OFF region is the ring background model. It uses an annulus centered on the ON region for the OFF region. The ring covers different offsets and camera acceptance decreases as offset increases. Alpha therefore is calculated by the ratio of the integral of the acceptance function in the ON region to the ratio of the integral of the acceptance function in the OFF region [57].

To determine if the gamma ray excess is a detected signal, the significance needs to be calculated. It is defined as the confidence level in Gaussian sigma. If we assume a Poisson (low statistics) background, the significance is:

$$S = \frac{N_{on} - \alpha N_{off}}{\sqrt{N_{on} + \alpha^2 N_{off}}} \quad \text{Eq. 3.9}$$

Equation 3.9 is actually just the excess signal shown in equation 3.8 divided by the estimate of the standard deviation of the signal using Poisson statistics [56].

An alternative way of calculating significance uses a maximum likelihood method. That method takes the ratio of the probability of the ON region not containing a signal to the probability of it containing a signal, in other words, the probability of  $N_s$  being null as opposed to any other value. The quantity  $-2\ln(\lambda)$ , where  $\lambda$  is the ratio of probabilities will

approximately follow a  $\chi^2$  distribution with one degree of freedom. The degrees of freedom are  $N_s$ , since it is the quantity being tested. The  $\chi$  is equivalent to a Gaussian sigma, which in turn is equivalent to significance:

$$S = \sqrt{2} \left( N_{on} \ln \left( \frac{1 + \alpha}{\alpha} \left( \frac{N_{on}}{N_{on} + N_{off}} \right) \right) + N_{off} \ln \left( (1 + \alpha) \frac{N_{off}}{N_{off} + N_{on}} \right) \right)^{1/2} \quad \text{Eq. 3.10}$$

Equation 3.10 is a better calculation if both  $N_{on}$  and  $N_{off}$  are both not small [56]. A significance of five or greater is required for a VERITAS detection, giving a probability of  $5.733 \times 10^{-7}$  of the excess  $\chi$  signal not being a background statistical fluctuation. An example of a completed VERITAS sky map is shown in figure 3-8.

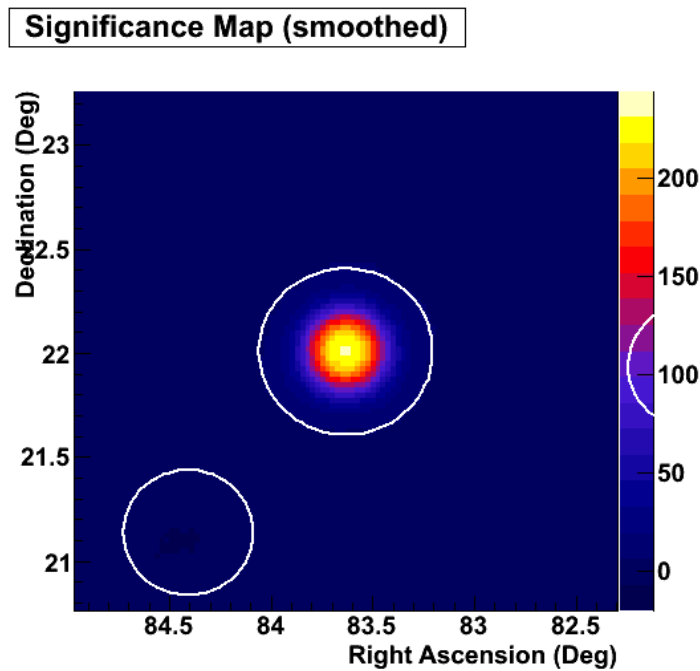


Figure 3-8. A significance sky map of the Crab Nebula, the standard candle of TeV astronomy. The white circles indicate regions excluded for use as background.

### 3.4.4. Other Data Products

Two other images, along with 2-D sky map images, can be useful in understanding sources in gamma-ray astronomy. These are spectra and light curves. Both of these require calculation of the effective area of the Cherenkov shower to get a flux. Effective area can also be thought of as a cross section for a probability of a particular shower to fall along the ground based on the orientation of the original gamma ray in the sky.

Effective areas are calculated by using lookup tables similar to the ones used for event reconstruction using simulations. A typical plot of effective area as a function of energy is shown in figure 3-9. Since Cherenkov showers are emitted at one angle with respect to the particle that created the wave front (equation 3.1), the showers land in an elliptical area along the ground. Simulated showers have their impact distance (distance along the ground from the shower's center to the array's center) calculated, along with reconstructed energy. The ground is divided up into a grid and the probability of a particular shower triggering the array if the array was centered on that particular part of the grid. That probability is multiplied by the area of the grid section and added to the effective area curve for that energy.

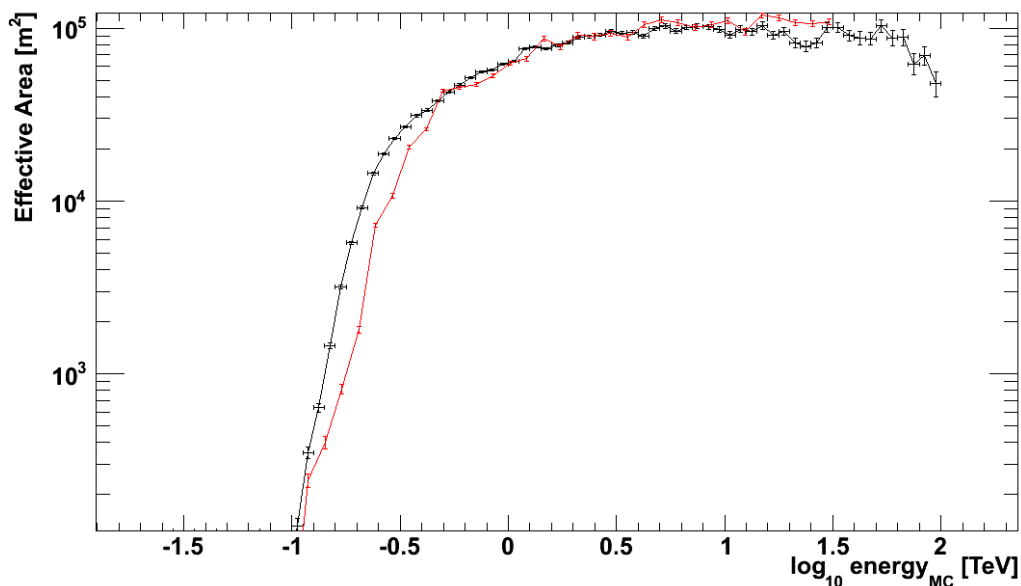


Figure 3-9. Effective area plots for two different simulation packages. KASCADE simulations are in red, CORSIKA are in black.

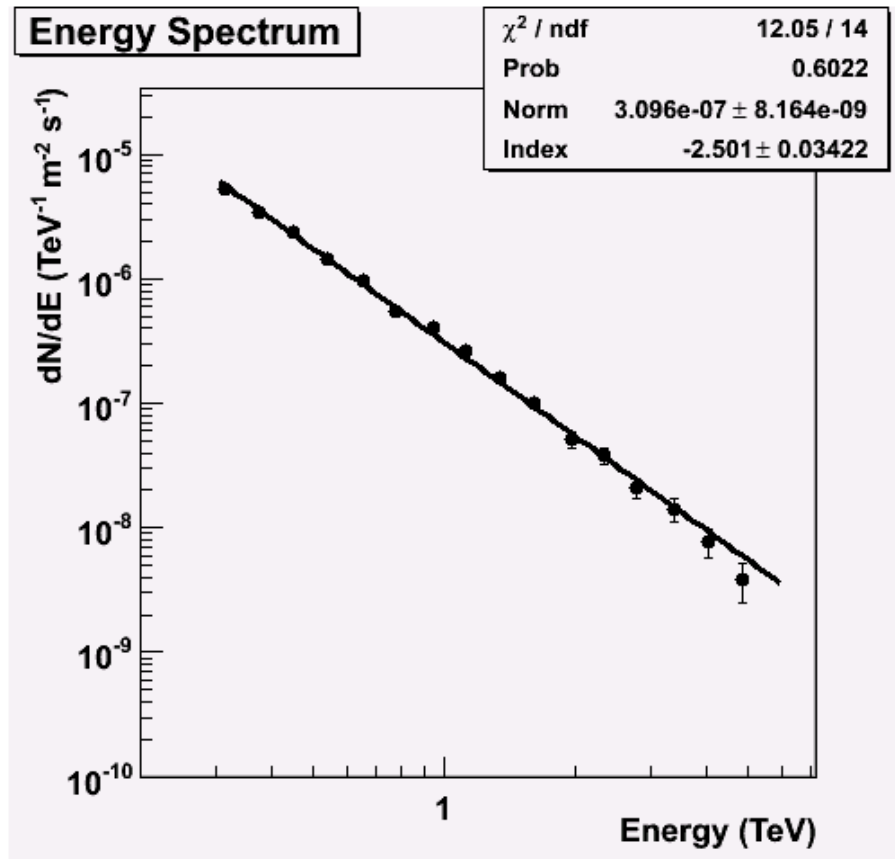


Figure 3-10. Energy Spectrum of the Crab Nebula using VERITAS data from the 2008-2009 observing season.

Effective area curves are created for a range of zenith and azimuth angles, telescope offsets and noise levels. The effective area used on the data is an interpolation based on the conditions on the data just mentioned. Flux is calculated in each bin based on the following:

$$R_i = \int_{E_i - \frac{\Delta}{2}}^{E_i + \frac{\Delta}{2}} A(E)F(E)dE \quad \text{Eq. 3.11}$$

Where  $F(E)$  is flux,  $A(E)$  is effective area as a function of energy (curve in figure 3-9), and  $R_i$  is the rate of the  $i^{th}$  bin centered at an energy  $E_i$ . If the resulting flux is plotted as a function of the photon arrival time, it's called a light curve, if it's plotted as a function of the reconstructed energy, (see figure 3-10) then the plot is a spectra.

## CHAPTER 4. PWN SELECTION CRITERIA

The central question of this work: “Which PWNs and the Pulsars associated with them are VHE emitters and which are not?” could depend on any number of parameters that are tied to their emission. Looking for correlations in existing VHE data can give insight into which of those parameters are linked to their emission. PWN with similar qualities to the already confirmed VHE sources would be ideal targets for observation. Since VERITAS is located in the northern hemisphere, the additional requirement that the objects also be located in the northern hemisphere is added as well.

### 4.1. VHE PWN Population Study

The PWN to be considered in our study of existing VHE emitters are above  $5\sigma$  significance by the 3<sup>rd</sup> generation of VHE observatories: HESS, MAGIC or VERITAS. Additionally, the VHE emission should be coincident with the position of the pulsar. Searching TeVCat [1] leaves thirteen PWN in the population study which is briefly summarized in table 4.1. Only PWN which have been clearly identified as PWN are used, therefore HESS unidentified sources with high  $\dot{E}$  pulsars nearby do not qualify for study in this work.

Table 4.1. PWN which are VHE emitters as of Spring 2010.

Source	Pulsar	$F_{\text{VHE}}$ (CU)	D (kpc)	$\dot{E}$ (ergs/s)	$\tau_c$ (kyr)	Ref.
Crab	J0534+2200	1.0	2.00	4.61E+38	1.2	[1]
Vela	J0835-4510	0.75	0.29	6.92E+36	11.3	[59]
HESS J1356	J1357-6429	0.11	4.09	3.10E+36	7.3	[60]
Kookabura P.	J1420-6048	0.07	7.69	1.04E+37	13.0	[61]
MSH15-22	J1637-4642	0.15	5.77	6.40E+35	41.0	[62]
HESS J1616	J1617-5055	0.19	6.46	1.60E+37	8.1	[64]
HESS J1708	J1709-4429	0.17	1.82	3.41E+36	17.5	[64]
HESS J1718	J1730-3350	0.02	4.25	1.25E+36	89.6	[63]
HESS J1809	J1809-1917	0.14	3.71	1.78E+36	51.4	[63]
HESS J1825	J1826-1334	0.17	4.12	2.87E+36	64.1	[64]
G54.1+0.3	J1930+1852	0.03	5.00	1.20E+37	2.9	[66]
Boomerang	J2229+6114	0.05	8.00	2.25E+37	10.4	[65]
HESS J1912	J1913+1011	0.04	4.48	2.90E+36	168.8	[60]

#### 4.2. Results of the Population study:

The population study shows that the PWN most likely to be VHE emitters are young and energetic. This can best be illustrated by figure 4-1, known as the  $P - \dot{P}$  diagram. This plots over 300 pulsars from the ATNF catalog [67], including the thirteen pulsars listed in table 4-1. Along with the pulsars on this diagram, contour lines for the pulsars spin-down luminosity (equation 2.9) and characteristic age (equation 2.13) are drawn. The plot shows that the majority of VHE pulsars have  $\dot{E} > 10^{36}$  ergs/s and  $\tau_c < 100$  kyr.

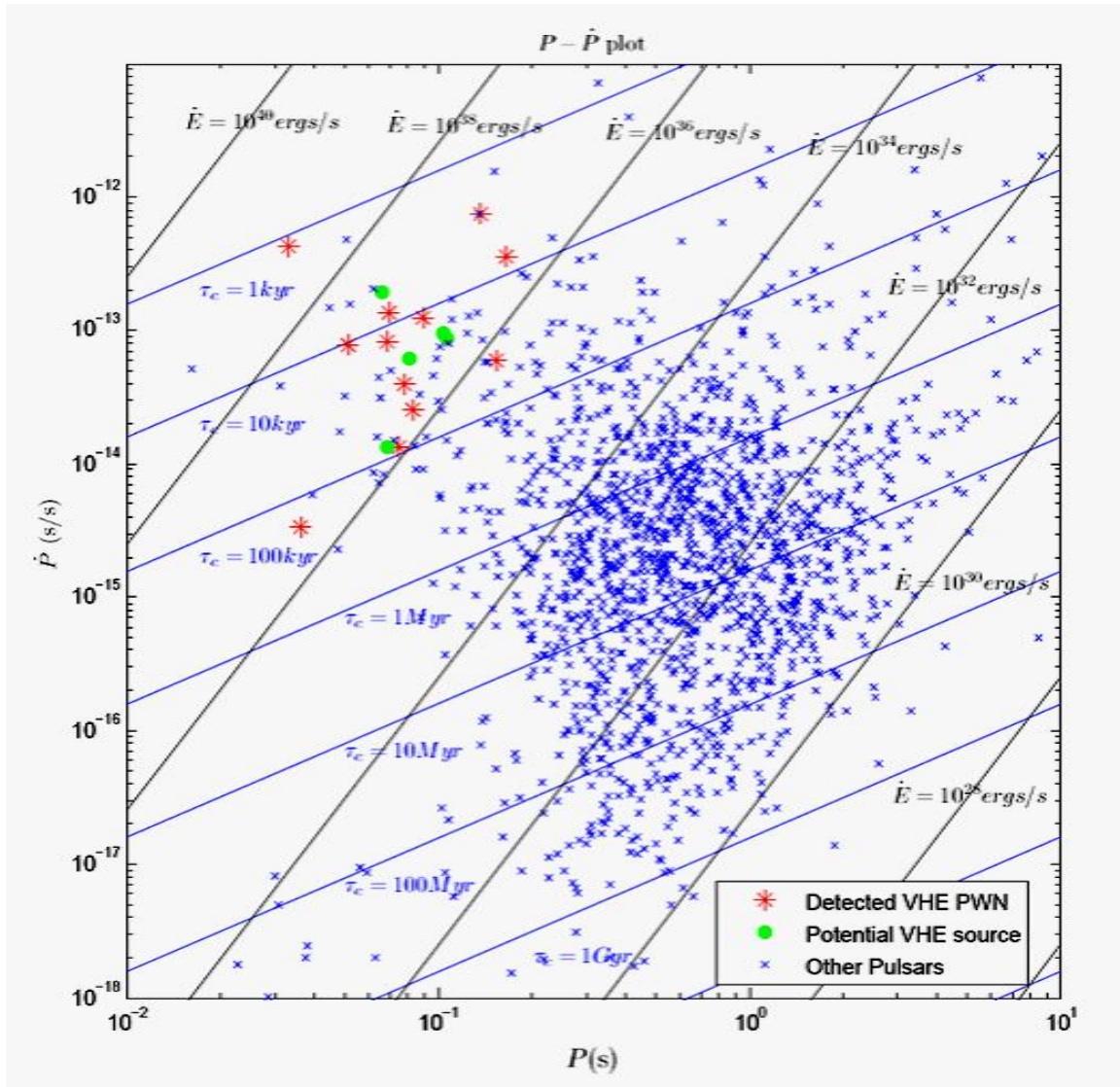


Figure 4-1. Period vs. Period derivative plot. Blue contour lines are characteristic ages for the pulsar, and black contour lines are spin-down luminosity. Red asterisks indicate already established VHE PWN from table 4-1, green circles are potential sources discussed in this section, and other pulsars are blue crosses.

The evidence that luminosity of the PWN at TeV energies ( $L_{TeV}$ ) depends on  $\dot{E}$  is shown in figure 4-2, which plots the two quantities. Contour lines of TeV efficiency ( $\varepsilon = L_{TeV}/\dot{E}$ ) is also drawn on the plot. The color of the point on the plot indicates the age of the pulsar. Crab-like pulsars (less than 5kyrs old) are shown in red, Vela-like pulsars



(5kyrs to 50kyrs old) are green. Pulsars older than 50 kyrs are shown in blue. TeV Luminosities are calculated by integrating the spectral function of the pulsar in the energy range from 1 to 10 TeV, then multiplying by a factor of  $4\pi d^2$ , where  $d$  is the distance to the pulsar.

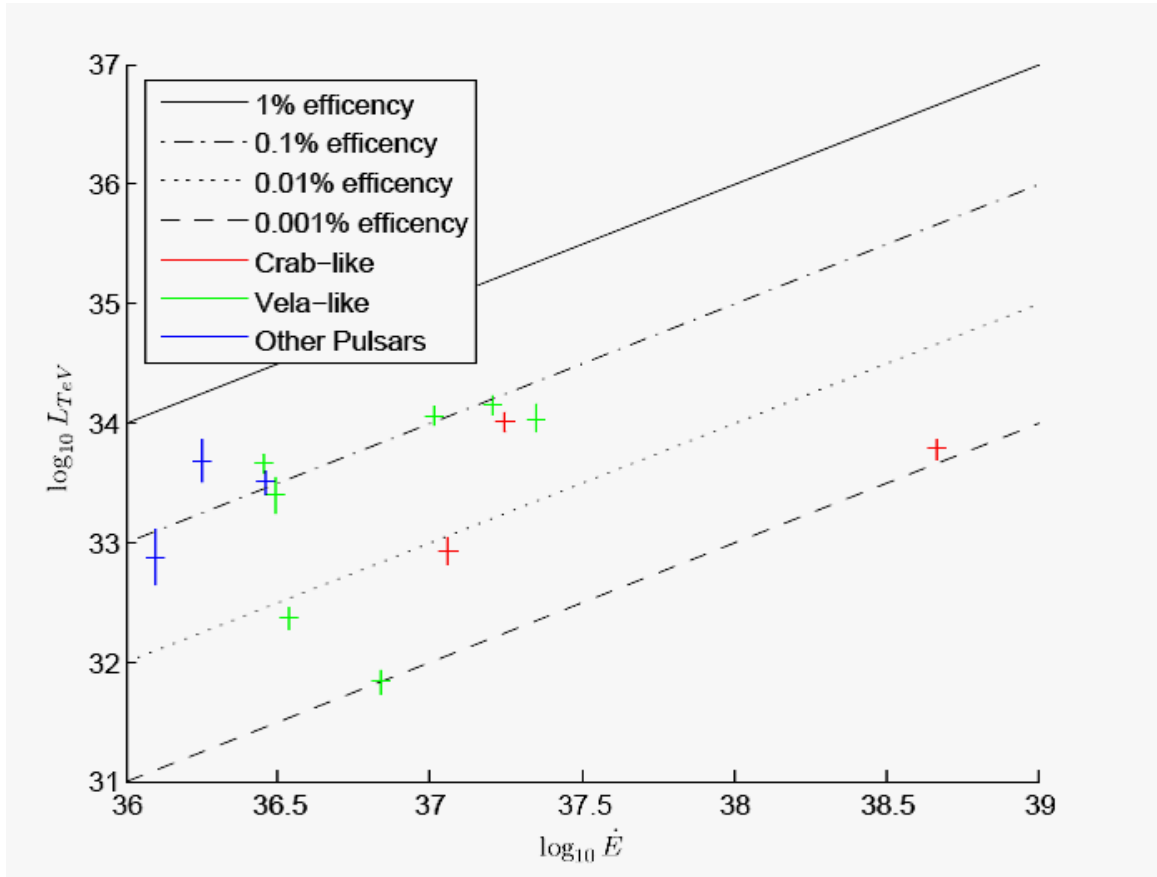


Figure 4-2. Plot of TeV Luminosity as a function of spin-down power. Contour lines of TeV efficiency are also drawn.

A fit of the TeV luminosity with the pulsar quantities was performed to determine how the TeV luminosity depends on the period and period derivative. It is assumed that  $L_{TeV}$  (in ergs/s) is a function of  $P$  (in seconds),  $\dot{P}$  (divided by  $1 \times 10^{-15}$ ) with no other dependencies:

$$\log_{10} L_{TeV,Calc} = a \log_{10} P_{[s]} + b \log_{10} \dot{P}_{-15} + c \quad \text{Eq. 4.1}$$

Where  $a, b$ , and  $c$  are the free fit parameters. The fit yielded  $a = -1.4 \pm 0.9$ ,  $b = 0.34 \pm 0.29$ , and  $c = 27.1 \pm 1.7$ , when fitted with the thirteen PWNs in table 1.

A second fit is performed with  $L_{TeV}$  as a function of only  $\dot{E}$  (in units of ergs/s):

$$\log_{10} L'_{[TeV]} = a' \log_{10} \dot{E}_{\left[\frac{erg}{s}\right]} + c' \quad \text{Eq. 4.2}$$

The fit yields  $c' = 19.2 \pm 11.5$  and  $a' = 0.38 \pm 0.31$  as the best fit parameters for equation 4.2.

Both fits suggest that  $L_{TeV} \sim \dot{E}^{1/2}$  or  $L_{TeV} \sim B_0/P^2$  which has the same  $P$  and  $\dot{P}$  dependence. To determine how well correlated those parameters are the correlation coefficient was calculated for the two parameters:

$$r = \sum_i^n \frac{(L_{TeV,i} - \bar{L}_{TeV})(\dot{E}_i^{1/2} - \bar{\dot{E}}^{1/2})}{\sigma(L_{TeV})\sigma(\dot{E}^{1/2})} \quad \text{Eq. 4.3}$$

Where  $\sigma$  is the standard deviation. The  $r$  value calculated from equation 4.3 is 0.356, indicating a positive correlation, although not a strong one. The correlation can also be seen in figure 4.3.

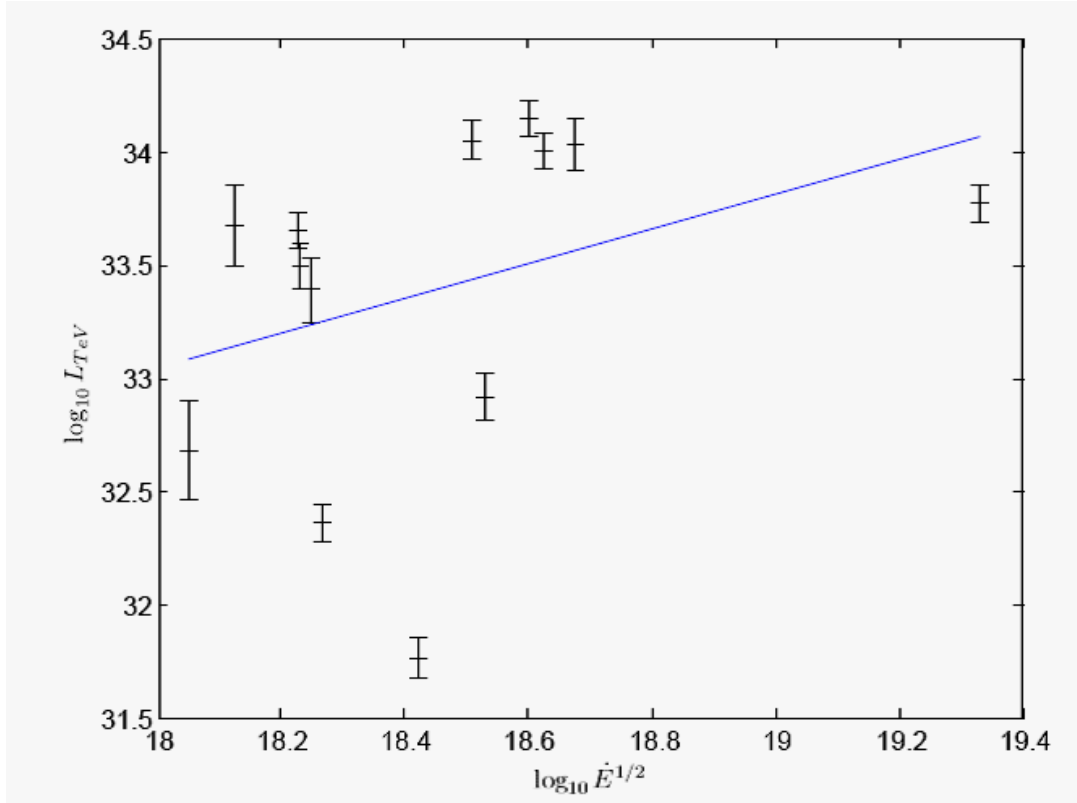


Figure 4-3. TeV Luminosity as a function of the square root of spin-down luminosity. The best fit value of equation 4.2 is shown as the blue line.

#### 4.3. Candidates for VHE Observation

By searching the ATNF database [67], four pulsars were found with  $\dot{E} > 10^{36}$  ergs/s,  $\tau_c < 100$  kyrs and declination above zero degrees, that were not already VERITAS sources: the PWN 3C58, associated with the pulsar J0205+6449, J2021+3651 in the Cisne galactic region, J1856+0245, which is a recently discovered pulsar associated with the unidentified source HESS J1857+026, and PSR J1928+1746 associated with an Egret source and roughly 1 degree from the PWN G54.1+0.3. Their position on the  $P - \dot{P}$  diagram is marked with green circles on figure 4-1. VERITAS data was taken on all four of these potential sources in the period from fall 2007 to summer 2010. The results of the observations of these four sources are given in the following chapter. The next chapter also gives results of the observations for the three already established VERITAS PWN sources: Crab, G54.1+0.3 and the Boomerang PWN.

#### 4.3.1. Crab Nebula

The Crab Nebula is possibly the most studied object by astronomers outside of the solar system. The supernova associated with it was observed in the constellation Taurus by the Chinese and Arabs in 1054 AD. The nebula was discovered much later in 1731 by John Bevis. The pulsar was discovered after that, in 1968 [68], prompted by the discovery of the first pulsar by Bell and Hewish [69]. It is one of about half a dozen optical pulsars that can be seen [70].

The Crab Nebula is the strongest VHE gamma-ray source in the sky. That, along with very little flux variation makes Crab the standard candle for VHE astronomy. Flux from VHE sources are often quoted in Crab units, such as the flux column in table 4-1. Cuts used for reconstruction quality and Gamma/Hadron separation are typically optimized based on the Crab nebula signal.

#### 4.3.2. PSR J1928+1746/PSR J1930+1852

PSR J1930+1852 is one of the most energetic ( $\dot{E} = 1.2 \times 10^{37}$  ergs/s) and youngest ( $\tau_c = 2900$  yrs) known [71], making it a ‘cousin’ to the Crab. The PWN associated with it, G54.1+0.3 was identified as such by high resolution radio observations [72]. X-ray observations revealed an X-ray jet, consistent with the radio extension [73]. The X-ray to TeV gamma-ray luminosity ratio is higher for G54.1+0.3 than for any other young rotation-powered PWN, 0.7, which is higher than Crab by two orders of magnitude [66]. Leptonic models and Leptonic-Hadronic hybrid models have been proposed to explain this [74]. Neither the PWN nor the pulsar has yet been seen by FERMI.

About 1.4 degrees away from PSR J1930+1852 is the unidentified Egret source 3EG J1928+1733. This is outside of the 99% confidence-level error box. The older and less energetic pulsar PSR J1928+1746 has been proposed to be a more likely counterpart for the Egret source [75]. PSR J1928+1746 is 1.2 degrees away from PSR J1930+1852, coincident with the Egret source and the Fermi source 1FGL 1929.0+1741c [66]. PSR

J1928+1746 has a flat radio spectrum and a derived distance of about 6 kpc from dispersion measure [75].

#### 4.3.3. PSR J2229+6114/Boomerang

The PWN associated with PSR J2229+6114, G106.65+2.96, is also known as the ‘Boomerang’ PWN for its arc shape at X-ray and radio frequencies. The pulsar PSR J2229+6114 was discovered when looking for a counterpart for the Erget source 3EG J2227+6122 [76]. The pulsar was later associated with the supernovae remnant G106.3+2.7. Despite being one of the most energetic pulsars known, it has low radio luminosity [77]. Pincault & Joncas confirmed the object as a SNR [78]. The pulsar was seen at GeV energies by FERMI [79]. MILAGRO also reported a significant excess in the FOV [80].

#### 4.3.4. PSR J1856+0245/HESS J1857+026

The Vela-like pulsar PSR J1856+0245 is a recent discovery by the Arecibo PALFA survey, looking for counterparts to the TeV unidentified source HESS J1857+026 in other wavelengths. The existence of a young energetic pulsar within the HESS source makes a strong argument that the source is a PWN [23]. The pulsar is also spatially coincident with the faint X-ray source AX J185651+0245, adding additional evidence that the HESS source is a PWN, since many TeV sources with young pulsars also contain X-ray synchrotron sources [81]. The inferred distance is 9 kpc from the dispersion measure [23], making the gamma efficiency  $\varepsilon_\gamma = 3.1\%$ , higher than other TeV PWN, as seen in figure 4-2.

A second HESS unidentified source, HESS J1858+020 is about 0.7 degrees from HESS J1857+026. It is possible that this source is an extension of HESS J1857+026, but no significant emission has been seen linking the two. It has also been suggested that the pulsar PSR J1857+0143 could explain the source, but it is significantly offset [81].

#### 4.3.5. PSR J2021+3651/Cisne PWN

PSR J2021+3651 was discovered during a targeted search for radio pulsations from the ASCA X-ray source AX J2021.1+3651. AX J2021.1+3651 was proposed as counterpart for the EGRET source GeV J2020+3658 [82]. Chandra X-ray observations later revealed the PWN, named G75.2+0.1 [83]. The pulsar was also among the first FERMI sources. The lightcurve folded over period shows two pulses, separated by 0.468 pulse phase, both of equal amplitude. The first pulse lags the maximum of the 2 GHz radio pulse by 0.162 phase. Analysis of the Chandra data shows that the pulsar is detected at  $4.5\sigma$ , with the same shape as the gamma-ray curve, shifted  $\sim 0.1$  phase with the first peak [84].

#### 4.3.6. 3C58

The radio source 3C58 was first identified as a SNR [85], and then later as a PWN [86]. Later, the pulsar PSR J0205+6449 was discovered within the PWN by Chandra data and archival Rossi X-ray Timing Explorer (RXTE) data [87]. Weak, narrow radio pulsations were found soon after that [88].

3C58 has the third highest spin-down luminosity of all galactic pulsars, and fairly young (5.4 kyrs), qualifying it for study in this work. Combined with a distance of 3.2 kpc from neutral hydrogen absorption [89], it makes it a promising VHE candidate. The pulsar is a Fermi source with both a pulse and inter-pulse separated by  $\sim 0.49$  phase [90].

### 4.4. Conclusions of the Population Study

The population study has two purposes as far as the larger scope of this work is concerned: It determines which PWN are good candidates that are likely to be VHE emitters. The observations of these PWN, along with other objects that fit the same criteria with VERITAS will be discussed in the following chapter. The selection criteria determined from the population study will also tell us something about the nature of these sources. The implications of the selection criteria will be discussed in the concluding chapter.

## CHAPTER 5. PWN OBSERVATIONS

### 5.1. Crab Nebula and Pulsar

#### 5.1.1. Cuts and Data Set Used for Analysis

The Crab Nebula is by far the strongest known source in the VHE sky. Most VHE sources are 15% of the Crab flux or less. Cuts used for reconstruction and gamma/hadron separation are optimized using a set of quality Crab data that is ‘scaled down’ to an appropriate fraction of the Crab flux. Optimizing to the full Crab flux level often allows extra events that are more likely to be hadrons. This concept is better illustrated in figure 5-1, which shows that for point sources, a smaller  $\theta^2$  is more optimal. An optimal cut is found when the significance is maximized for the scaled down excess (equation 3.9, but using  $N'_{on} = sN_{ex} + \alpha N_{off}$  instead of  $N_{on}$ , where  $s$  is the fraction of the Crab flux for the desired cuts).

In addition to the predicted flux, sets of cuts may be altered due to the believed spectral index and extension of potential sources. Sets of cuts may be ‘hard’, ‘medium’ or ‘soft’ cuts based on the spectral index of the source. Hard cuts are used on those sources with spectral indices greater than the Crab index (-2.5), while soft cuts are those for an index of less than the Crab’s. Medium cuts are used for sources that are around the Crab’s spectral index. The only cut that changes for source extension is  $\theta^2$ . Since the Crab is a point source in VHE, the scaled optimized  $\theta^2$  cut is acceptable for point sources. Extended sources in VHE such as the Boomerang PWN (see section 5.3.2) require larger values of  $\theta^2$  to encompass more  $\gamma$ -like events in the same ON region. Finally, the move of T1 during the summer of 2009 has also changed the MSL and MSW cuts due to

simulations reflecting the new T1 position, so cuts used after the 2008-2009 observing season will be slightly different.

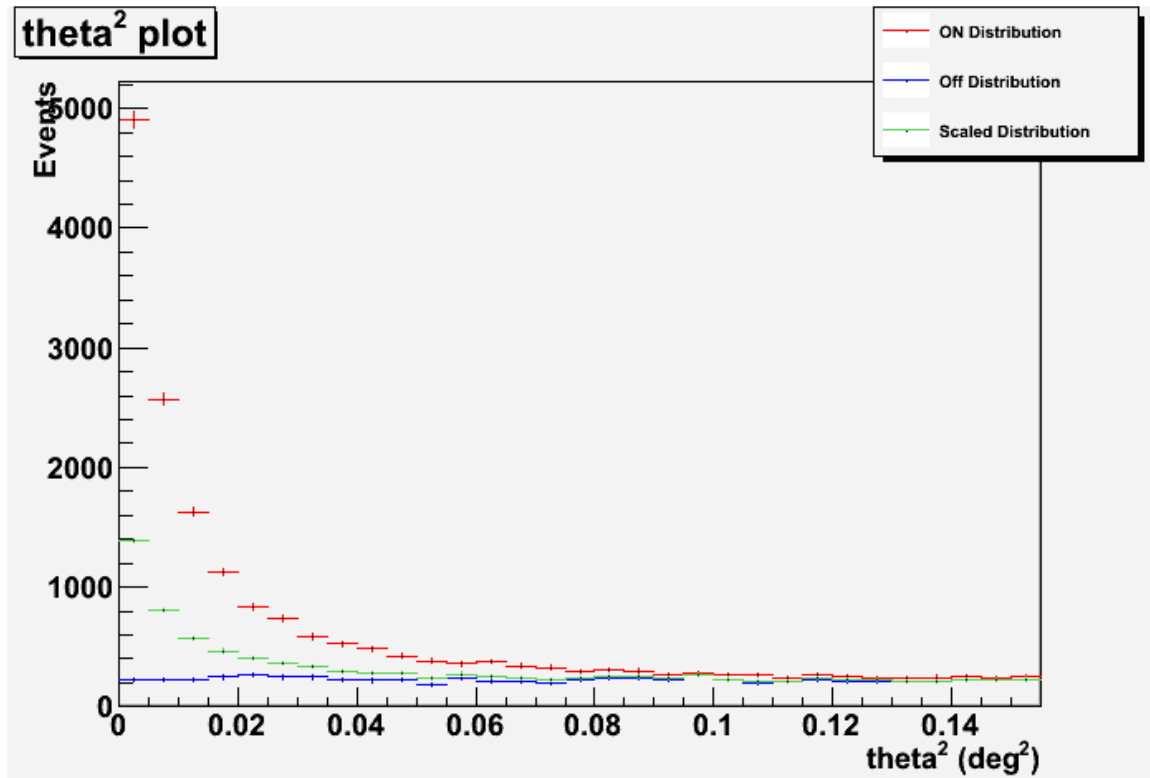


Figure 5-1.  $\theta^2$  distribution of the Crab Nebula in red, the Crab OFF regions in blue, and the Crab scaled down to 25% of the total excess in Green.

All analysis in this work has cuts that do not change depending on source. They are always implied to be present in this work. The maximum distance is  $1.43^\circ$ , minimum of five pixels in a single telescope image after cleaning, and lower cuts of 0.05 on both MSL and MSW.

The Crab Nebula, as previously mentioned, is a point-like strong source. Table 5-1 summarizes cuts optimized for the Crab. The runs used in this work are the same as used for finding the Crab Pulsar, summarized in the next section.



Table 5.1. Cuts used for Crab Nebula analysis

Cut	OVA	NVA
SIZE [dc]	400	400
Pairs to deny	T1T4	None
MSL Upper	1.35	1.47
MSW Upper	1.17	1.18
HSM Lower [km]	5.0	5.5
$\theta^2$ [deg <sup>2</sup> ]	0.025	0.025

The data taken for the Crab Nebula was taken over three different observing seasons of VERITAS full array operations: fall 2007 to summer 2008, fall 2008 to summer 2009 and fall 2009 to summer 2010. This amounts to 25 hours of quality data before the T1 move and 14 hours afterwards. In this work, data taken with the array before the T1 move will be referred to as old VERITAS array data (or OVA data) and after the T1 move will be referred to as new VERITAS array data (or NVA data).

#### 5.1.2. Results of Observations of the PWN

The resulting sky maps from the observations of the Crab Nebula are shown in figure 5-2. They show a bright, point source centered on the location of the nebula. At the point of maximum significance, there are 22,778 excess counts above the background, detecting the Crab Nebula at a level of  $227\sigma$  using equation 3.10 to calculate significance.

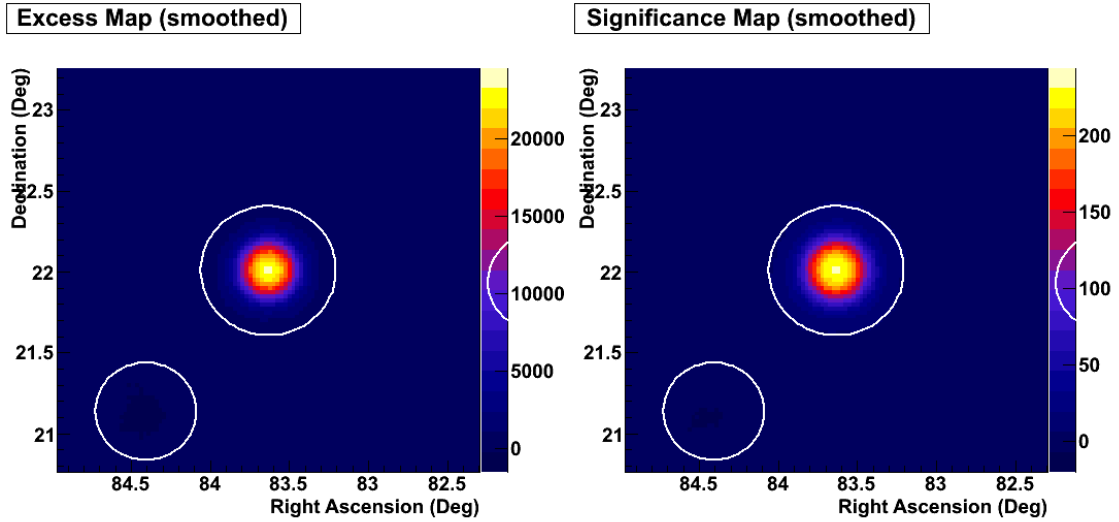


Figure 5-2. Excess (left) and Significance (right) maps of the Crab PWN. White circles indicate background exclusion regions in the analysis.

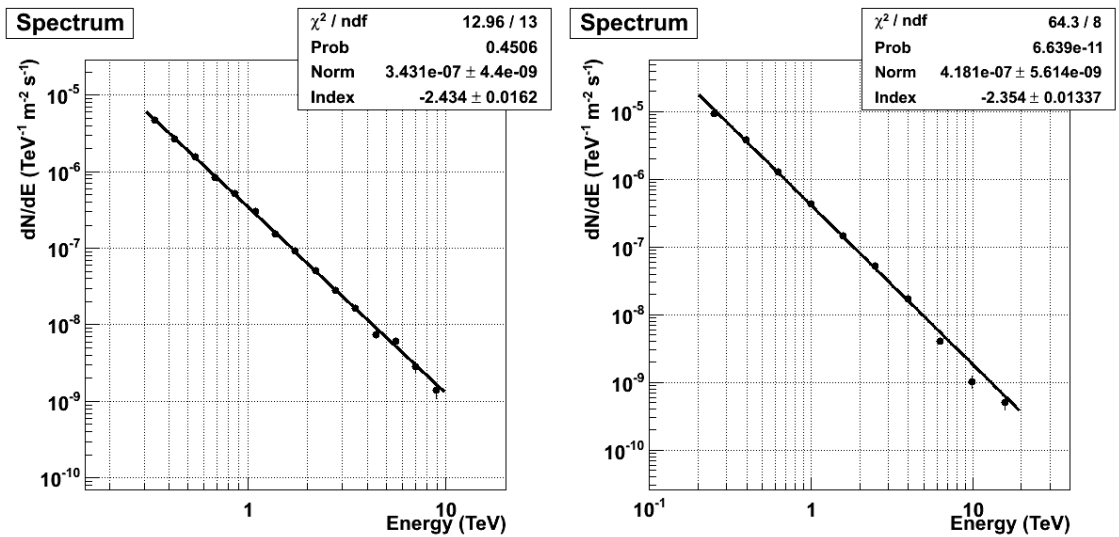


Figure 5-3. Spectrum of the Crab Nebula before (left) and after (right) the T1 move

The spectrum for the Crab nebula is shown in figure 5-3. The flux is fit with a powerlaw function:

$$F(E) = kE_{[TeV]}^{-\Gamma} \quad \text{Eq. 5.1}$$

where  $k$  is the normalization,  $\Gamma$  is the photon index, and  $E_{[TeV]}$  is the energy in units of TeV. Differences in the two spectra from before and after the T1 move are due to systematic errors that are not yet understood at this time. The flux of the Crab Nebula is 15% higher than the canonical previously published values [58, 91 HESS spectrum].

### 5.1.3. Pulsar Analysis

The pulsar within the PWN is detected if strong pulsations are seen from the light curve folded on the period of the pulsar. Time of arrival (TOA) has to be corrected for motions of the earth through the solar system, a process called barycentering. The barycentered photon arrival times are folded into phase by the following equation:

$$\varphi(t) = (t - t_0)\nu + \frac{1}{2}(t - t_0)^2\dot{\nu} + \frac{1}{3}(t - t_0)^3\ddot{\nu} \quad \text{Eq. 5.2}$$

Where  $\varphi$  is the phase (mod 1),  $\nu$  is the frequency of the pulsar observed at a time  $t_0$ , and  $\dot{\nu}$  and  $\ddot{\nu}$  are the first and second time derivatives of the frequency, respectively. The precise values of  $\nu$ ,  $\dot{\nu}$ ,  $\ddot{\nu}$  and other relevant information to barycentering, known collectively as the ephemeris, was obtained from the Jodrell Bank group, which is published monthly for the Crab pulsar (PSR B0531+21) [92, Jodrell Bank group].

Cuts used for the Crab pulsar are different than those used for the nebula. The Crab pulsar is believed to be essentially a weak source sitting on top a strong source (the nebula). Cuts were determined by optimizing simulated gamma-rays with a powerlaw energy distribution of an index of -3.8 that is 3% of the Crab flux at 100 GeV, with Crab Nebula data being used as background. The cuts that were optimized and used in the analysis for the three observing seasons are summarized in table 5-3 [93]. Also, a cut on the elevation of the telescopes was used to keep the energy threshold as low as possible. Any run below an elevation of  $55^\circ$  was not used in the analysis.

Table 5.2. Cuts used for the Crab Pulsar during three seasons of observation

Cut	2007-2008	2008-2009	2009-2010
SIZE [dc]	150	150	100
Pairs to deny	T1T4	T1T4	None
MSL Upper	1.03	1.10	1.35
MSW Upper	1.08	1.03	1.17
HSM Lower [km]	6.4	6.8	6.6
$\theta^2$ [deg <sup>2</sup> ]	0.133	0.076	0.072

The final result of producing the folded lightcurve (also known as a phase histogram or phasogram, a portmanteau combining the words phase and histogram), is shown in figure 5-4. As a comparison to what is seen at other wavelengths, the Crab pulsar in optical wavelengths is shown in figure 5-5. The Crab pulsar has two peaks, a main peak (P1) and a second smaller peak (P2) called the interpulse. As seen in figure 5-4, there is excess above the nebular emission for P2, but not for P1, at a level of  $3.7\sigma$ .

There are several statistical tests to confirm whether or not the excess at P2 is an actual pulsation or a fluctuation in the nebula emission. Like the significance used to test for nebular emission, a significance of over five is required for a positive detection. The first test used was the  $\chi^2$  statistic, where a constant was fit to the phase histogram. The red dashed line in figure 5.4 represents the constant. The  $\chi^2$  value is roughly the statistical significance per degree of freedom. The probability of pulsations being a chance statistical fluctuation is then calculated from a  $\chi^2$  distribution. In this case, the Crab pulsar data has a reduced  $\chi^2$  of 2.07 per degree of freedom for 10 degrees of freedom. This is a chance probability of 0.023,  $1.6\sigma$ , converting that probability to a Gaussian significance level.

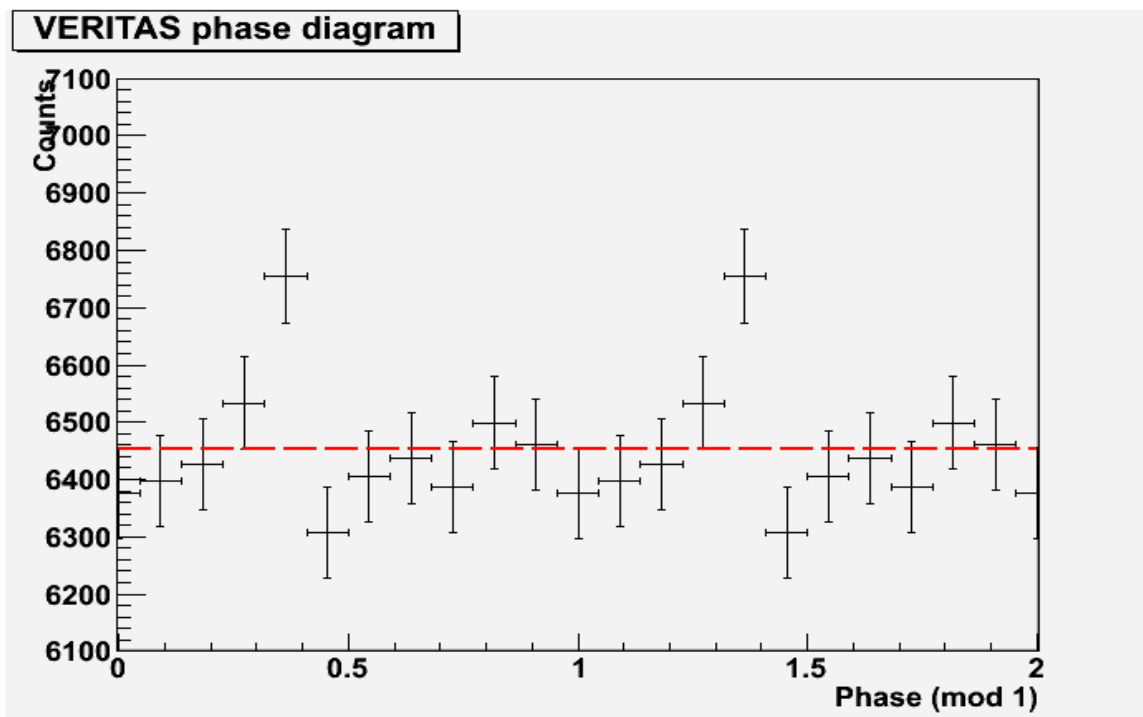


Figure 5-4. Phase histogram for Crab Pulsar data over two periods. The red dashed line represents the best fit to a constant value.

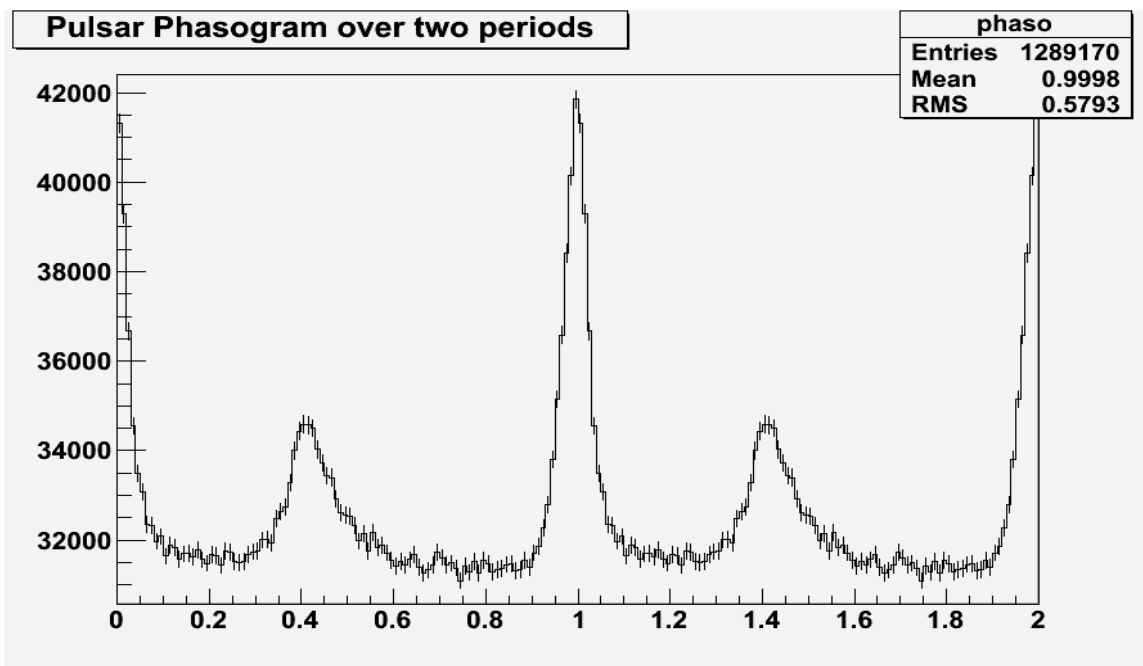


Figure 5-5. Optical data of the Crab Pulsar taken from the Multiple Mirror telescope (MMT), located on Mt. Hopkins, AZ.

The second is the  $Z_1^2$  (or Rayleigh test statistic), where  $Z_n^2$  is defined as the following:

$$Z_n^2 = \frac{2}{N} \sum_{j=1}^n \left[ \left( \sum_{i=1}^N \sin(2\pi j \varphi_i) \right)^2 + \left( \sum_{i=1}^N \cos(2\pi j \varphi_i) \right)^2 \right] \quad \text{Eq. 5.3}$$

In the limit of  $N > 100$  events, the  $Z_n^2$  statistic is roughly the  $\chi^2$  statistic for  $2n$  degrees of freedom (ref#). Only the first harmonic  $n = 1$  was tested in this work, which will only test for the broadest features in the folded light curve. The Crab pulsar data has a  $Z_1^2$  value of 1.7 for 2 degrees of freedom, corresponding to a chance probability of 0.43.

The third statistic used was a significance using the P2 as the ON region and the remaining regions of the phase histogram as the OFF region. This test is only used if the pulse profile is well-defined at other wavelengths, such as for the Crab pulsar. The significance was calculated using equation 3.9. The P2 ON region is defined from 0.32 to 0.43 in phase, the same as MAGIC [28] and EGRET before it [94], making alpha equal to 0.12. This gave the highest detection probability of the three statistical tests, giving a significance of  $3.71\sigma$ , or a probability of  $2.1 \times 10^{-4}$  that the peak at P2 is not a statistical fluctuation.

Figure 5-6 shows the distribution in energy of the photons. The background, shown in blue is the distribution of photons in the OFF regions that have been scaled down to the size of the ON region by a factor of  $\alpha$ . Figure 5-7 shows the distribution of energies for the photons in the ON region subtracting the photons in the OFF regions.

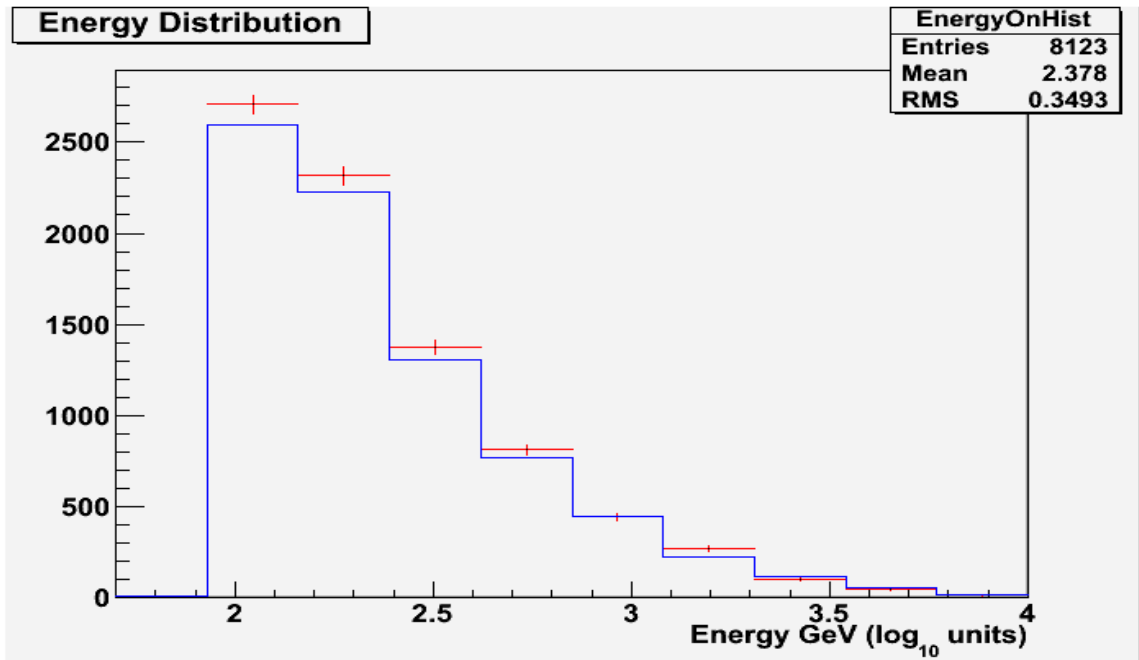


Figure 5-6. ON and OFF distributions of pulsed photons, where the ON region is defined as the P2 region. ON region photons are shown in red, while OFF region distribution is blue.

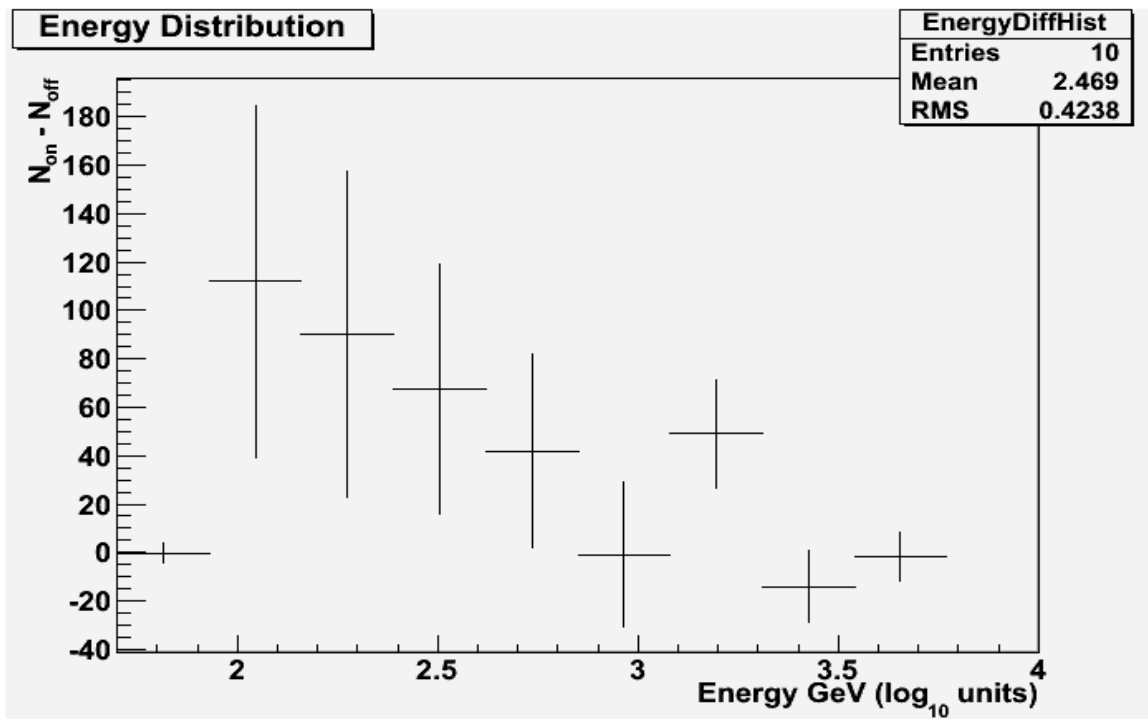


Figure 5-7. Distribution of energy of the excess pulsed photons for the Crab pulsar at the P2 position.

An upper limit on the flux of the Crab pulsar can now be calculated. First, a measurement is made of the standard deviation a particular bin of the folded lightcurve. Using Poisson statistics, this would be the square root of the mean of the phase histogram. The upper limit of counts in any bin at a  $5\sigma$  confidence level would be five times the standard deviation. Dividing by the rate and effective area would give you the flux upper limit at  $5\sigma$  confidence. Analytically, this is expressed in equation 5.4:

$$F_{UL,5\sigma} \cong \frac{5\bar{N}^{1/2}}{TA_{eff}} \quad \text{Eq. 5.4}$$

where  $T$  is the exposure time on the source,  $A_{eff}$  is the effective area (approximately  $1 \times 10^5 \text{ m}^2$ ), and  $\bar{N}$  is the mean number of counts in the lightcurve. Evaluating equation 5.4 for the Crab pulsar gives an  $5\sigma$  upper limit of  $2.8 \times 10^{-12} \text{ photons/cm}^2/\text{s}$  above 160 GeV for a pulse width less than of 9% of the pulse phase.

## 5.2. G54.1+0.3/PSR J1930+1852 & PSR J1928+1746

### 5.2.1. Cuts and Data Set Used for Analysis

G54.1+0.3 was observed by VERITAS for 31 hours using data in the 2007-2008 and the 2008-2009 observing seasons, before the T1 move. Only the runs with south and west wobble pointing have PSR J1928+1746 in the FOV, giving only half of the total time on that source. The spectrum of G54.1+0.3 is harder than the Crab spectrum, consistent with other PWN observed at TeV energies. A higher size cut gave more optimal results for that reason. The cuts used for G54.1+0.3 in this work are summarized in Table 5.3. They are for a point-like, hard spectrum, optimized on 5% of the Crab excess.



Table 5.3. Cuts used for G54.1+0.3 and PSR J1930+1852

Cut	G54.1+0.3	PSR J1930+1852
SIZE [dc]	1000	200
Deny	T1T4 pairs	T1T4 pairs
HSM Lower [km]	Not used	7.0 km
MSW Upper	1.08	1.06
MSL Upper	1.19	1.30
$\theta^2$ [deg <sup>2</sup> ]	0.0121	0.02

### 5.2.2. Results of Observations of Nebulae

The resulting sky maps from the observations with VERITAS are shown in figure 5-8 and 5-9. These maps show that there is a significance excess that is consistent with the position of the pulsar and PWN. At the point of maximum significance, there are 61.2 excess counts above background, detecting G54.1+0.3 at the  $6.02\sigma$  level.

The PMT circle in the lower left corners of the maps help to illustrate that this is a point source. The point-spread function (PSF) of VERITAS varies with time and energy but is consistently smaller than the diameter of the PMT, which each PMT subtends  $0.15^\circ$  of the sky. Due to changes in the alignment and the T1 move, the PSF has gotten smaller in the most recent data.

Figure 5-10 shows the significance distribution of the sky map of G54.1+0.3. In the case of the absence of a source, the distribution should be Gaussian with mean of zero and a width of one. A positive source detection should show deviations from the Gaussian in the upper tail above  $4\sigma$ . This is the case in of G54.1+0.3, shown in figure 5-10. Figure 5-10 is contrasted by figure 5-11, which is the same distribution except without bins in the source exclusion region for G54.1+0.3.

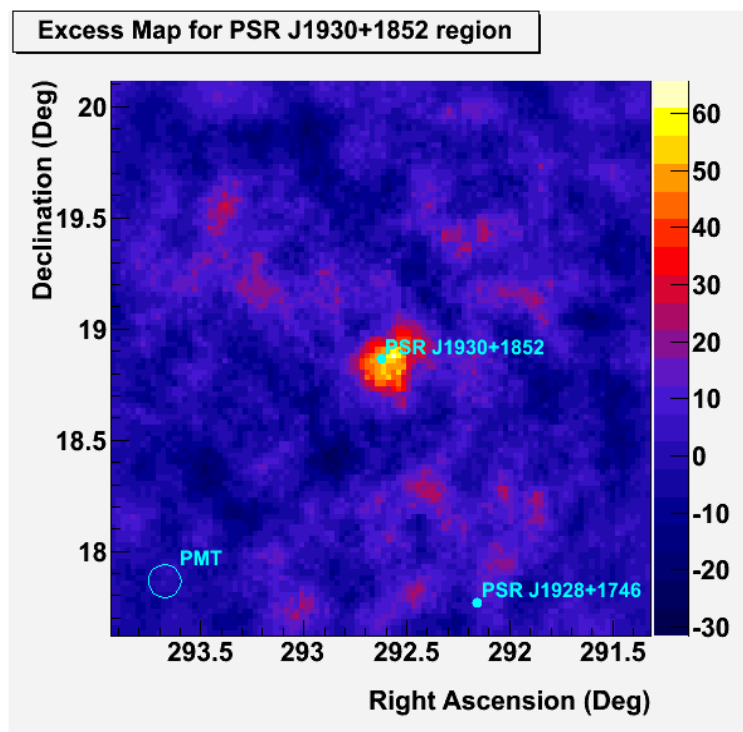


Figure 5-8. Excess map for the G54.1+0.3 region

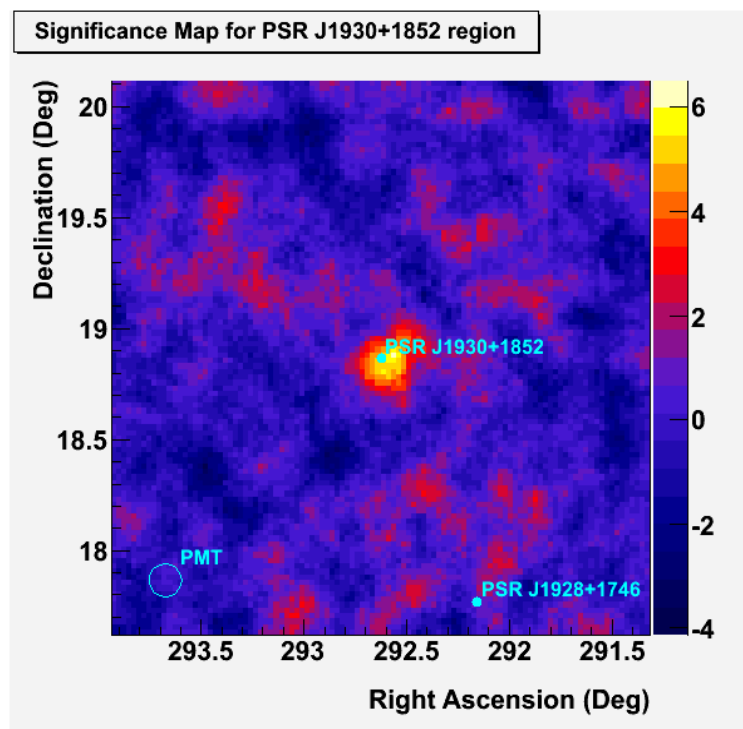


Figure 5-9. Significance map for the G54.1+0.3 region

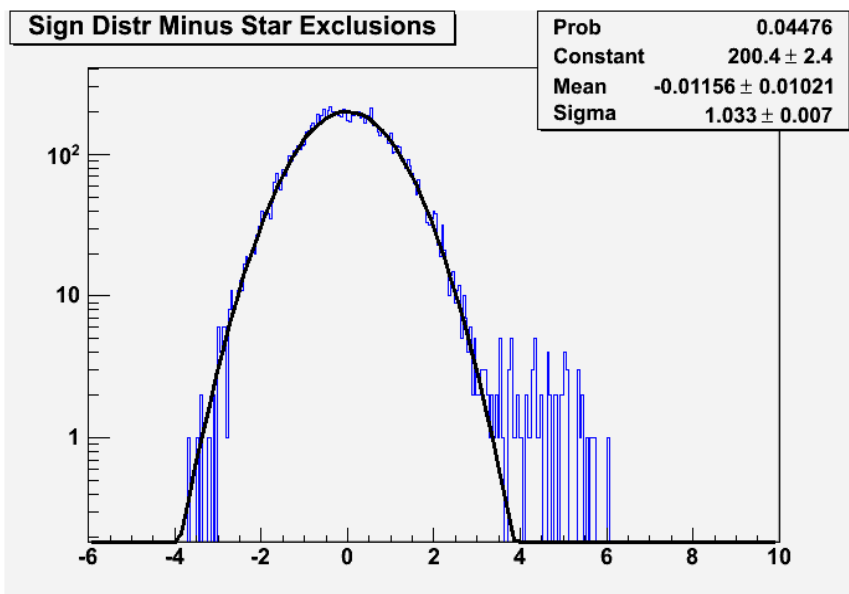


Figure 5-10. Significance distribution of the G54.1+0.3 sky region. The best fit Gaussian function is shown as the black curve

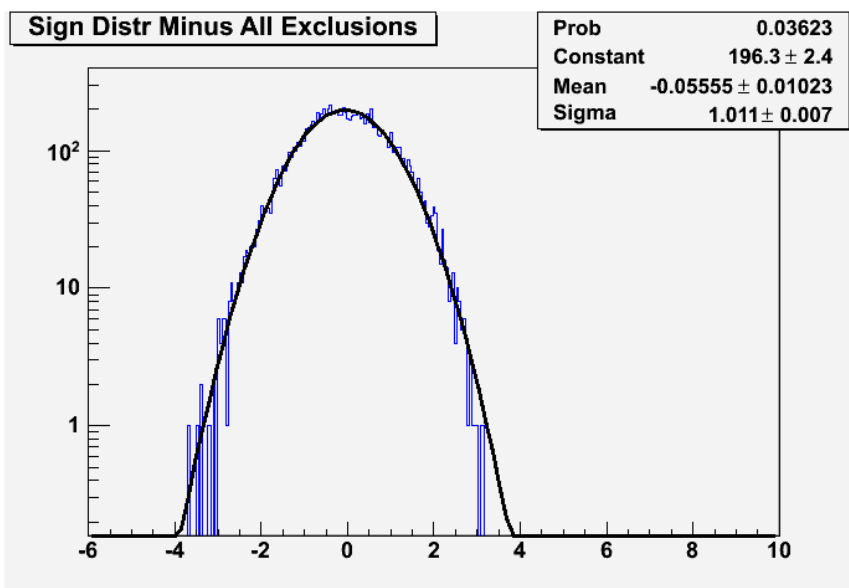


Figure 5-11. Significance distribution of the G54.1+0.3 sky region, excluding a region of  $0.3^\circ$  around G54.1+0.3

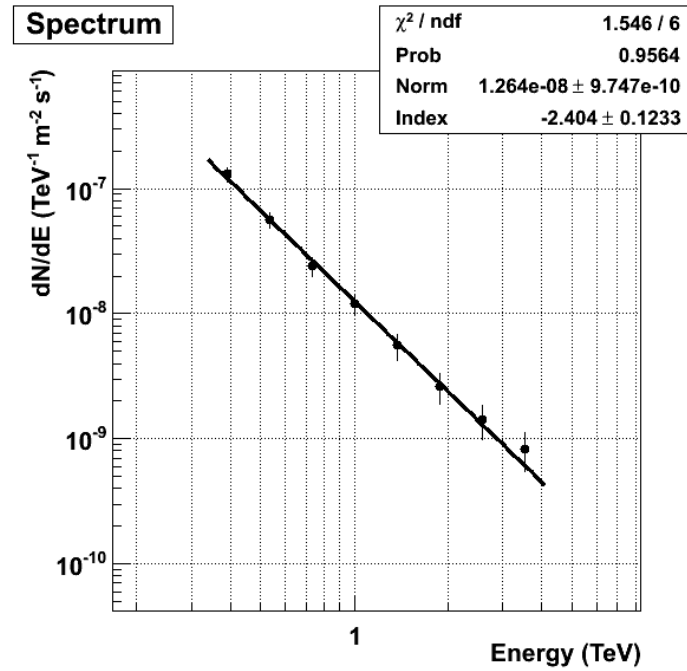


Figure 5-12. Spectrum for G54.1+0.3, fit to a powerlaw of the form in equation 5.1.

The spectrum for G54.1+0.3 is best fit by a powerlaw of the form in equation 5.1, as seen in figure 5-12. The best fit values for the spectrum of G54.1+0.3 is  $k = (1.26 \pm 0.10) \times 10^{-8} \text{ TeV}^{-1} \text{ m}^{-2} \text{ s}^{-1}$  and  $\Gamma = -2.4 \pm 0.1$ . The integrated flux above 1 TeV is  $(9.00 \pm 1.44) \times 10^{-9} \text{ m}^{-2} \text{ s}^{-1}$  or about 4% of the Crab Nebula flux.

PSR J1928+1746 is shown in the same FOV, as seen in figures 5-6 and 5-7, about  $\sim 1.1$  deg away from PSR J1930+1852. The position at PSR J1928+1746 does not have a significance above  $5\sigma$ , and therefore not a detection. Figure 5-9, which shows the significance distribution of the region excluding around G54.1 + 0.3, also shows a null detection. An upper limit of the possible VHE flux at that position is instead calculated. The flux upper limit is calculated by:

$$F_{UL,5\sigma} = F_{Crab} (R_{UL,5\sigma} / R_{Crab}) \quad \text{Eq. 5.5}$$

Where  $R_{UL,5\sigma}$  the upper limit on the  $\gamma$ -ray is rate of the source with a  $5\sigma$  confidence, and  $R_{Crab}$  is the  $\gamma$ -ray rate of the Crab Nebula using the same set of cuts. The  $5\sigma$  upper limit on rate is calculated using standard deviation using Poisson statistics similar to the Crab pulsar in equation 5.4. Here we assume that the flux of the source has a spectral index the same as the Crab, and exploit the fact that the  $\gamma$ -ray rate is proportional to the flux of the source. At the position of PSR J1928+1746, using the set of cuts in table 5-3, the analysis yields -10.9 excess counts at a significance of  $-0.91\sigma$ . The 95% upper limit of rate is 10.6 counts, with a Crab Nebula rate of  $2.01 \pm 0.11$   $\gamma$ /min for the set of cuts for G54.1+0.3 in table 5.3, giving a upper limit of 2.0% of the Crab Nebula flux above 400 GeV.

### 5.2.3. Pulsar Analysis for PSR J1930+1852

The difference in the analysis for the Crab pulsar and PSR J1930+1852 (and the other pulsars discussed in this work) is that only the Crab has a strong VHE nebular background. Cuts used for pulsars other than the Crab are optimized for weaker source strengths and softer spectral distributions, assuming that the pulsar falls off in a manner similar to than the Crab Pulsar. The cuts used for PSR J1930+1852 are summarized in the far right column of table 5-3.

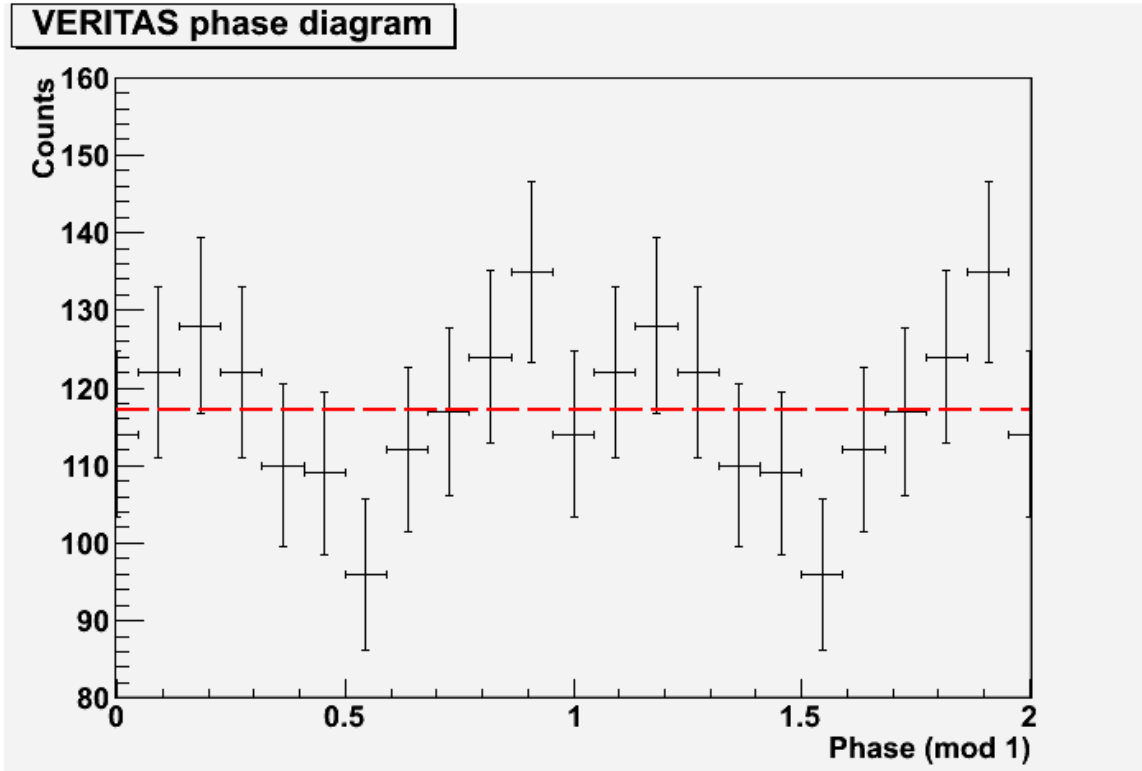


Figure 5-13. Phase histogram for PSR J1930+1852. The dashed red line is the best fit to a constant value.

The pulsar timing analysis using ephemeris data given by [95], yielded a non-detection of PSR J1930+1852. The  $Z_1^2$  statistic was 5.84, while the reduced  $\chi^2$  statistic gave  $1.01\sigma$  for 10 degrees of freedom. The  $5\sigma$  upper limit is  $5.1 \times 10^{-13}$  photons/cm<sup>2</sup>/s above 200 GeV for a pulse width of less than 9% of the pulse period.

### 5.3. The Boomerang PWN and PSR J2229+6114

#### 5.3.1. Cuts used and data set

The Boomerang PWN was observed by VERITAS for a total of 55.7 hours live time over the three observing seasons from fall 2007 to summer 2010. 10.8 hours of this data was taken during the 2007-2008 season, 32.2 hours during the 2008-2009 season, and 12.7

hours during 2009-2010. Standard VERITAS data is taken with a  $0.5^\circ$  offset, often referred to as wobble mode observations, from the source location. After initial analysis of the data showed possible extension of the source,  $0.7^\circ$  wobble runs were taken to encompass larger background regions. Both  $0.5^\circ$  and  $0.7^\circ$  offsets are used in this work for the source detection, however, the runs with pointing at  $0.5^\circ$  both south and west of the source are removed for the spectral analysis, since they did not provide any usable background regions. A wider  $\theta^2$  cut was used for the spectral analysis ( $0.09 \text{ deg}^2$ ) to attempt to encompass as much as the VHE excess as possible for the spectrum.

Cuts used for the analysis are for an extended source optimized on 5% of the Crab flux. They are summarized in Table 5.4.

Table 5.4. Cuts used for G106.3+2.7 and PSR J2229+6114

Source	G106.3+2.7		PSR J2229+6114	
	OVA	NVA	OVA	NVA
Array	400	400	200	200
SIZE [dc]	400	400	200	200
Deny	T1T4 pairs	None	T1T4 pairs	None
HSM Lower [km]	Not used	7.0	7.0	8.0
MSW Upper	1.08	1.10	1.06	1.13
MSL Upper	1.19	1.32	1.30	1.15
$\theta^2$ [ $\text{deg}^2$ ]	0.04	0.04	0.02	0.019

### 5.3.2. Results of observations of the PWN G106.3+2.7

The 2-d sky maps are shown in figure 5-14 and figure 5-15. The excess map shows an extended region of VHE excess southeast of the pulsar. The peak significance point is located  $0.46^\circ$  southwest of the pulsar position. The peak significance location has an excess of 194.9 counts with a significance of  $7.51\sigma$ . The pulsar position has 85.8 excess counts with a significance of  $3.38\sigma$  using the RBM background analysis method.

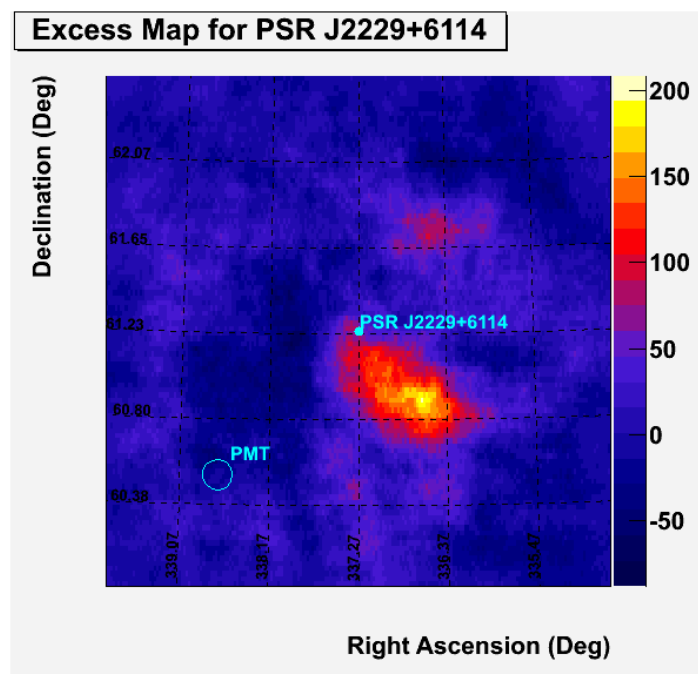


Figure 5-14. Excess map of the G106.3+2.6 region. The pulsar position is shown by the light blue point. A PMT is drawn for scale.

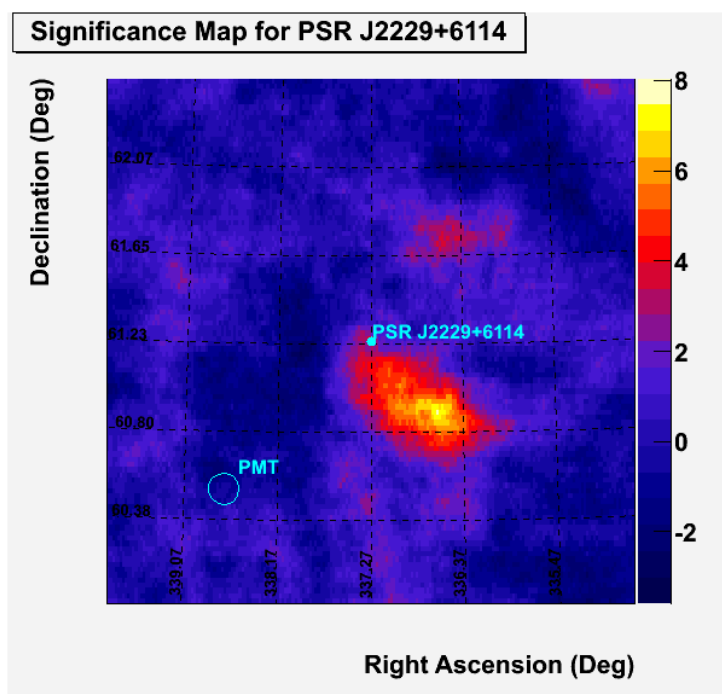


Figure 5-15. Significance map of the G106.3+2.6 region. The pulsar position is shown by the light blue point. A PMT is drawn for scale.



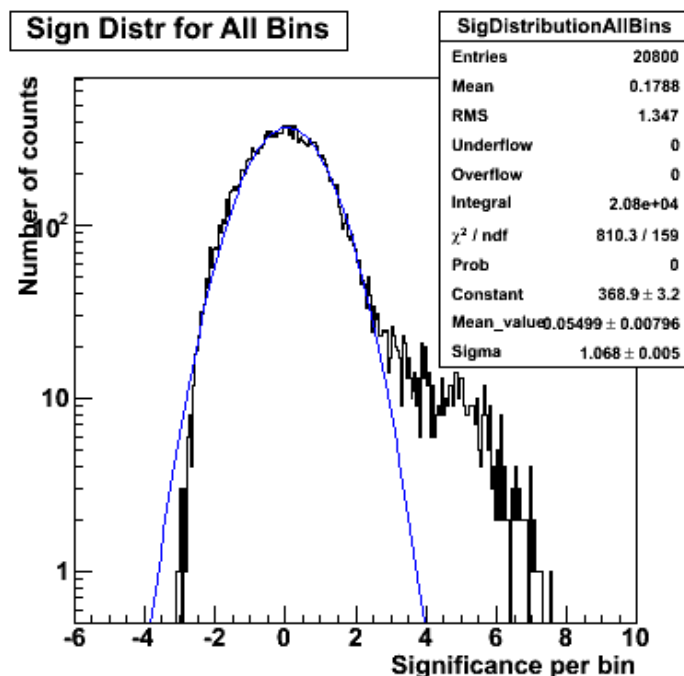


Figure 5-16. Significance distribution of the G106.3+2.6 region. A Gaussian best fit is shown as a blue curve on the figure.

The significance distribution, figure 5-16, is wider and with a higher mean than the typical significance distribution, which is typical for a sky map with a detected source in the FOV.

The excess count map for G106.3+2.7 was modeled with a 2-D elliptical Gaussian function to determine the amount of extension of the source. The best fit of the Gaussian for the source has a  $0.48^\circ$  full-width half-maximum (FWHM) along the major axis and  $0.30^\circ$  FWHM along the minor axis, placing the pulsar position within the ellipse. The ellipse is orientated  $54.3^\circ$  below the galactic plane going in a clockwise direction.

The spectrum for G106.3+2.7 is shown in figure 5-17. It is fit with a powerlaw function (equation 5-1) with best fit values are  $k = (1.78 \pm 0.51) \times 10^{-8} \text{ TeV}^{-1} \text{ m}^{-2} \text{ s}^{-1}$  and  $\Gamma = 2.191 \pm 0.256$ . The integrated flux above 1 TeV is therefore  $9.31 \times 10^{-9} \text{ m}^{-2} \text{ s}^{-1}$ , or about 5% of the Crab Nebula flux.

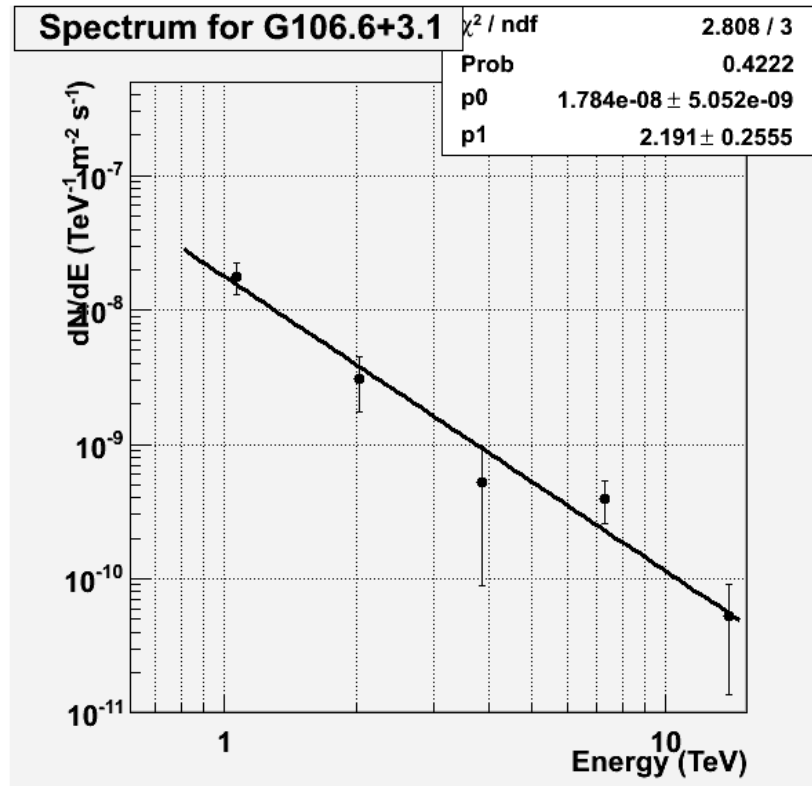


Figure 5-17. VERITAS spectrum of G106.3+2.7. The black line shown is the best fit to the powerlaw function.

### 5.3.3. Pulsar analysis of PSR J2229+6114

The pulsar analysis for PSR J2229+6114 performed in a very similar manner as the analysis for PSR J1930+1852. The only difference was that data from before and after the T1 move was used. Soft analysis cuts used on PSR J2229+6114 are listed in table 5-4. The cuts from before the T1 move are identical to the ones for PSR J1930+1852. Ephemeris data was obtained from the FERMI LAT database [96].

The results of the pulsar analysis (shown in figure 5-18) show a null detection of PSR J2229+6114. The Rayleigh test resulted in  $Z_1^2 = 5.41$  with two degrees of freedom and a reduced  $\chi^2$  of  $0.99\sigma$  for ten degrees of freedom. The  $5\sigma$  confidence upper limit is  $2.8 \times 10^{-12}$  photons/cm<sup>2</sup>/s above 200 GeV for a pulse width less than 9% of the pulse period.

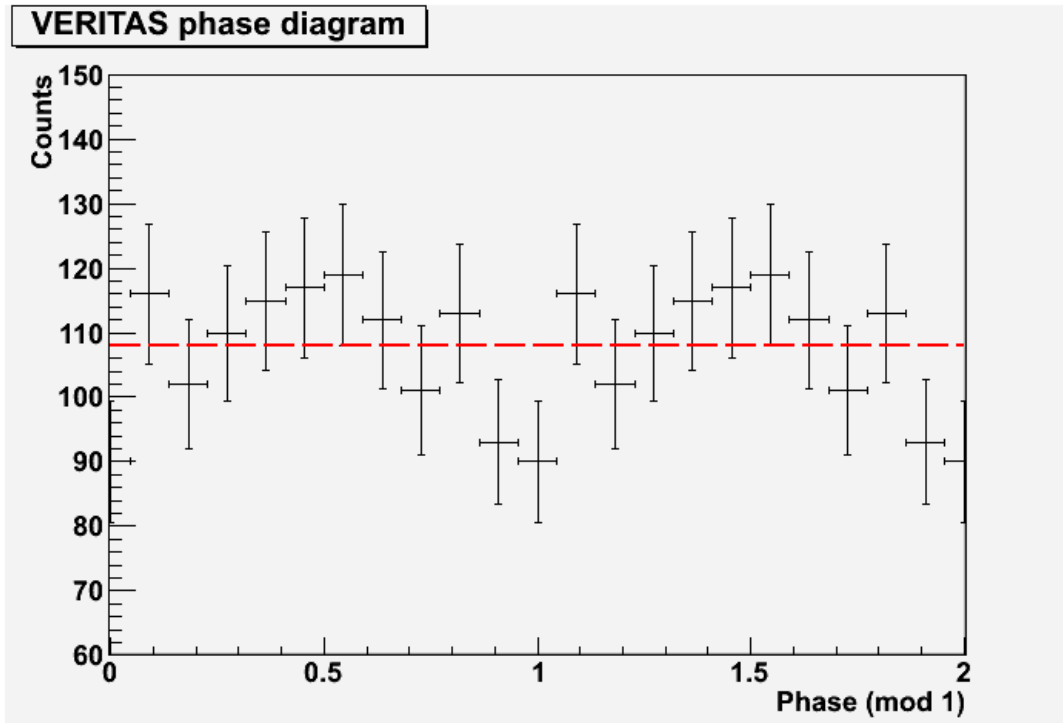


Figure 5-18. Phase histogram for PSR J2229+6114. The dashed red line is the best fit to a constant value.

#### 5.4. HESS J1857+026/PSR J1856+0245

##### 5.4.1. Cuts used and data set

The initial VERITAS data taken in the region of HESS J1857+026 was targeted at the supernovae remnant W44 late in the 2007-2008 observing season. After twenty hours of observation centered at W44, initial analysis of the data showed significant excess centered on the published locations HESS unidentified sources HESS J1857+026 and HESS J1858+020 [81]. Since HESS J1857+026 can only be seen in the north and east wobble runs in the W44 data, only ten hours of the W44 data was used in this analysis. An additional seven hours was taken targeting HESS J1857+026 during the summer of

2008 and three more hours during the spring of 2010, bringing the total observation time to twenty hours.

The cuts used for the HESS UNID are identical to the cuts used for G106.3+2.7 in table 5-4, with the exception of using  $\theta^2 < 0.023$ , which was the same value used in the HESS paper [81]. Once again, a wider  $\theta^2$  cut ( $0.09 \text{ deg}^2$ ) was used for the spectral analysis.

#### 5.4.2. Observation results of HESS J1857+026

The excess counts map and significance map of HESS J1857+026 are shown in figures 5-19 and 5-20, respectively. They show a significant excess in the region, centered on HESS J1857+026. PSR J1856+0245 and the maximum significance locations of VERITAS are both close to the HESS position. The significance distribution, figure 5-19, is consistent with a detected source. The point of maximum significance had an excess of 136.8 excess counts giving  $6.35\sigma$ , at a point  $0.095^\circ$  away from the HESS position. The center of the HESS emission had 102.7 excess counts at  $4.72\sigma$ .

Both HESS and VERITAS data show that the source is extended. The VHE excess for VERITAS was modeled as a 2-D elliptical Gaussian, using the same procedure as for G106.3+2.7. The fit results were that the major axis FWHM was  $0.51^\circ$ , and the minor axis was  $0.32^\circ$ . The orientation of the ellipse was  $3.9^\circ$  below the galactic plane.

HESS J1858+020 is also within the same FOV, located about 0.8 deg away, as seen in the excess counts and significance maps. HESS J1858+020 was not detected by VERITAS, although there is an excess at that position. There was 59.5 excess events at that position with a significance of  $3.32\sigma$ . An upper limit of 3.2% with  $5\sigma$  confidence of the Crab flux above 1TeV was placed at the position of HESS J1858+020, using the same method as for PSR J1928+1746. This is consistent with the HESS spectrum of 2.4% of the Crab spectrum.

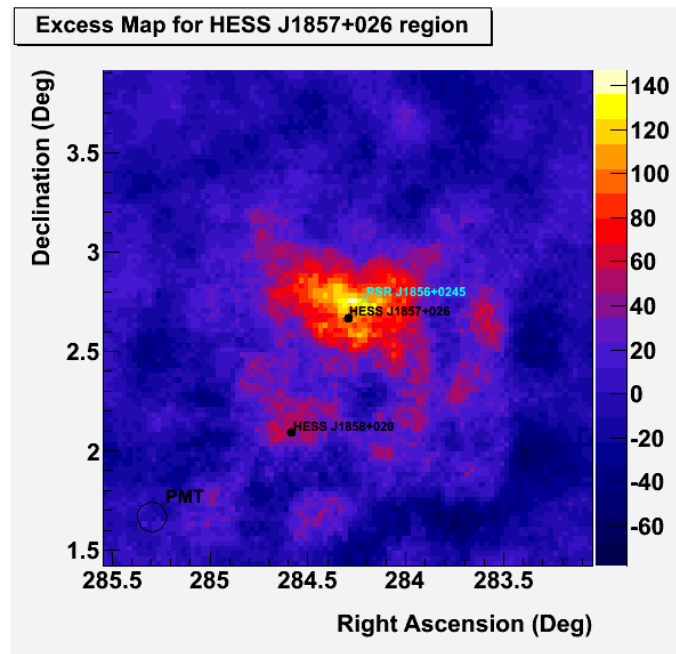


Figure 5-19. Excess counts map in the HESS J1857+026 FOV. The blue cross represents the pulsar position, and the black points are the two HESS UNID sources.

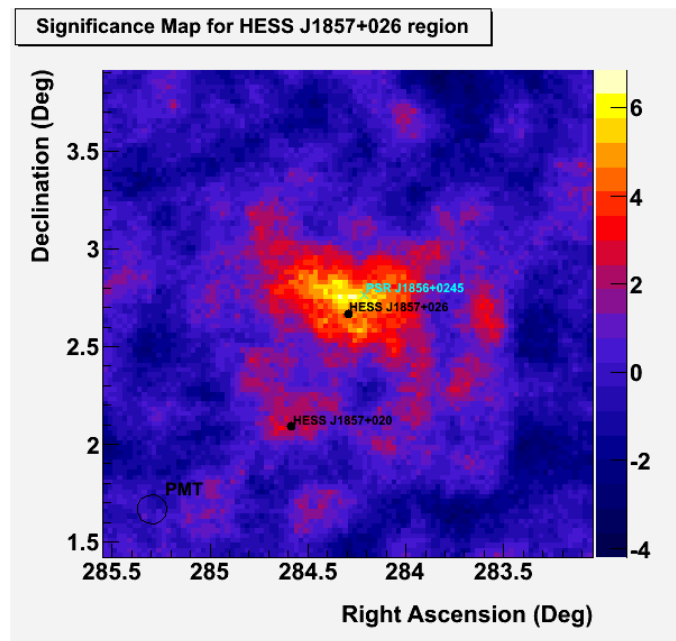


Figure 5-20. Significance map in the HESS J1857+026 FOV. The blue cross represents the pulsar position, and the black points are the two HESS UNID sources.

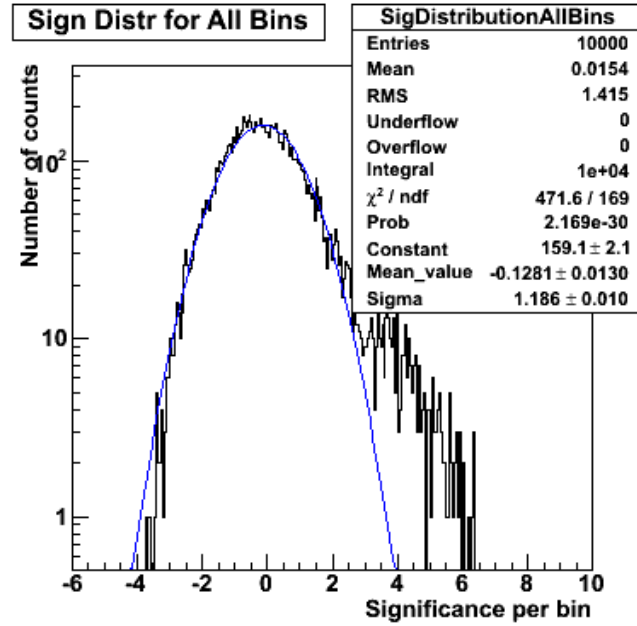


Figure 5-21. Significance distribution in the HESS J1857+026 FOV. The blue curve is the best fit to a Gaussian function.

The spectrum of HESS J1857+026 is shown in figure 5-22. The spectrum is fit to a powerlaw (equation 5-1). The best fit values are  $k = (5.44 \pm 0.92) \times 10^{-9}$  photons/TeV/m<sup>2</sup>/s and  $\Gamma = -2.319 \pm 0.261$ . These values agree with the HESS spectral values of  $k = (6.1 \pm 0.7) \times 10^{-9}$  photons/TeV/m<sup>2</sup>/s and  $\Gamma = -2.39 \pm 0.08$ .

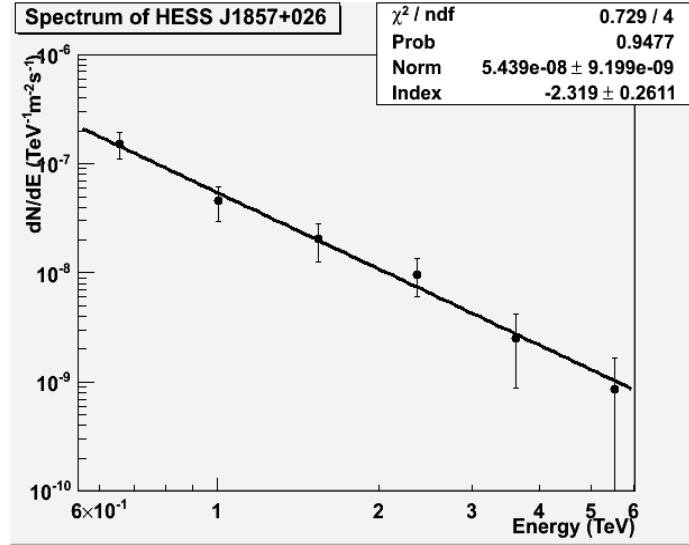


Figure 5-22. Spectrum of HESS J1857+026. The black line represents the best fit of the spectrum to a powerlaw of the form of equation 5.1.

#### 5.4.3. Pulsar Analysis of PSR J1856+0245

The cuts used in the analysis of PSR J1856+0245 are the same as for PSR J2229+6114 (table 5-4). The ephemeris data was obtained from the radio observations that detected the source [23]. The statistical test results were  $Z_1^2 = 2.42$  and a reduced  $\chi^2 = 1.04\sigma$  for ten degrees of freedom. The pulsar was not detected. The phase diagram is shown in figure 5-23. The pulsar upper limit is  $9.1 \times 10^{-13}$  photons/cm<sup>2</sup>/s above 200 GeV with  $5\sigma$  confidence for a pulse width less than 9% of the pulse period.

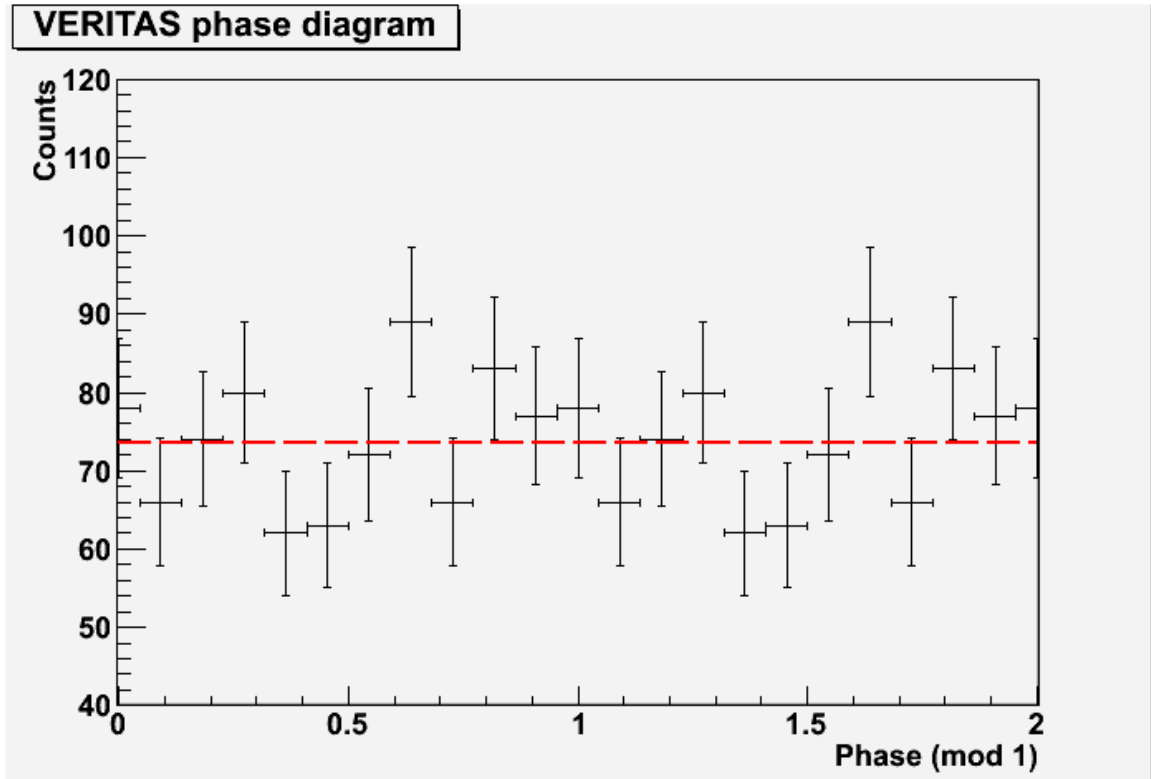


Figure 5-23. Phase histogram of PSR J1856+0245. The red dashed line represents the best fit of the phase histogram to a constant value.

## 5.5. 3C58 & PSR J0205+6449

### 5.5.1. Cuts used and data set

3C58 was observed for a total of 22 hours before the T1 move, 18 hours were quality selected to be in the analysis. Cuts reported in this work are the same as used for G106.3+2.7, except for a point source, so a  $\theta^2$  cut of  $0.0169 \text{ deg}^2$  is used.

### 5.5.2. Observation results for 3C58

The excess counts and significance maps of 3C58 are shown in figures 5-22 and 5-23 respectively. The highest significance in any bin in the significance skymap is  $3.72\sigma$ . Since there are no bins above  $5\sigma$  in the region around 3C58, it is not detected in VHE by



VERITAS. This is further illustrated in the significance distribution, figure 5-24, which is consistent with a null detection.

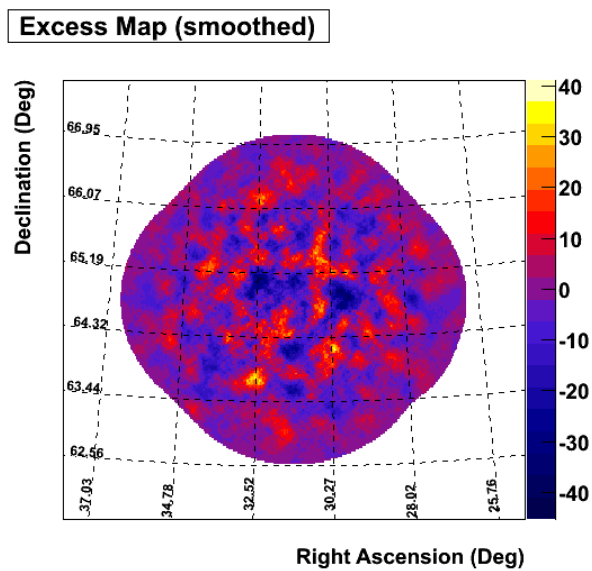


Figure 5-24. Excess Map of the 3C58 FOV

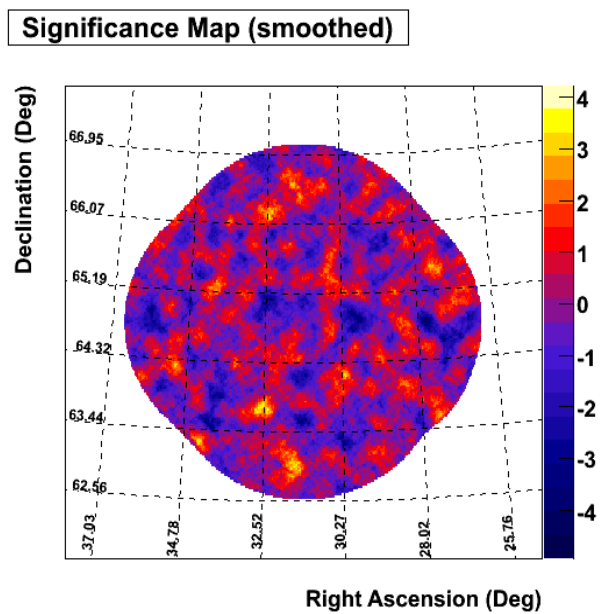


Figure 5-25. Significance Map of the 3C58 FOV

At the location of 3C58, there are 5.97 excess counts at a significance of  $0.31\sigma$ . An upper limit of 2.2% of the Crab Nebula flux with  $5\sigma$  confidence is placed at the location of 3C58 above 400 GeV.

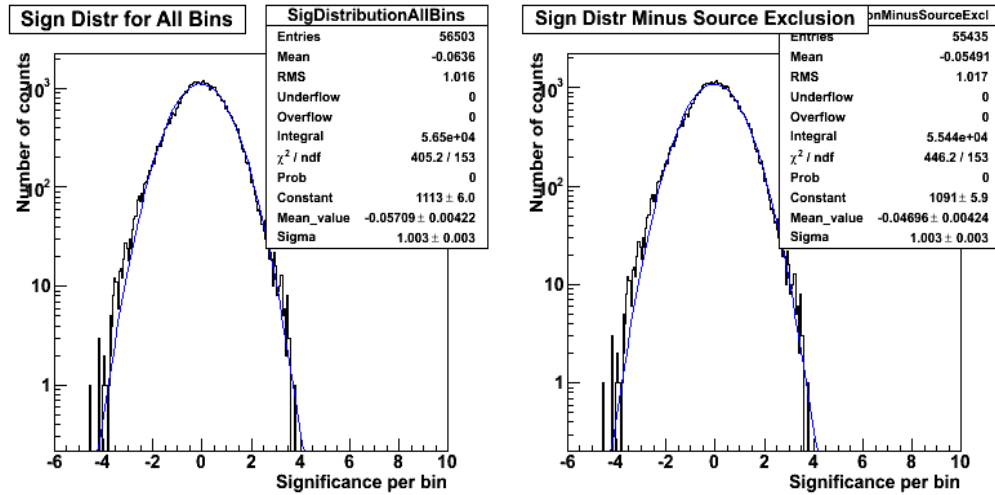


Figure 5-26. Significance distributions of 3C58 with the  $0.3^\circ$  source exclusion around 3C58 (right) and without the source exclusion (left). Both distributions are fit by a Gaussian function shown in blue.

### 5.5.3. PSR J0205+6449

The ephemeris information for PSR J0205+6449 was taken from the FERMI reported results [90]. The phase histogram is shown in figure 5-27. Cuts used for PSR J0205+6449 are the same as for PSR J2229+6114 (table 5-4). The results of the two statistical tests are:  $Z_1^2 = 1.42$  ( $0.71\sigma$  for two degrees of freedom) and a reduced  $\chi^2 = 1.56$  for 10 degrees of freedom. The pulsar PSR J0205+6449 was not detected. The pulsar upper limit is  $8.6 \times 10^{-13}$  photons/cm<sup>2</sup>/s above 200 GeV with  $5\sigma$  confidence for a pulse width less than 9% of the pulse period.

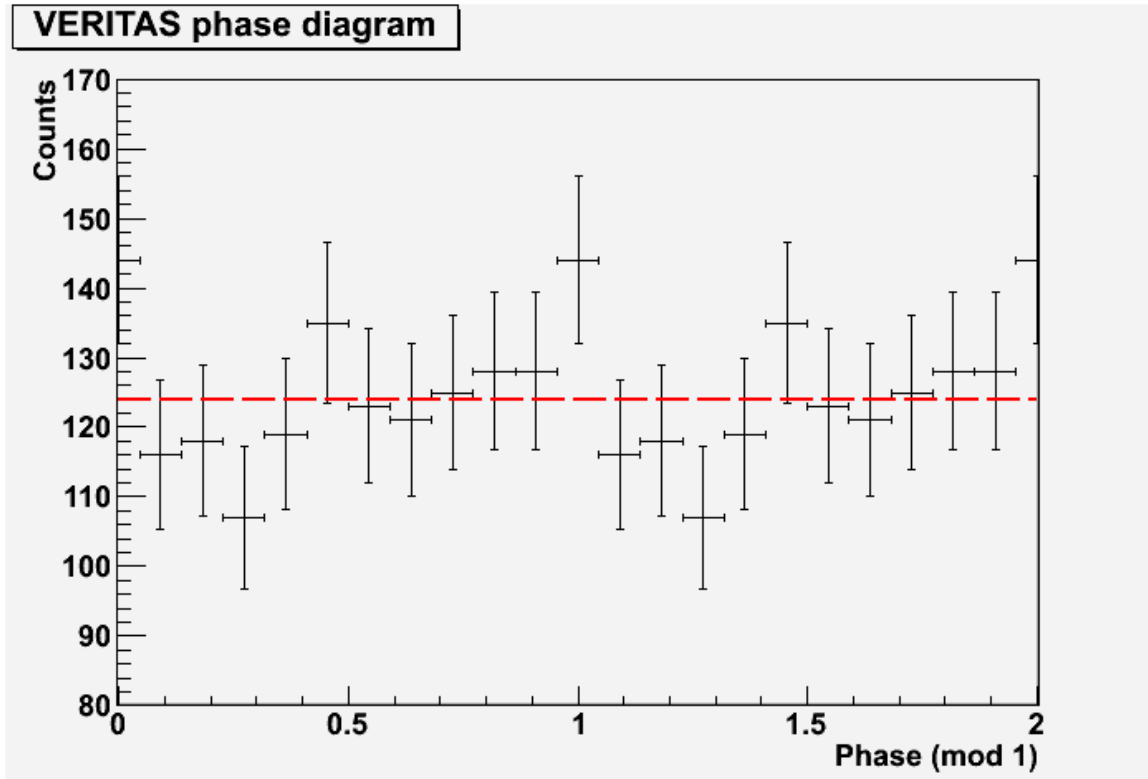


Figure 5-27. Phase histogram of PSR J0205+6449

## 5.6. Cisne PWN & PSR J2021+3651

### 5.6.1. Data set and cuts used

The PWN G75.2+0.1 was observed for 34 hours centered on PSR J2021+3651 late during the 2009-2010 observing season. The cuts that produced the highest significance are hard, weak and extended cuts optimized on the NVA data, listed in table 5-5.

Table 5.5 Cuts used for G75.2+0.1

Cut	Value
SIZE [dc]	1000
Deny	None
HSM Lower [km]	5.5
MSW Upper	1.09
MSL Upper	1.3
$\theta^2$ [deg <sup>2</sup> ]	0.04

### 5.6.2. Observation results of G75.2+0.1

Excess counts and Significance maps are shown in figures 5-28 and 5-29 respectively.

The maps show the location of PSR J2021+3651, the INTEGRAL source IGR J20188+3647, and the PWN CTB87, a PWN for which no known pulsar has been found. The maximum significance in the FOV is close to the location of IGR J20188+3647, which extends east to the location of PSR J2021+3651. At the location of PSR J2021+3651, there are 45.8 excess counts at a significance of  $3.3\sigma$ . The maximum significance location has 81.0 excess counts at  $6.03\sigma$ .

The morphology of the source is modeled as a 2-D Gaussian, the same as for G106.3+2.7 and HESS J1857+026. The best fit of the extension of the source has a FWHM of  $0.67^\circ$  along the major axis and  $0.31^\circ$  along the minor axis. The orientation of the Gaussian is  $9^\circ$  below the galactic plane.

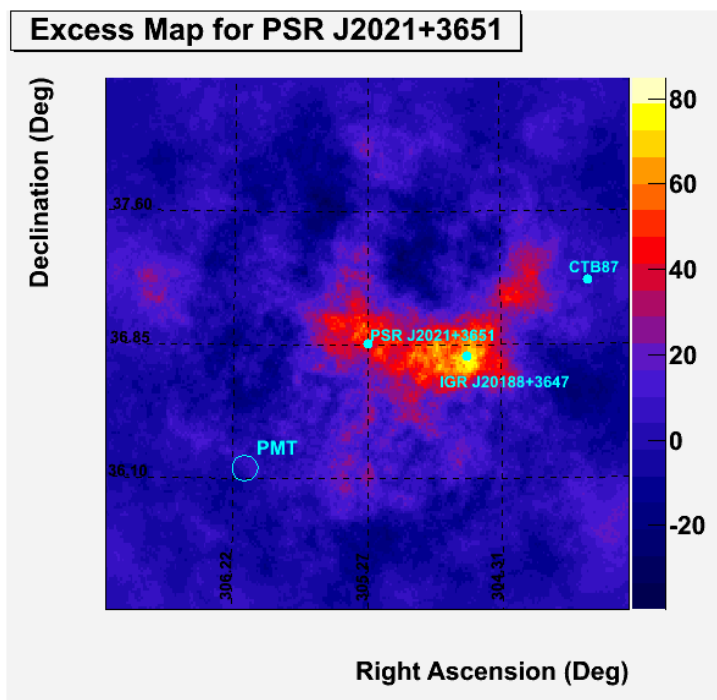


Figure 5-28. Excess counts map for G75.2+0.1. The light blue points indicate the positions of the PWNe and the INTEGRAL source IGR J20188+3647.

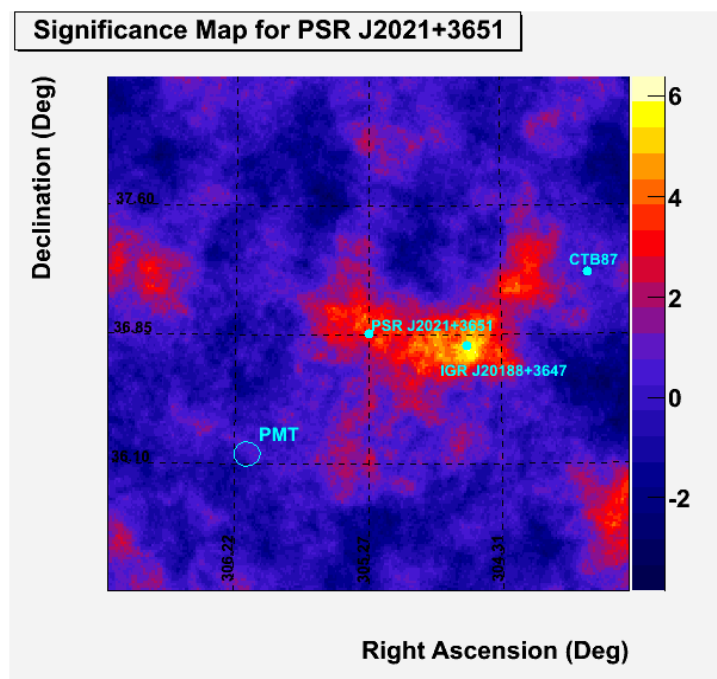


Figure 5-29. Significance map for G75.2+0.1. The light blue points indicate the positions of the PWNe and the INTEGRAL source IGR J20188+3647.

The significance distribution for G75.2+0.1 is shown in figure 5-30. The significance distribution is consistent with a detected source.

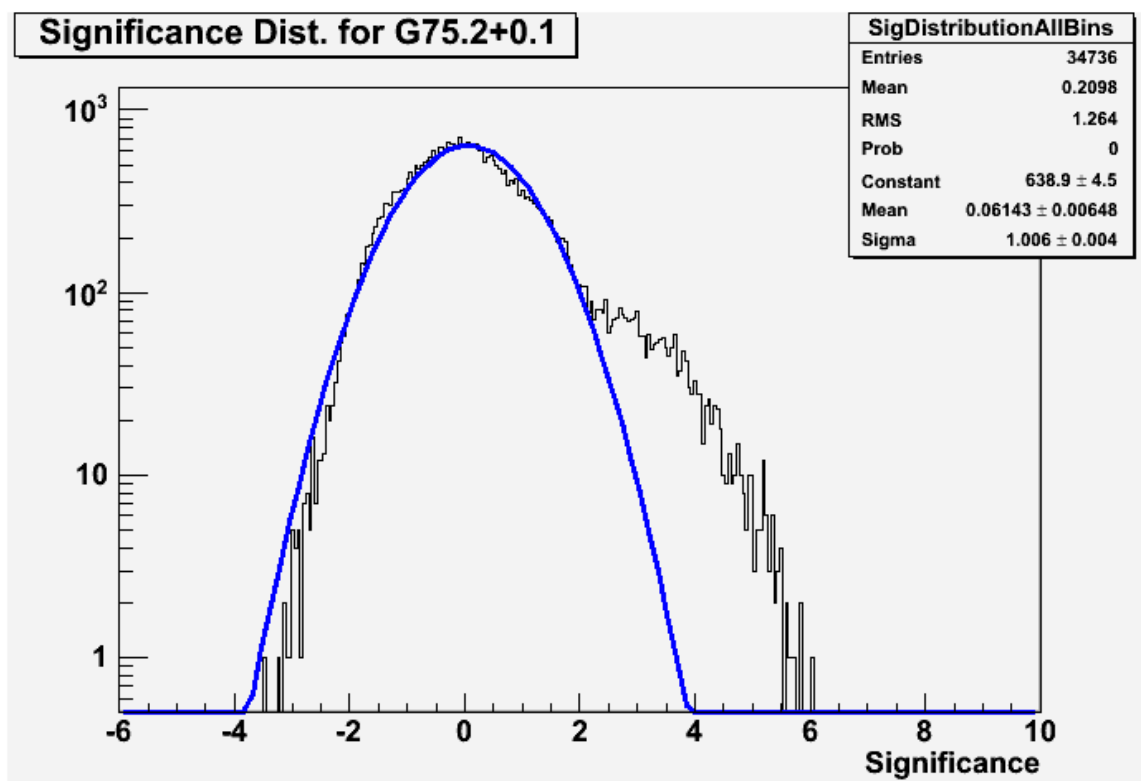


Figure 5-30. Significance Distribution of G75.2+0.1. The blue curve is the fit of the significance distribution to a Gaussian.

The spectrum of G75.2+0.1 is shown in figure 5-31. The best fit values of a powerlaw to this spectrum give the results of  $k = (5.93 \pm 1.84) \times 10^{-9} \text{ TeV}^{-1} \text{ m}^{-2} \text{ s}^{-1}$  and  $\Gamma = -1.35 \pm 0.21$ . This would make G75.2+0.1 (if the VHE emission is associated with G75.2+0.1) the hardest of any spectrum of PWN in VHE. The integrated flux above 1TeV is about 3% of the Crab Nebula flux.

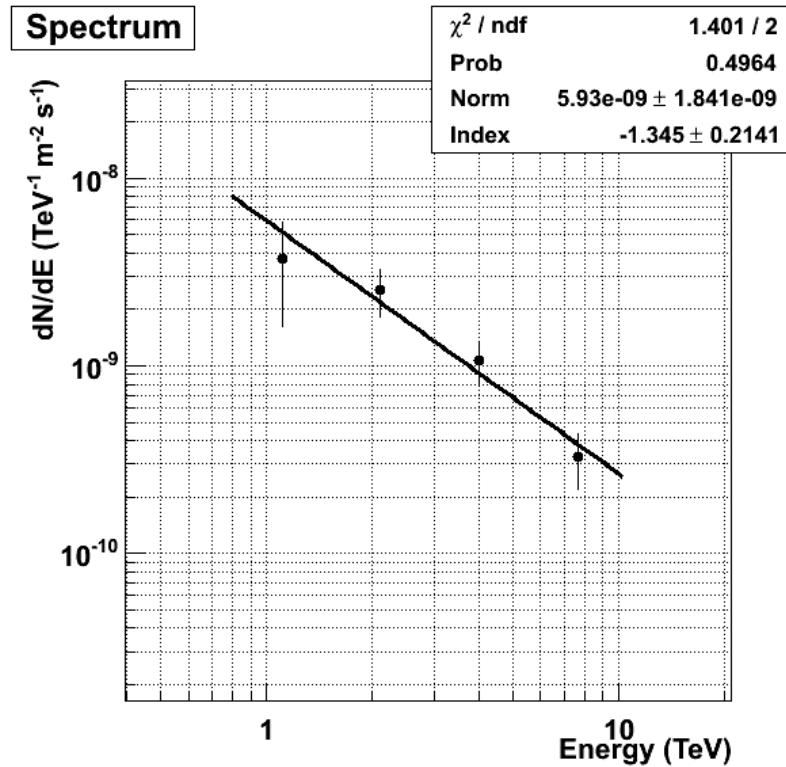


Figure 5-31. Spectrum of G75.2+0.1

### 5.6.3. PSR J2021+3651

The cuts used for PSR J2021+3651 are the same as used for the NVA data for PSR J2229+6114 in table 5-3. The phase histogram for PSR J2021+3651 is shown in figure 5-32. The statistical tests for pulsations in PSR J2021+3651 are  $Z_1^2 = 0.67$  and a reduced  $\chi^2$  of 2.7 for 10 degrees of freedom. The pulsar upper limit is  $6.9 \times 10^{-13}$  photons/cm<sup>2</sup>/s above 200 GeV with  $5\sigma$  confidence for a pulse width less than 9% of the pulse period.

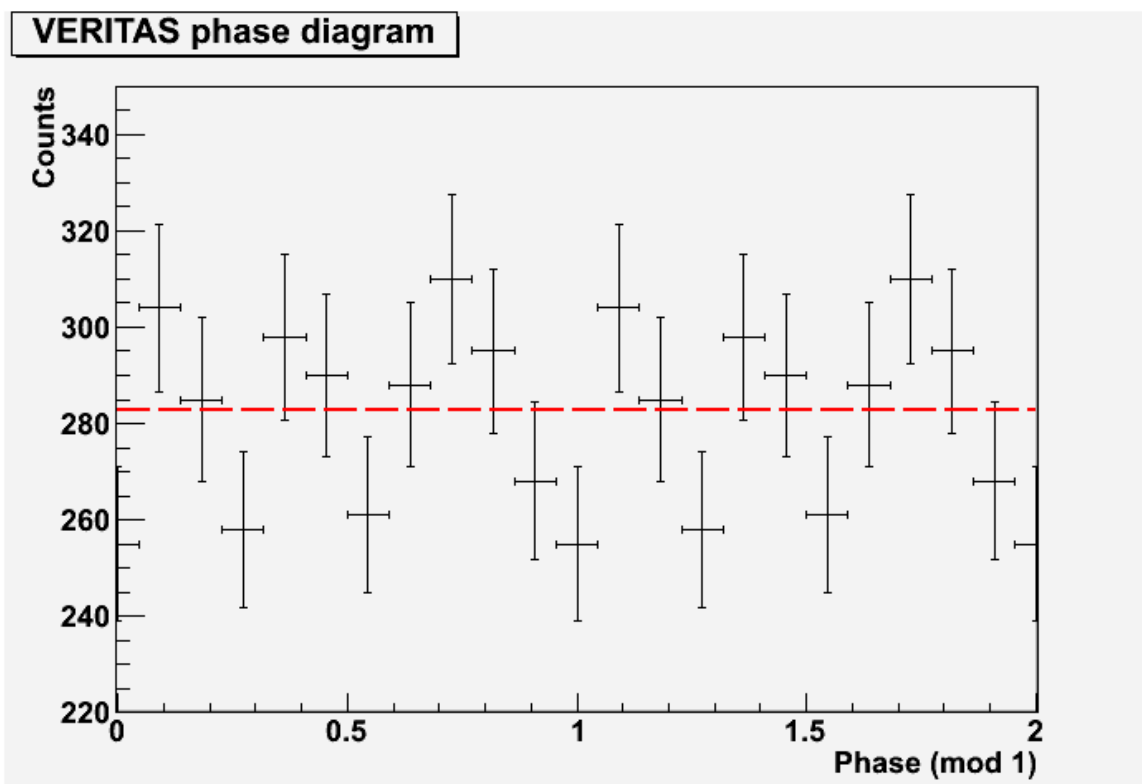


Figure 5-32. Phase histogram of PSR J2021+3651. The red dashed line is the fit of the phase histogram to a constant value.



## CHAPTER 6. CONCLUSIONS

### 6.1. PWNe Observation Summary

Table 6.1 contains a summary of the analysis in chapter 5 for the three detected sources and four candidate sources stated in chapter 4. The number of trials has to be taken into account for the final significance calculation. Each set of cuts used counts as a different trials factor. Additionally, since many sources are extended and offset from the pulsar, then searching throughout the FOV for signals also add trials. In this work, most sources were analyzed with three SIZE cuts (pulsar, medium and hard cuts), a point source analysis, an extended source analysis and two based on source strength (1% and 5% of the Crab), bringing a maximum of twelve different combinations of cuts. Additional trials need to be taken into account for searching sky regions offset from the pulsar position. For sources that are coincident with the pulsar position, this adds no additional trials. The number of additional trials can be approximated by the area of the FOV divided by the  $\theta^2$  cut. Maps produced in this work used a  $2.5^\circ \times 2.5^\circ$  square search region centered on the pulsar. This eliminates fluctuations that occur towards the edge of the FOV due to low statistics. It also seems unlikely that VHE emission due to PWN would be so distant from the pulsar, since only young pulsars were used in this work. This multiplies any extended source analysis by a factor of 156 and any point source analysis by 370.

Table 6.1. Analysis summary of PWN

PWN	$N_{on}$	$N_{off}$	$\alpha$	$N_{ex}$	Exp (min)	$S$ ( $\sigma$ )
Crab	25766	27620	0.108	22778.3	2357.7	227.2
G54.1+0.3	140	1564	0.050	61.2	1841.7	6.02
G106.3+2.7	693	2745	0.181	194.9	3344.3	7.51
3C58	359	4712	0.075	6.0	1078.5	0.31
G75.2+0.1	195	459	0.248	81.0	2027.5	6.03
HESS J1857	499	3293	0.110	136.8	822.4	6.35
PSR J1928	123	1310	0.102	-10.9	1841.7	-0.91

Table 6.1 summarizes the VERITAS steady emission search in this work. The  $N_{on}$ ,  $N_{off}$  and  $\alpha$  columns are the values used to calculate the maximum significance ( $S$ ) using equation 3.10. The ring background model was used to estimate the background.  $N_{ex}$  is the number of excess counts at the maximum significance point.

Trials reduce the probability of the VHE excess being a statistical fluctuation by an amount for  $N$  trials:

$$P_{trials} = 1 - (1 - P)^N \quad \text{Eq. 6.1}$$

where  $P$  is the pre-trial probability the signal of being a statistical fluctuation. That probability is then converted back into a Gaussian significance in table 6.2.

Table 6.2. Post-trials Significance of detected sources

Source	$S$	$N_{trials}$	$S_{trials}$	$P_{trials}$
G54.1+0.3	6.02	6	5.73	$1.0 \times 10^{-8}$
G106.3+2.7	7.51	1462	6.49	$8.6 \times 10^{-11}$
G75.2+0.1	6.03	1422	4.72	$2.4 \times 10^{-6}$
HESS J1857	6.35	1052	5.18	$2.2 \times 10^{-7}$

Table 6.2 displays results of the calculations of post-trials significance for sources above  $5\sigma$  pre-trials. The  $S$  column is the maximum significance from table 6.1. The number of trials is the  $N_{trials}$  column. The probability calculated from the equation 6.1 is the  $P_{trials}$  column, then converted back into a Gaussian significance in the  $S_{trials}$  column. Crab is not included, since it is already a strongly detected source. Since the post-trials significance for G75.2+0.1 below  $5\sigma$ , it is technically a not VHE detection.

Table 6.3 summarizes the spectral information for the seven sources in this work. Upper limits with  $5\sigma$  confidence at the pulsar position will be stated in the case of non-detections. Best fit values of  $k$  and  $\Gamma$  of the spectra to powerlaw fits of the form of equation 5.1 are in the 2<sup>nd</sup> and 3<sup>rd</sup> columns. Energy flux is obtained by the integral of the spectral fit from 1 to 10 TeV in the  $F_{TeV}$  column. Distance ( $d$ ) in units of kpc are in the 5<sup>th</sup> column. Values in the  $F_{TeV}$  column are multiplied by  $4\pi d^2$  to get the luminosity in the  $L_{TeV}$  column. The next section will discuss the implications of these results.

Table 6.3. Summary of Spectral Data

Source	$k$ ( $\text{TeV}^{-1}\text{cm}^{-2}\text{s}^{-1}$ )	$\Gamma$	$F_{TeV}$ (CU)	$d$ (kpc)	$L_{TeV}$ (ergs/s)
Crab	$(3.43\pm 0.04)\times 10^{-11}$ *	$-2.43\pm 0.02$ *	1.0	2.0	$1.08\times 10^{34}$
G54.1+0.3	$(1.26\pm 0.12)\times 10^{-12}$	$-2.40\pm 0.20$	0.037	5.0	$2.51\times 10^{33}$
G106.3+2.7	$(1.78\pm 0.33)\times 10^{-12}$	$-2.19\pm 0.33$	0.058	8.0	$9.92\times 10^{33}$
HESS J1857	$(5.44\pm 0.92)\times 10^{-12}$	$-2.32\pm 0.26$	0.17	10.3	$4.73\times 10^{34}$
G75.2+0.1	$(5.93\pm 1.84)\times 10^{-13}$	$-1.35\pm 0.21$	0.03	4.0	$1.07\times 10^{33}$
3C58**	$<7.61\times 10^{-13}$	$-2.43\pm 0.02$	$<0.022$	3.2	$<8.81\times 10^{32}$
PSR J1928**	$<6.87\times 10^{-13}$	$-2.43\pm 0.02$	$<0.020$	8.1	$<5.10\times 10^{33}$

\*Based on the OVA data in this work

\*\* 95% upper limit assuming a Crab-like spectrum

## 6.2. PWNe Discussion

The selection criteria for the putative sources studied in this work require three criteria:

- [1] The pulsar associated with the PWN must have  $\dot{E} > 1 \times 10^{36}$  ergs/s.
- [2] The pulsar associated with the PWN must have  $\tau_c < 100$  kyrs.
- [3] The PWN must be in the Northern hemisphere.

The first and second criteria imply that the PWN have a known pulsar, so PWN without known pulsars, such as CTB 87, are not included. The first two criteria were chosen because PWN previously seen in VHE (mostly in the southern hemisphere) follow this trend. The third criterion was required because VERITAS is a Northern hemisphere instrument. It is logical to conclude that PWN that fit these criteria are therefore the most likely for detection by a northern ACT such as VERITAS.

There are seven PWNe that fit these criteria. Four of the seven PWNe are positive detections by VERITAS. G75.2+0.1 is a promising VHE candidate, and is only below  $5\sigma$  after trial penalties are applied. The spectrum of this source, figure 5-29, is harder than any other PWN in VHE, with a photon index of -1.3. The spectrum also shows a possible break or curvature to, although this has not been explored in detail. More observations will likely bring the post-trial significance above  $5\sigma$ , and provide more detail on the morphology and spectra.

Two PWN (PSR J1928+1746 and 3C58) are not detected. 3C58 has only 17 hours of observation, well below the  $\sim 50$  hours required before the T1 move for the detection of a 1% Crab VHE source. An upper limit of 2.2% of the Crab flux is placed on 3C58, implying that more time is required to test if 3C58 is a VHE source. Similarly, while G54.1+0.3 has 31 hours of observation, PSR J1928+1746 is only in the FOV in the south and west wobble pointing, giving roughly half the exposure time of G54.1+0.3 on PSR J1928+1746. The 2.0% of Crab flux upper limit on PSR J1928+1746 also implies that more observation time is required if it is a VHE source. PSR J1928+1746 is more distant than most pulsars associated with VHE sources. The time on either source was not

enough to achieve a 1% of the Crab sensitivity, which might be required if either are VHE sources.

Because the majority of PWN sources in this work are positive detections, the first two selection criteria tell us something about the nature of the VHE PWN sources. The first criteria, that high  $\dot{E}$  PWN are more likely to be VHE emitters, implies that some amount of the spin-down luminosity is being transferred to the pulsar wind, which is then emitted as high energy radiation. This is also supported by the  $L_{TeV} \sim \dot{E}^{1/2}$  correlation illustrated by figure 4-3, as well as the best fit of equation 4-2. Interestingly enough, the luminosity of pulsars in the GeV band show the same correlation, implying a possible connection of bright pulsars seen by FERMI and PWN seen at TeV energies. Follow up observations of new pulsars discovered by FERMI [97] might lead to new discoveries in the TeV band.

Uncertainty in determining the distance to a PWN is the most likely reason for discrepancies in luminosity calculations. The determination of distance to pulsars can often be disputed. As an example, PSR J2021+3651 has a distance of 12 kpc based on dispersion measure [83], but the X-ray spectra is consistent with a distance of 2 to 4 kpc [82]. This work assumes a distance closer to the X-ray spectral measurements, 4 kpc, since VHE PWN further than 10 kpc tend not to be seen. PSR J1856+0245, which is the most recently discovered pulsar in this work, which has an unusually high TeV luminosity to  $\dot{E}$  ratio, might have a more reasonable efficiency if the distance estimate was closer.

It has been suggested that several HESS unidentified sources are actually PWN [98]. This certainly seems to be the case of HESS J1857+026, which shows many of the properties of a PWN. Multi-wavelength observations of unidentified sources may find other PWNe. Understanding why some PWN appear to be dark at lower energies could better constrain PWNe models.

The second criterion, that PWN younger than 100 kyrs tend to be VHE emitters, implies a leptonic origin of VHE gamma rays through IC scattering. An estimate of the cooling lifetime of electrons, assuming energy losses from synchrotron radiation and IC scattering from the CMBR, is roughly 100 kyrs:

$$\tau(E_e) \sim \frac{E_e}{dE_e/dt} \sim \frac{\gamma m_e c^2}{P_{IC} + P_{Synch}} \sim \frac{100 \text{kyrs}}{(1 + 0.144 B_{\mu G}^2) E_{TeV}^{1/2}} \quad \text{Eq. 6.2}$$

where  $\gamma$  is the Lorentz factor and,  $P_{Synch}$  and  $P_{IC}$  are the electron losses from synchrotron and IC, given by equations 1.1 and 1.4, respectively.  $B_{\mu G}$  is the mean magnetic field of the PWN in units of  $\mu G$ . Equation 6.2 gives an estimate of a potential cutoff of VHE emission, and PWN much older than 100 kyrs may not have electrons energetic enough to emit in the VHE range. The oldest PWN in the population study of VHE PWN is still less than 200 kyrs.

### 6.3. Pulsar Observation Summary

Table 6.4 summaries the pulsar analysis in this work. The results of the two statistical tests are shown, along with the significance for the Crab pulsar at the P2 position. The results for both tests are shown in the  $\chi_{10}^2$  and  $Z_1^2$  columns, respectively. Each statistical test performed for each pulsar counts as a trial, so each pulsar has two trials, except for Crab which has three. Probabilities are calculated from a  $\chi^2$  distribution. The lowest post-trials probability is then shown in the  $P_{trials}$  column, along with the probability expressed as a Gaussian significance in the  $S_{trials}$  column. None of the pulsar tests show a post-trials significance above  $5\sigma$ , concluding that none of the pulsars are seen in VHE.

Table 6.4. Pulsar Statistical Test Results

Pulsar (begins with 'PSR')	$\chi_{10}^2/10$	$Z_1^2/2$	$S$ ( $\sigma$ )	$S_{trials}$ ( $\sigma$ )	$P_{trials}$
B0531+21 (Crab)	2.07	1.70	3.71	3.42	$6.26 \times 10^{-4}$
J1930+1852	1.01	5.84	NA	1.62	0.105
J2229+6114	0.99	5.42	NA	1.52	0.129
J1856+0245	1.04	2.42	NA	0.66	0.507
J0205+6449	1.56	1.42	NA	1.25	0.211
J2021+3651	2.7	0.68	NA	0.10	0.917

#### 6.4. Pulsar Discussion

The statistical tests show that the most likely future candidate for VHE pulsar detection is the Crab at the P2 position. The peak of the pulsed emission in the VERITAS Crab data occurs at 160 GeV. If this result is proven to be a positive detection later, would have an impact for existing pulsar models, since pulsed photons have not yet been detected at energies that high. Photons close to the neutron star surface pair produce due to the high magnetic field. The energy cutoff of the pulsar can therefore give an approximate value of the distance from the NS surface where photons are emitted. Equation 6.3 shows this relationship:

$$E_{cut} \approx 0.4 \sqrt{\frac{r}{R} P_{[s]}} \max \left\{ 1, \frac{0.1 B_{crit}}{B_0} \left( \frac{r}{R} \right)^3 \right\} GeV \quad \text{Eq. 6.3}$$

where  $r$  is the distance from the center of the NS to the point of emission  $R$  is the NS radius, and  $B_{crit} = 4.4 \times 10^{13}$  G is the critical magnetic field from quantum field theory [99]. For a cutoff energy of  $E_{cut} = 160$  GeV, evaluating equation 6.1 for the Crab pulsar gives  $r/R > 10.7$ . Emission at that point in the magnetosphere would cast more doubts in the polar cap models, which requires emission close to the NS surface. Pulsed emission of the Crab pulsar seen by MAGIC has already put a limit of  $r/R > 6.2 \pm 0.2_{stat} \pm 0.4_{syst}$  [28]. Spectral points could be added to the spectral energy distribution for the Crab pulsar, such as figure 1-4. Additional points at those energies (not just upper limits) would reveal more about the nature of the pulsar cutoff, whether it is an exponential

(preferred by Outer Gap models), super-exponential (preferred by Polar Gap models), or something different like a change in the power-law index. Finally, detection of only the Crab interpulse would follow the trends seen in other wavelengths, with the ratio of P1/P2 decreasing with energy. More observations of the Crab and other pulsars will determine whether or not the pulsar can produce emission in the VHE band.



## BIBLIOGRAPHY

- [1] Weekes, T.C., Cawley M.F., Fegan D.J., Gibbs K.G., Hillas A.M., Kowk P.W., Lamb R.C., Lewis D.A., Macomb D., Porter N.A., Reynolds P.T., and Vacanti G., “Observations of TeV Gamma Rays from the Crab Nebula using the atmospheric Cherenkov imaging technique,” *The Astrophysical Journal*, vol. 342, 1989.
- [2] [HTTP://TEVCAT.UCHICAGO.EDU/](http://TEVCAT.UCHICAGO.EDU/)
- [3] Weekes, Trevor. “TeV Gamma-Ray Astronomy: The Story so Far” *Proceedings of the 4th International Meeting on High Energy Gamma-Ray Astronomy*. AIP Conference Proceedings, Volume 1085, pp. 3-17, 2008.
- [4] Holder, J. et al. (The VERITAS Collaboration) “First VERITAS Telescope” *Astroparticle Physics* Volume 25, p. 391-401, 2006.
- [5] R.A. Ong, et al. (The VERITAS Collaboration) “Highlight Talk: Recent Results from VERITAS” in *31<sup>st</sup> International Cosmic Ray Conference*, 2009, Lodz Poland.
- [6] Aharonian, F. et al. (The HESS Collaboration) “A New Population of Very High Energy Gamma-Ray Sources in the Milky Way,” *Science*, vol. 1938, 2005.
- [7] Aharonian, F. et al. (The HESS Collaboration) “Calibration of cameras of the HESS detector”, *Astroparticle Physics*, Volume 22, Issue 2, pages 109-125, Nov. 2004.
- [8] Vincent, P. for the HESS collaboration. “HESS Phase II”, *Proceedings of the 29th International Cosmic Ray Conference*. August 3-10, 2005, Pune, India.
- [9] Moralejo, A. for the MAGIC Collaboration. “Status of Magic-II” *Proceedings of the 2009 Fermi Symposium*. December 2009, Washington DC.

- [10] J. Cortina, A. Armanda, A. Biland, O. Blanch, M. Garczarczyk, F. Goebel, P. Majumdar, M. Mariotti, A. Moralejo, D. Paneque, R. Paoletti, N. Turini and the MAGIC collaboration. "Technical Performance of the MAGIC Telescope" in *29<sup>th</sup> International Cosmic Ray Conference*, 2005.
- [11] Carson, J. "GLAST: physics goals and instrument status" *Proceedings from TeV Particle Astrophysics II*, Madison, WI, August 2006
- [12] Urry, Megan C., Padovani, Paolo. "United Schemes for Radio-Loud Active Galactic Nuclei" Publications of the *Astronomical Society of the Pacific*, v.107, p.803
- [13] Punch, M. et al. "Detection of TeV photons from the active galaxy Mrk 421", *Nature* vol. 358, no. 6386, Aug. 6, 1992, p. 477, 478.
- [14] Longair, M. "High Energy Astrophysics"
- [15] Masahiro, T. "Discovery of Very High Energy Gamma-Rays from the Distant Flat Spectrum Radio Quasar 3C 279 with the MAGIC Telescope" Proceedings of the *30<sup>th</sup> International Cosmic Ray Conference*. July 2007, Mérida, Yucatán, Mexico.
- [16] Acciari, V. et al. (The VERITAS Collaboration) "A connection between star formation activity and cosmic rays in the starburst galaxy M82" *Nature*, Volume 462, Issue 7274, pp. 770-772 (2009).
- [17] Acero, F. et al. (The HESS Collaboration) "Detection of Gamma Rays from a Starburst Galaxy" *Science*, Volume 326, Issue 5956, pp. 1080- (2009)
- [18] Aharonian, F. et al. (The HESS Collaboration) "Very High Energy Gamma Rays from the Direction of Sagittarius A\*" *Astronomy and Astrophysics*, v.425, p.L13-L17 (2004).
- [19] Acciari et al. (The VERITAS Collaboration) "Observation of Extended Very High Energy Emission from the Supernovae Remnant IC 443 with VERITAS" *The Astrophysical Journal Letters*, Volume 698, Issue 2, pp. L133-L137 (2009).
- [20] Paredes, J.M., Zabalza, V. "Microquasars in the GeV-TeV era" in *7<sup>th</sup> AGILE Workshop: The Bright  $\gamma$ -ray sky* Frascati, Italy, 29 September to 1 October 2009

- [21] Acciari, V.A. et al. “Multiwavelength Observations of LS I +61°603 with Veritas, Swift and RXTE” *The Astrophysical Journal*, Volume 700, Issue 2, pp. 1034-1041 (2009).
- [22] Aharonian, F. et al. (The HEGRA Collaboration) “An Unidentified TeV Source in the Vicinity of Cygnus OB2” *Astronomy and Astrophysics*, v.393, p.L37-L40 (2002)
- [23] Hessels, J.W.T. et al. “PSR J1856+0245: Arecibo Discovery of a Young, Energetic Pulsar Coincident with the TeV  $\gamma$ -ray Source HESS J1857+026”, *The Astrophysical Journal*, 682: L41-L44, 2008 July 20.
- [24] Rybicki, G.B. and Lightman, A.P. “Radiative Processes in Astrophysics”
- [25] Blumenthal, G.R. and Gould, R.J. “Bremsstrahlung, Synchrotron Radiation, and Compton Scattering of High-Energy Electrons Traversing Dilute Gases”, *Reviews of modern physics*, volume 42, number 2, April 1970.
- [26] Meszaros, P. “High-Energy Radiation from Magnetized Neutron Stars”
- [27] Atoyan, A., Aharonian, F. “On the mechanisms of gamma radiation in the Crab Nebula” *Monthly Notices of the Royal Astronomy Society*, volume 278 p. 525-541 (1996)
- [28] The MAGIC Collaboration. “Observation of Pulsed  $\gamma$ -Rays above 25 GeV from the Crab Pulsar with MAGIC”, *Science*, volume 322, 21 November 2008.
- [29] Ostlie, D., Carroll, B. “An Introduction to Modern Stellar Astrophysics”
- [30] Griffiths, David J. “Introduction to Quantum Mechanics”
- [31] Ostriker, J.P. & Gunn, J.E. “On the Nature of Pulsars. I. Theory” *The Astrophysical Journal*, volume 157, p. 1395, Sept. 1969
- [32] Goldreich, P. & Julian, W. “Pulsar Electrodynamics” *The Astrophysical Journal*, volume 157, August 1969
- [33] Kosack, K., et al. (The Whipple Collaboration) “TeV Gamma-Ray Observations of the Galactic Center” *The Astrophysical Journal*, Volume 608, Issue 2, pp. L97-L100. (2004)

- [34] Strurrock, P.A. "A Model of Pulsars" *The Astrophysical Journal*, volume 164, p. 529-556, March 1971
- [35] Harding, A.K., Tademaru, E., Esposito, L.W. "A Curvature-Radiation-Pair-Production Model for Gamma-Ray Pulsars" *The Astrophysical Journal*, volume 225, p. 226-236 Oct 1978
- [36] Harding, A. K. "Pulsar  $\gamma$ -Rays: Spectra, Luminosities, and Efficiencies" *The Astrophysical Journal*, volume 245, p. 267-273, April 1981
- [37] Daughtery, J.K., Harding, A.K. "Electromagnetic Cascades in Pulsars" *The Astrophysical Journal*, volume 252, p. 337-347, January 1982
- [38] Cheng K.S., Ho, C., Ruderman, M. "Energetic Radiation from Rapidly Spinning Pulsars. I. Outer Magnetosphere Gaps" *The Astrophysical Journal*, volume 300, p. 500-521, January 1986
- [39] Cheng K.S., Ho, C., Ruderman, M. "Energetic Radiation from Rapidly Spinning Pulsars. II. Vela and Crab" *The Astrophysical Journal*, volume 300, p. 522-539, January 1986
- [40] Osmanov, Z., Rieger, F.M. "On Particle Acceleration and Very High Energy  $\gamma$ -ray Emission in Crab-like Pulsars" *Astronomy and Astrophysics*, volume 502, Issue 1, 2009, p. 15-20 (2009).
- [41] Arons J., Scharlemann, E.T. "Pair Formation above Pulsar Polar Caps – Structure of the Low Altitude Acceleration Zone" *The Astrophysical Journal*, vol. 231, p. 854-879, Aug 1979
- [42] Muslimov, A., Harding, A. "Extended Acceleration in Slot Gaps and Pulsar High-Energy Emission" *The Astrophysical Journal*, vol. 588, p. 430-440, May 2003
- [43] Cheng K.S. et al. "Could Very High Energy Gamma Rays from the Crab Nebula Result from p-p Collision?" *Journal of Physics G: Nuclear and Particle Physics*, volume 16, Issue 7, p. 1115-1121, 1990
- [44] Weiler, K.W. "Are Crab-type Supernovae Remnants (Plerions) Short-lived?" *Astronomy and Astrophysics*, Vol. 70, p. 419, 1979

- [45] DeJager, O.C. & Venter, C. “Ground-based Gamma-Ray Observations of Pulsars and their Nebulae: Towards a New Order” Proceedings from *Cherenkov 2005*, Palaiseau, France
- [46] Blondin, J., Chevalier, R., Frierson, D. “Pulsar Wind Nebulae in Evolved Supernovae Remnants” *The Astrophysical Journal*, Vol 563, p. 806-815, Dec 2001
- [47] Gaensler, B. & Slane, P. “The Evolution and Structure of Pulsar Wind Nebulae” *Annual Review of Astronomy & Astrophysics*, vol. 44, Issue 1, pp.17-47
- [48] Slane, P. “High Energy Studies of Pulsar Wind Nebulae” *Proceedings of 4th Heidelberg International Symposium on High Energy Gamma-Ray Astronomy*, Heidelberg, Germany
- [49] Stanev, T. “High Energy Cosmic Rays” 2<sup>nd</sup> edition, Praxis Publishing Ltd, Chichester, UK, 2004.
- [50] [HTTP://WWW.PHOTONIS.COM/INDUSTRYSCIENCE/PRODUCTS/PHOTOMULTIPLIERS\\_ASSEMBLIES/PRODUCT\\_SPECIFICATIONS](http://www.photonis.com/industry-science/products/photomultipliers-assemblies/product-specifications)
- [51] Hays, E. et al. (The VERITAS Collaboration.) “VERITAS Data Acquisition” Proceedings from *the 30<sup>th</sup> ICRC conference*, Merida Mexico
- [52] Cogan, P. et al. (The VERITAS Collaboration.) “Analysis of Flash ADC Data with VERITAS” Proceedings from *the 30<sup>th</sup> ICRC conference*, Merida Mexico
- [53] Weinstein, A. for the VERITAS Collaboration. “The VERITAS Trigger System” Proceedings from *the 30<sup>th</sup> ICRC conference*, Merida Mexico
- [54] Hanna, D. for the VERITAS Collaboration. “Calibration Techniques for VERITAS” Proceedings of the *30th International Cosmic Ray Conference*. July 3 - 11, 2007, Mérida, Yucatán, Mexico.
- [55] Daniel, M. for the VERITAS Collaboration. “The VERITAS Standard Data Analysis” Proceedings from *the 30<sup>th</sup> ICRC conference*, Merida Mexico
- [56] Li, T. & Ma, Y. “Analysis Methods for Results in Gamma-ray Astronomy” *The Astrophysical Journal*, vol 272, p. 317-324, September 1983

- [57] Berge, D., Funk, S., Hinton, J. “Background Modeling in Very-High-Energy  $\gamma$ -ray Astronomy” *Astronomy and Astrophysics* Vol 466, p. 1219-1229, 2007
- [58] Hillas, A.M. et al. “The Spectrum of TeV Gamma Rays from the Crab Nebula” *The Astrophysical Journal*, Vol 503, p. 744-759, August 20 1998
- [59] Aharonian, F. et al. “First Detection of a VHE Gamma-Ray Spectral Maximum from a Cosmic Source: HESS Discovery of the Vela X Nebula” *Astronomy and Astrophysics* Vol. 448, p. 43-47, January 2006.
- [60] Renaud, M. et al. “Pulsar Wind Nebula Candidates Recently Discovered by H.E.S.S” Proceedings from the 4<sup>th</sup> Heidelberg International Symposium of High Energy Gamma-Ray Astronomy, 2008
- [61] Aharonian, F. et al. “Discovery of the two “Wings” of the Kookaburra Complex in VHE  $\gamma$ -rays with HESS” *Astronomy and Astrophysics* Vol. 456, p. 245-251, June 2006.
- [62] Aharonian, F. et al. “Discovery of Extended VHE Gamma-Ray Emission from the Asymmetric Pulsar Wind Nebulae in MSH 15-52 with HESS” *Astronomy and Astrophysics*, Volume 435, Issue 1, May III 2005, pp.L17-L20
- [63] Aharonian, F. et al. “Discovery of two Candidate Pulsar Wind Nebulae in Very-High-Energy Gamma-Rays” *Astronomy and Astrophysics* Vol. 472, p. 489-495, April 2007.
- [64] Aharonian, F. et al. “The H.E.S.S Survey of the Inner Galaxy in Very-High-Energy Gamma-Rays”, *The Astrophysical Journal*, Vol 636, p. 777-797, 2006.
- [65] Acciari, V.A. et al. “Discovery of VHE  $\gamma$ -Ray Emission from the SNR G54.1+0.3”, *The Astrophysical Journal Letters*, Volume 719, Issue 1, p. 69-73, 2010.
- [66] Acciari, V.A. et al. “Detection of Extended VHE Gamma-Ray Emission from G106.3+2.7 with VERITAS” *The Astrophysical Journal*, Volume 703, p 6-9 September 20, 2009
- [67] [HTTP://WWW.ATNF.CSIRO.AU/](http://www.atnf.csiro.au/)

- [68] Staelin, D., Reifenstein, E. "Pulsating Radio Sources near the Crab Nebulae" *Science*, Volume 162, Issue 3861, pp. 1481-1483
- [69] Hewish, A., Bell, S. "Observation of a Rapidly Pulsating Radio Source" *Nature*, Volume 217, Issue 5130, pp. 709-713 (1968).
- [70] Cocke, W., Disney, J. and Taylor, D. "Discovery of Optical Signals from Pulsar NP 0532" *Nature*, Volume 221, Issue 5180, pp. 525-527 (1969).
- [71] Camilo, F. et al. "Discovery of a 136 Millisecond Radio and X-Ray Pulsar in Supernovae Remnant G54.1+0.3" *The Astrophysical Journal*, Volume 574, Issue 1, pp. L71-L74. (2002)
- [72] Reich, W. et al. "Evidence for two Young Galactic Supernova Remnants" *Astronomy and Astrophysics* (ISSN 0004-6361), vol. 151, no. 2, Oct. 1985, p. L10-L12.
- [73] Lu, F. et al. "Observations of the Supernova remnant G54.1+0.3: X-ray spectrum and evidence for an X-ray jet" *Astronomy and Astrophysics*, v.370, p.570-575 (2001)
- [74] Li, H., Chen, Y., Zhang, L. "Lepto-hadronic origin of  $\gamma$ -rays from the G54.1+0.3 pulsar wind nebula" *Monthly Notices of the Royal Astronomical Society: Letters*, Volume 408, Issue 1, pp. L80-L84. (2010)
- [75] Cordes, J. "Arecibo Pulsar Survey Using ALFA. I. Survey Strategy and First Discoveries" *The Astrophysical Journal*, Volume 637, Issue 1, pp. 446-455. (2006)
- [76] Hartman, R. "The Third EGRET Catalog of High-Energy Gamma-Ray Sources" *The Astrophysical Journal Supplement Series*, Volume 123, Issue 1, pp. 79-202. (1999)
- [77] Higgs, L. "The Low-Resolution DRAO Survey of H I Emission from the Galactic Plane" *The Astronomical Journal*, Volume 120, Issue 5, pp. 2471-2487. (2000)
- [78] Pineault, S. Joncas, G. "G106.3+2.7: A Supernovae Remnant in a Late Stage of Evolution" *The Astronomical Journal*, Volume 120, Issue 6, pp. 3218-3225. (2000)

- [79] Abdo, et al. (The Fermi Collaboration) “Fermi Large Area Telescope Detection of Pulsed  $\gamma$ -rays from the Vela-like Pulsars PSR J1048-5832 and PSR J2229+6114” *The Astrophysical Journal*, Volume 706, Issue 2, pp. 1331-1340 (2009)
- [80] Abdo, et al. (The Milagro Collaboration) “Milagro Observations of Multi-TeV Emission from Galactic Sources in the Fermi Bright Source List” *The Astrophysical Journal Letters*, Volume 700, Issue 2, pp. L127-L131. (2009)
- [81] Aharonian, F. et al. (The HESS Collaboration) “HESS Very-high-energy Gamma-Ray Sources Without Identified Counterparts” *Astronomy and Astrophysics*, Volume 477, Issue 1, January I 2008, pp.353-363. (2008)
- [82] Roberts, M. et al. “PSR J2021+3651: A Young Radio Pulsar Coincident with an Unidentified ERGET  $\gamma$ -Ray Source” *The Astrophysical Journal*, Volume 577, Issue 1, pp. L19-L22. (2002)
- [83] Hessels, J. et al. “Observations of PSR J2021+3651 and its X-ray Pulsar Wind Nebula G75.2+0.1” *The Astrophysical Journal*, Volume 612, Issue 1, pp. 389. (2004)
- [84] Abdo, A. et al. (The Fermi Collaboration) “Pulsed Gamma-Rays from PSR J2021+3651 with the Fermi Large Area Telescope” *The Astrophysical Journal*, Volume 700, L1059-L1066, August 1 (2009)
- [85] Hermann, B. “Polarmetric Aperture Synthesis Observation of four Small-Diameter Supernovae Remnants” *Astronomical Journal*, Vol. 78, p. 879 (1973)
- [86] Becker, H. “X-ray Observations of Crab-like Supernovae Remnants” In *Proceedings from Supernova remnants and their X-ray emission*, Venice, Italy, August 30-September 2, 1982
- [87] Murray, S. et al. “Discovery of X-Ray Pulsations from the Compact Central Source in the Supernovae Remnant 3C58” *The Astrophysical Journal*, Volume 568, Issue 1, pp. 226-231. (2002)
- [88] Camilo, F. et al. “Discovery of Radio Pulsations from the X-Ray Pulsar J0205+6449 in Supernovae Remnant 3C 58 with the Green Bank Telescope” *The Astrophysical Journal*, Volume 571, Issue 1, pp. L41-L44. (2002)



- [89] Roberts, D. “High Resolutions HI Observations of 3C58” *Astronomy and Astrophysics* V.274, no. 2/Jul(II), P. 427, 1993
- [90] Abdo, A. et al. (The Fermi Collaboration) “Pulsed Gamma-Rays from PSR J2021+3651 with the Fermi Large Area Telescope” *The Astrophysical Journal*, Volume 700, Issue 2, pp. 1059-1066 (2009).
- [91] Aharonian, F. et al. (The HESS Collaboration) “Observations of the Crab Nebula with HESS”
- [92] [HTTP://WWW.JB.MAN.AC.UK/~PULSAR/CRAB.HTML](http://www.jb.man.ac.uk/~pulsar/crab.html)
- [93] N. Otte, Private Communications.
- [94] Nolan, P. et al. “Observations of the Crab Pulsar and Nebulae by the ERGET Telescope on the Compton Gamma-Ray Observatory” *The Astrophysical Journal*, Part 1 (ISSN 0004-637X), vol. 409, no. 2, p. 697-704. (1993)
- [95] F. Camilio, Private Communications.
- [96] [HTTP://FERMI.GSFC.NASA.GOV/](http://fermi.gsfc.nasa.gov/)
- [97] Abdo, A. et al. “Detection of 16 Gamma-Ray Pulsars Through Blind Frequency Searches Using the Fermi LAT” *Science*, Volume 325, Issue 5942, pp. 840- (2009).
- [98] De Jager, O. C. et al. “Unidentified Gamma-Ray Sources as Ancient Pulsar Wind Nebulae” Proceedings from the *31st International Cosmic Ray Conference*, Lodz, Poland, July 2009
- [99] Lee, K. et al. “Lower Bounds of Altitudes for Pulsar  $\gamma$ -Ray Radiation” *Monthly Notices of the Royal Astronomical Society*, Volume 405, Issue 3, pp. 2103-2112.

## VITA

Benjamin Joshua Zitzer was born November 8, 1981 to Mark Edward Zitzer and Judy Irene Moon. He attended high school at Franklin Community High School in Franklin, Indiana, where he graduated in May 2000. He attended Purdue University from August 2000 to May 2004, earning a BS in Honors Physics. He continued studying at Purdue, earning his PhD in physics in December 2010.